PONTIFICIA UNIVERSIDAD CATOLICA DE CHILE
ESCUELA DE INGENIERIA

MULTIPHYSICS MODELING AND EXPERIMENTAL BEHAVIOR OF VISCOUS FLUID DAMPERS

CLAUDIO ODILO BENJAMÍN FRINGS ARAVENA

Thesis submitted to the Office of Research and Graduate Studies in partial fulfillment of the requirements for the Degree of Master of Science in Engineering.

Advisor:
JUAN CARLOS DE LA LLERA MARTIN

Santiago, Chile. June, 2011

PONTIFICIA UNIVERSIDAD CATOLICA DE CHILE
ESCUELA DE INGENIERIA

MULTIPHYSICS MODELING AND EXPERIMENTAL BEHAVIOR OF VISCOUS FLUID DAMPERS

CLAUDIO ODILO BENJAMÍN FRINGS ARAVENA

Members of the Committee:

JUAN CARLOS DE LA LLERA

ALDO CIPRIANO

DANIEL HURTADO

EDUARDO IZQUIERDO

Thesis submitted to the Office of Research and Graduate Studies in partial fulfillment of the requirements for the Degree of Master of Science in Engineering.

Santiago, Chile. June, 2011

ACKNOWLEDGEMENTS

Support to this investigation was provided by the Chilean Government through research grants FONDEF D07I1006 and FONDECYT 1085282.

TABLE OF CONTENTS

LIST OF TABLES

Page

LIST OF FIGURES

ABSTRACT

During the last decades, viscous fluid dampers have become an increasingly used technology for energy dissipation, protecting structures from severe ground motions. The main objectives of this research are to unveil the design parameters that control the behavior of viscous dampers subjected to cyclic motions and, subsequently, develop a comparison between analytical and experimental responses. Although extensive literature regarding these devices is available, little has been published about the internal design details that affect their behavior, due to the complex physical phenomena involved and the proprietary nature of the components of commercial dampers. Motivated by this, mathematical models accounting for the coupled fluid dynamics and heat transfer of the flow inside the damper are developed and solved with state-of-the-art numerical simulation software with multiphysics capabilities, i.e., able to handle coupled systems of different physical phenomena. First, the relevant equations that govern the problem are presented and discussed in terms of dominant tendencies. Parametric analyses are then carried out to further understand the influence of aspects such as dimensions, geometric relations between components and fluid properties in damper behavior. To validate and calibrate the model predictions, a full scale 600 *kN* prototype was designed, manufactured and tested at the Laboratory of the Department of Structural Engineering. The built prototype included the possibility of exchanging its piston, allowing the testing of different internal fluid passage configurations as well as different fluid viscosities. Results show good numerical agreement between the mathematical and physical models, which is particularly relevant for the future design and production of other damper capacities and configurations. In general, uncertainties in the model come from the representation through complex partial differential equations, but also from the rheological properties of the employed fluids, specifically their nonlinear constitutive behavior.

Key words: Vibration Control; Energy Dissipation; Passive Systems; Seismic Protection; Viscous Fluid Damper; Non Linear Viscous Fluid Damper; Multiphysics; Viscous Heating; Conjugate Heat Transfer.

RESUMEN

Durante las últimas décadas, el uso de amortiguadores viscosos para la disipación de energía en estructuras expuestas a sismos severos ha aumentado progresivamente. Los objetivos principales de este trabajo son develar los parámetros de diseño que controlan el comportamiento de amortiguadores viscosos sometidos a excitaciones harmónicas y, posteriormente, desarrollar una comparación entre respuestas analíticas y experimentales. A pesar de que existe una amplia literatura relacionada a este tipo de dispositivos, poco se ha publicado sobre los detalles de diseño que afectan su comportamiento, debido a la complejidad de los fenómenos físicos involucrados y al secreto industrial que protege a los componentes de amortiguadores comerciales. Motivado por esto, se desarrollaron modelos matemáticos que consideran la dinámica de fluidos y el comportamiento térmico dentro del amortiguador, los cuales se resolvieron con *software* de simulación numérica con capacidades multifísicas, es decir, capaces de manejar distintos fenómenos físicos acoplados. Primero, se presentan las ecuaciones relevantes que gobiernan el problema y se discuten sus tendencias dominantes. Luego se llevan a cabo análisis paramétricos para entender en profundidad la influencia de aspectos tales como dimensiones, relaciones geométricas entre los distintos componentes y propiedades del fluido en el comportamiento del amortiguador. Para validar y calibrar los modelos se diseñó y fabricó un prototipo a escala completa con una capacidad de 600 *kN*, el cual fue ensayado en el Laboratorio de Ingeniería Estructural. El prototipo incluye un pistón intercambiable, permitiendo ensayar distintas configuraciones internas y fluidos. Los resultados muestran una buena concordancia entre los modelos matemáticos y físicos, lo cual resulta relevante para el diseño futuro y la producción de otras capacidades y configuraciones. En general, las incertidumbres del modelo se pueden atribuir a la representación a través de ecuaciones diferenciales parciales complejas, pero también a las propiedades reológicas de los fluidos empleados, especialmente su relación constitutiva no lineal.

Palabras Clave: Control de Vibraciones; Disipación de Energía; Sistemas Pasivos; Protección Sísmica; Amortiguador Viscoso Lineal; Amortiguador Viscoso No Lineal; Calentamiento Viscoso; Transferencia de Calor Conjugada.

1. INTRODUCTION

The traditional approach for designing earthquake resistant structures is to provide them with a combination of lateral resistance and ductility, that is, the ability of its elements to deform beyond their elastic limit without a significant loss of strength. Under this premise, structural damage, such as cracking and/or formation of plastic hinges, is likely to occur during severe ground motions. The addition of supplemental energy dissipation devices will mitigate this effect; they will absorb part of the mechanical vibration energy, decreasing the ductility demand on structural members. Viscous fluid dampers are a proven and increasingly used technology for this purpose, dissipating the mechanical energy primarily through heat. Among seismic protection devices, they present advantages such as: (i) an extraordinarily high level of energy dissipation density, i.e., they dissipate large amounts of energy relative to their size (Symans and Constantinou 1998), (ii) ease of implementation in either new or retrofit designs, (iii) no need for replacement after earthquakes, and (iv) an output force dependent on velocity, which is out-of-phase with displacements, thus reducing structural responses without increasing elastic forces (Lee and Taylor 2001).

The basic operating principle for these devices is moving a piston through a viscous fluid enclosed in a cylindrical housing, as shown in Figure 1-1. The piston movement forces the fluid to pass from one chamber to the other through different types of orifices, being generally acknowledged that the choice of these orifices is a key aspect in controlling the damper's behavior (e.g., Cameron and Makris 2005; Constantinou and

Symans 1992; Soong and Dargush 1997; Symans and Constantinou 1998; Valdebenito et. al. 2010; Wolfe et. al. 2008).

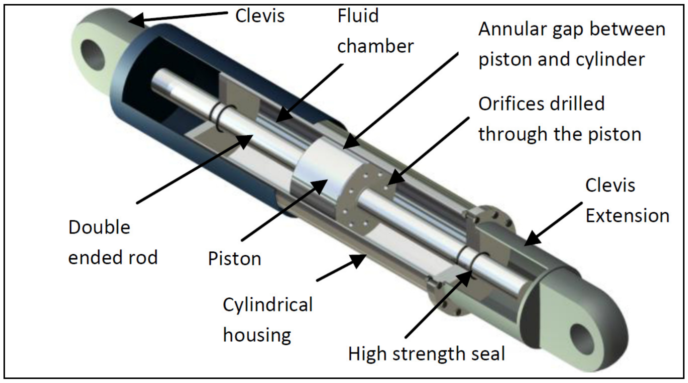

Figure 1-1: A typical internal view of a viscous fluid damper.

It is commonly accepted, yet not always accurate as will be discussed in this thesis, that a viscous damper's ouput force relates to the velocity of its end supports by a power law:

$$F = C\left|V\right|^{\alpha} \operatorname{sgn}\left(V\right) \tag{1.1}$$

where F is the output force; C is a damping coefficient; V is the relative velocity of the damper's ends (i.e., the piston's velocity); sgn( ) is the sign function; and α is an exponent with values ranging typically from 0.2 to 1 for structural engineering applications.

Extensive literature is available regarding the dynamic behavior of viscous dampers; however, due to the complex physical phenomena involved in their operation and the proprietary nature of commercial damper components, little has been published about the internal design details that control their force-velocity constitutive relationship. For instance, many authors attribute low velocity exponents ($\alpha < 1$) to intricate orifices in the piston (Cameron and Makris 2005; Constantinou and Symans 1992; Symans and Constantinou 1998; Valdebenito et. al. 2010); nevertheless, no further details are given. Motivated by this, the main objective of this research is to understand how different design aspects affect viscous damper behavior using state-of-the-art numerical simulation. The impact of geometric dimensions and relations, fluid properties, and input characteristics (amplitude and frequency) on the force-velocity relationship for dampers with different types of orifices was investigated.

Viscous damper behavior is also affected by fluid heating, mainly because of the force reduction and internal pressure rise that take place as the number of cycles increases. Consequently, a further objective is to evaluate these effects, for which the damper modeling presented herein is able to consider the interaction of fluid dynamics and heat transfer. Commercially available software able to simultaneously solve coupled systems of different physical phenomena, a concept denoted as multiphysics, were used in these calculations. Specifically, these were CFX, a finite volume based computational fluid dynamics program included in ANSYS (ANSYS Inc. 2009), and COMSOL (COMSOL AB 2008), a finite element based multiphysics program.

Finally, to validate and calibrate the models, a full scale prototype was manufactured and tested. The prototype included an exchangeable piston, allowing dynamic testing of different internal configurations and fluids.

2. PROBLEM STATEMENT AND DAMPER EQUATIONS

Figure 2-1 presents a general scheme of the problem in question. A piston is subjected to a sinusoidal displacement with amplitude A and angular frequency $\omega = 2\pi f$; as it moves, fluid passes from one chamber to the other through orifices, such as an annular gap between the cylinder and a piston of slightly smaller diameter and/or cylindrical orifices drilled through the piston. The fluid's resistance to flow will subject the piston to stresses on its surfaces that will result in the output force. Hence, the first goal of the model is to determine the fluid's velocity and pressure fields and the corresponding output force at each instant, given the piston velocity. Internal work, as a result of the intermolecular forces exerted as fluid layers try to slide past one another, will increase the fluid's temperature. Therefore, a second goal of the model is to determine the temperature field (on the fluid and solid parts), which will influence the viscosity of the fluid.

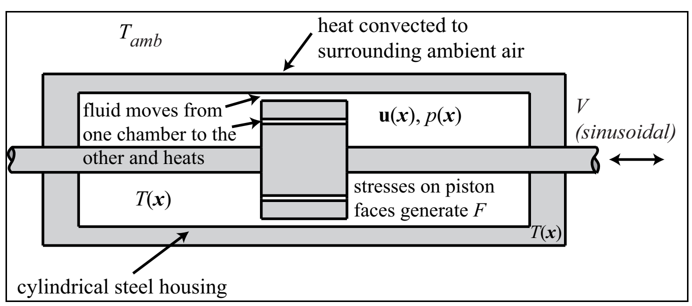

Figure 2-1: Schematic representation of the problem in concern.

2.1 Fluid Dynamics

The equations that model the fluid motion derive from basic continuum conservation principles. Conservation of mass and linear momentum lead to:

$$\frac{\partial \rho}{\partial t} + \nabla \cdot (\rho \mathbf{u}) = 0 \tag{2.1}$$

$$\rho \frac{\partial \mathbf{u}}{\partial t} + \rho \mathbf{u} \cdot \nabla \mathbf{u} = -\nabla p + \nabla \cdot \tau + \mathbf{F} \tag{2.2}$$

where ρ is the fluid density; $\mathbf{u} = (u, v, w, t)$ is the velocity field; $\nabla \mathbf{u}$ is a velocity gradient tensor; p is the pressure field; τ is the deviatoric or viscous stress tensor; and $\mathbf{F}$ corresponds to body forces, in this case $\mathbf{0}$. Eq. (2.2) represents a set of equations commonly referred to as the Navier-Stokes equations.

To solve Eqs. (2.1) and (2.2), further relations between the variables are needed. Accordingly, a fluid constitutive law expresses that viscous stresses are proportional to the symmetric strain rate tensor, defined as:

$$\mathbf{S} = \frac{1}{2}\left[\nabla \mathbf{u} + (\nabla \mathbf{u})^T\right] \tag{2.3}$$

Considering an isotropic fluid and using Stokes assumption, $\mathbf{S}$ and τ are related by a proportionality parameter μ, the dynamic viscosity of the fluid:

$$\tau = 2\mu \mathbf{S} - \frac{2}{3}\mu (\nabla \cdot \mathbf{u}) \mathbf{I} \tag{2.4}$$

If viscous stresses are linearly proportional to velocity gradients, i.e., μ is constant, the fluid is said to be Newtonian. In contrast, the relation is non linear for non-Newtonian fluids.

If the fluid is considered incompressible, density is constant and Eq. (2.1) simplifies to:

$$\nabla \cdot \mathbf{u} = 0 \tag{2.5}$$

Considering Eq. (2.5) and substituting Eq. (2.4) into (2.2) yields:

$$\rho \frac{\partial \mathbf{u}}{\partial t} + \rho \mathbf{u} \cdot \nabla \mathbf{u} = -\nabla p + \nabla \cdot \mu \left[\nabla \mathbf{u} + \left(\nabla \mathbf{u} \right)^T \right] \tag{2.6}$$

Thus, for an incompressible fluid, Eqs. (2.5) and (2.6) are enough to form a system with the same number of equations and unknowns as long as μ is a function of the velocity field only.

Silicone oil, used as the damper fluid, is significantly more compressible than most liquids. Despite this, assuming incompressibility leads to a very good approximation of the damper's force-velocity relationship, accurately predicting the maximum force and providing a "backbone" curve that resembles the shape of the result considering compressibility, as will be seen. It is particularly accurate at low frequency excitations. Computationally much less expensive, the incompressibility assumption is suitable for parametric analysis.

If compressibility is to be considered nonetheless, fluid density may be related to pressure with:

$$\rho = \rho_{ref} \left[1 + \beta \left(p - p_{ref} \right) \right] \tag{2.7}$$

where ρ_{ref} represents the density at a reference pressure p_{ref} and β is the fluid compressibility, assumed constant. This formulation is known as barotropic, since density depends only on pressure. With the boundary conditions used herein (detailed further on), this formulation is valid as long as the Mach number, defined as

$Ma = |\mathbf{u}|\sqrt{\rho \cdot \beta}$, is less than one. The practical limit is however lower than one since already at moderate Mach numbers the equations start to display very sharp gradients that require special numerical techniques. The rule of thumb is that these effects will not appear for $Ma < 0.3$ (COMSOL AB 2008). If viscosity is a function only of the velocity field, Eqs. (2.1) through (2.4) and (2.7) form a system with the same number of equations and unknowns, allowing to completely determine the damper's force-velocity relationship.

The damper's output force at each time instant may be calculated by integrating τ and p in the axial direction at all piston surfaces in contact with the fluid. Since viscous stresses are generally negligible in comparison to pressure, an excellent approximation of this force is $A_p \cdot \Delta p$, where A_p is the area of the piston face and Δp is the pressure difference between chambers.

2.2 Heat Transfer

Fluid heating also plays an important role in damper performance. For instance, end seals (see Figure 1-1) have operating temperature limits, the steel housing cylinder (which confines the fluid) must be designed to withstand the pressure build up due to fluid thermal expansion and, most important, the damper output force is expected to decline progressively as the fluid viscosity decreases with the rise in temperature. Hence, for design purposes it becomes relevant to estimate such force reduction as the number of cycles increases.

The scalar equation that governs the temperature field within the fluid or solid is derived from the conservation of energy:

$$\rho C_p\left(\frac{\partial T}{\partial t}+(\mathbf{u}\cdot\nabla)T\right)=\nabla\cdot(k\nabla T)+\tau:\mathbf{S} \tag{2.8}$$

where T is the temperature field; C_p is the specific heat of the medium; and k is the thermal conductivity. This formulation is valid as long as the Mach number is well below one, i.e., $Ma < 0.3$, since the sound wave transport term is being neglected (COMSOL AB 2008). The term $\tau:\mathbf{S}$ represents the rate of work for changing the shape of a fluid element at constant volume and is known as the dissipation function. It acts as a source of thermal energy in the damper, since work is converted irreversibly into heat through this mechanism. Naturally, in the domain represented by the steel housing, **u** and **S** are zero, and heat is transferred only by conduction.

Heat transfer to the ambient air is modeled with a convection boundary condition, $k_s\partial T/\partial \boldsymbol{e} = h(T - T_{amb})$, in which k_s is the steel thermal conductivity, $\boldsymbol{e}$ is the direction normal to the boundary and h is a heat transfer coefficient. The rod boundary was considered adiabatic in its full length.

If the velocity field is known, after solving the continuity and momentum equations, Eq. (2.8) may be solved independently. However, the three conservation equations may be coupled if some fluid property, viscosity in our case, is modeled as temperature dependent.

2.3 Fluid Properties

Silicone oil or polydimethylsiloxane, an organic silicon-based polymer, is commonly used as the fluid in viscous dampers. For low values of shear rate, it has Newtonian behavior; however, beyond certain level, viscosity starts to decrease with increasing shear rate, phenomenon known as shear thinning. This phenomenon is explained by the stretching of entangled molecules, permitting them to move in a more aligned manner, thus, with less resistance (Hou et. al. 2007). The process is completely reversible: viscosity returns to its initial values when shear rate ceases.

If temperature is considered constant, the viscosity-shear rate constitutive relationship for silicone fluid may be modeled by the Yasuda-Carreau equation (Clasen et.al. 2010, Ghannam and Esmail 1998, Swallow 2002, Hou 2008):

$$\frac{\mu-\mu_\infty}{\mu_0-\mu_\infty}=\left[1+\left(\kappa\cdot\dot{\gamma}\right)^a\right]^{\frac{n-1}{a}} \tag{2.9}$$

where μ_0 is the zero shear rate viscosity (valid for low shear rates); μ_∞ is the infinite shear rate viscosity (zero in this case); κ is a characteristic time (the reciprocal of the intercept between the power law line and the zero shear rate viscosity); n is the power law region exponent, a represents the width of the transition region between Newtonian and power law behavior; and $\dot{\gamma}$ is the shear rate magnitude defined as:

$$\dot{\gamma}=|2\mathbf{S}|=\sqrt{\frac{1}{2}(2\mathbf{S}):(2\mathbf{S})} \tag{2.10}$$

As expressed in (2.9), viscosity is only a function of the velocity field and may be considered along with (2.1) through (2.4) and (2.7) to solve just for the fluid dynamics. This case is referred to as isothermal flow, since temperature is assumed constant and constant values of μ_0, κ and a corresponding to the assumed temperature are used.

Although less pronounced than in most liquids, silicone oil exhibits a decrease in viscosity with rising temperature. This can be incorporated into Eq. (2.9) by multiplying μ_0 and κ by a temperature dependent shift factor $Z(T) = \exp(b/T - b/T_{ref})$, where b is a parameter and T_{ref} is a reference temperature to which μ_0 and κ correspond (Swallow 2002). Hence, the complete equation to simultaneously model shear and temperature response adopted in this research is:

$$\mu(\mathbf{u},T) = Z(T)\cdot\mu_0\left(T_{ref}\right)\left\{1+\left[Z(T)\cdot\kappa(T_{ref})\cdot\dot{\gamma}\right]^a\right\}^{\frac{n-1}{a}} \tag{2.11}$$

Applying $Z(T)$ to the viscosity-shear rate relationship for a reference temperature has two effects which can be observed in Figure 2-2 and Figure 2-3. Multiplying μ_0 by $Z(T)$ causes a vertical displacement of the curves corresponding to different temperatures. The second effect intends to emulate the behavior observed by Swallow (2002) during rheological tests of high viscosity silicone gum: viscosity became much less dependent of temperature beyond certain shear rate, where terminal power law flow was found. Thus, multiplying κ by $Z(T)$ causes the curves corresponding to different temperatures to tend to merge as shear rate increases. Considering μ as a function of temperature couples the fluid dynamics and heat transfer and allows the evaluation of additional effects, such as the ones discussed at the beginning of section 2.2.

Two types of silicone oil were used in this research: one with μ_0 = 1 Pa·s at T_{ref} = 25°C (referred to from here on as SF1) and another with μ_0 = 30 Pa·s at T_{ref} = 20°C (referred to from here on as SF30). In the case of SF1, literature reports several different values for κ, α and n (Clasen et. al. 2010; Gelest Inc. 2004; Hou, et.al. 2007; Hou 2008). Herein, the parameters reported by Hou (2008) were adopted, who calculated them by fitting Eq. (2.9) to previous experimental data (Currie and Smith 1950; Lee et. al. 1970) of silicone oil with the same viscosity at 25°C. Parameter b was taken from Ghannam and Esmail (1998). In the case of SF30, rheological analysis for a sample of the silicone oil actually used in the prototype was subcontracted to a specialized laboratory (TA Instruments http://www.tainstruments.com). Incremental shear rate tests were carried out at different constant temperatures with viscosity being measured up to values of approximately 1000 [1/s]. Since much higher values are expected in the damper, an additional ($\dot{\gamma}$,μ) pair for polydimethylsiloxane with μ_0 = 30 Pa·s at 25°C was obtained from a manufacturer's manual (Gelest Inc. 2004). This point was added to the TA Instruments viscosity-shear rate plot corresponding to μ_0 = 30 Pa·s (i.e., at 20°C) and κ, α and n were identified from the resulting curve. Parameter b in this case was calculated by fitting an equation in the form of $\mu_0 = c\cdot\exp(b/T)$ to a plot of the measured values of μ_0 by TA Instruments versus T, with c being a constant. This is an Arrhenius type equation (Ghannam and Esmail 1998) and is equivalent to modeling the zero-shear rate viscosity as $\mu_0 = Z(T)\,\mu_0(T_{ref})$. Please see Appendix A for details on the parameter determination for SF30.

Based on pressure-volumetric contraction data supplied by a manufacturer (Clearco Products), the fluid density ρ was assumed to vary linearly with pressure according to a compressibility coefficient, as in Eq. (2.7), for typical damper operating pressure ranges.

Values of the parameters used in the modeling, except otherwise indicated, are presented in Table 2-1 and the corresponding viscosity-shear rate relationships for SF1 and SF30 are shown in Figure 2-2 and Figure 2-3. These figures clearly show the shear thinning and the effect of the shift factor; applying it to μ_0 causes a parallel displacement of the curves; applying it to κ causes that the curves corresponding to different temperatures tend to merge as shear rate increases. By comparing the two fluids, SF30, which is composed of molecules with greater weight, displays a steeper viscosity decrease as shear rate increases. It will be seen that shear thinning plays a critical role in viscous damper behavior.

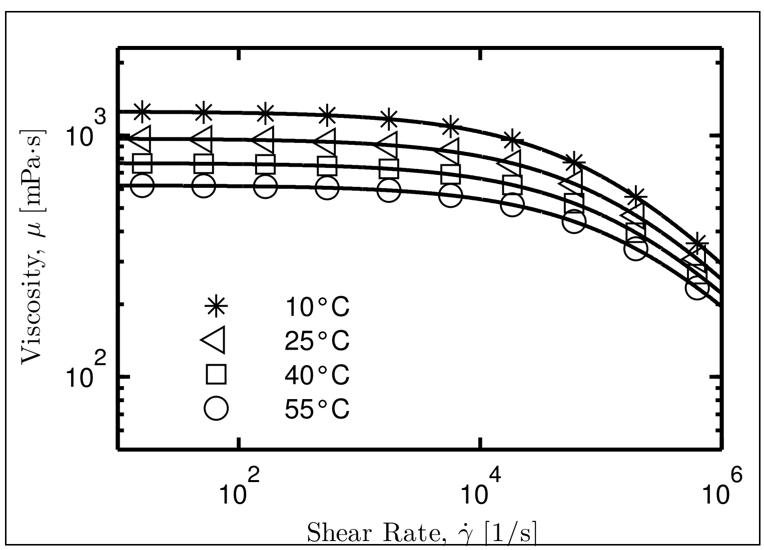

Figure 2-2: Viscosity-shear rate relationship for SF1 at different temperatures.

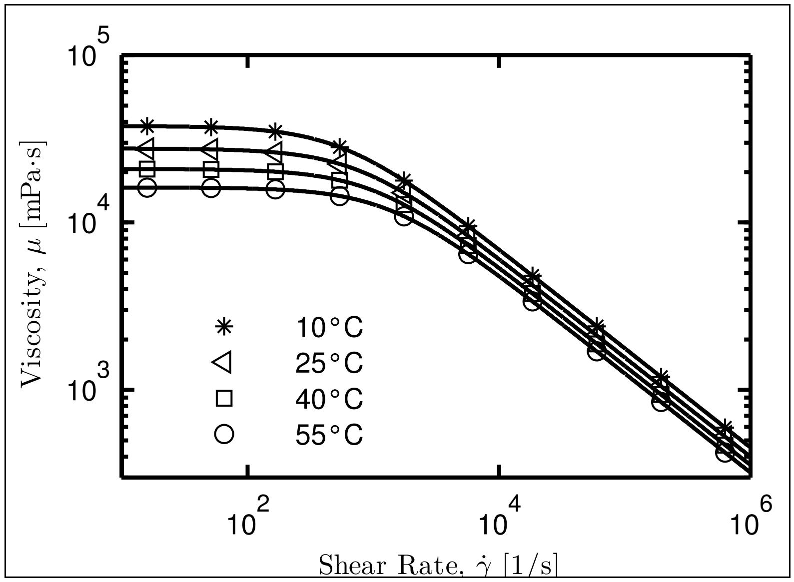

Figure 2-3: Viscosity-shear rate relationship for SF30 at different temperatures.

Table 2-1: Values of parameters used in the modeling

	Value	Units	Description
ρ_{ref}	970	kg/m^3	Fluid density at atm. pressure
p_{ref}	0	*bar*	Gauge reference pressure
T_{amb}	293.15	*K*	Ambient temperature
β	0.9341	GPa^{-1}	Fluid compressibility
κ	7.2e-6; 1.41e-3	*s*	Characteristic time SF1 (25°C); SF30 (20°C)
a	0.6; 1.325		Yasuda exp. SF1; SF30
n	0.43; 0.407		Power law index SF1; SF30
b	1452; 1746	*K*	Shift factor parameter SF1; SF30
C_f	2000	$J/(kg{\cdot}K)$	Fluid specific heat
k_f	4.4	$W/(m{\cdot}K)$	Fluid thermal conductivity
k_s	50.9	$W/(m{\cdot}K)$	Steel thermal conductivity
h	15.0	$W/(m^2{\cdot}K)$	Steel-air heat transfer coeff.
C_s	486	$J/(kg{\cdot}K)$	Steel specific heat
ρ_s	7854	kg/m^3	Steel density

2.4 Domain Deformation

All previous equations are derived from an Eulerian standpoint, in which mesh nodes remain fixed in space, the usual practice in computational fluid dynamics. Nevertheless, in this particular problem the fluid domain continually changes its shape as the piston moves. Fortunately, the mentioned software (COMSOL AB 2008, ANSYS Inc. 2009) is able to integrate these equations in grids that deform. Boundary displacements may be prescribed (the sinusoidal piston displacement in this case), to which the domain conforms by solving a displacement diffusion equation at the beginning of each time step, preserving the relative distribution of the initial mesh (Ansys CFX-Pre User's Guide 2009).

The previous technique is computationally expensive and time consuming. Because of that, Hou (2008) proposed an alternative model in which the analyzed domain remained unchanged at all times and fluid velocity was specified at the nodes located at one end of the fluid domain, generating a flow that resembles the fluid displaced by the movement of the piston. In the opposite end, a zero relative pressure is imposed. All fluid boundaries are immobile rigid walls, in which the no-slip condition applies, that is, fluid velocity is zero relative to the wall (Figure 2-4). This approach is considerably faster, simpler and produces results in excellent agreement with the analogous deforming mesh model. Thus, the imposed flow model was used in parametric analyses of the fluid dynamics of the damper.

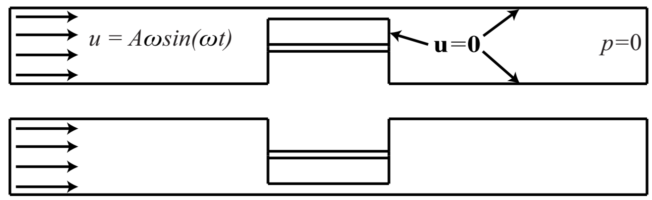

Figure 2-4: Boundary conditions in the imposed flow model.

2.5 Summary of Equations

For convenience, the previous equations are summarized in Table 2-2 . This table shows the three types of formulations solved during this research and the assumptions that lead to them. Depending on the pursued objective, there are: isothermal incompressible flow, isothermal barotropic flow and non-isothermal incompressible flow.

Table 2-2: Summary of the equations that govern the fluid flow and thermal behaviors inside the damper.

General Conservation Equations		
$\frac{\partial \rho}{\partial t}+\nabla\cdot(\rho\mathbf{u})=0$ $\rho\frac{\partial \mathbf{u}}{\partial t}+\rho\mathbf{u}\cdot\nabla\mathbf{u}=-\nabla p+\nabla\cdot\boldsymbol{\tau}$	ρ, T *constants* $\mu(\dot{\gamma})$ $\longrightarrow$	*Isothermal Incompressible Flow* $\nabla\cdot\mathbf{u}=0$ $\rho\frac{\partial \mathbf{u}}{\partial t}+\rho\mathbf{u}\cdot\nabla\mathbf{u}=-\nabla p+\nabla\cdot\mu(\dot{\gamma})\left[\nabla\mathbf{u}+(\nabla\mathbf{u})^T\right]$
$\rho C_p\left(\frac{\partial T}{\partial t}+(\mathbf{u}\cdot\nabla)T\right)=\nabla\cdot(k\nabla T)+\boldsymbol{\tau}:\mathbf{S}$ $\boldsymbol{\tau}=2\mu\mathbf{S}-\frac{2}{3}\mu(\nabla\cdot\mathbf{u})\mathbf{I}$ $\mathbf{S}=\frac{1}{2}\left[\nabla\mathbf{u}+(\nabla\mathbf{u})^T\right]$	T *constant* $\rho(p)$ $\longrightarrow$ $\mu(\dot{\gamma})$	*Isothermal Compressible Flow (Barotropic)* $\frac{\partial \rho}{\partial t}+\nabla\cdot(\rho\mathbf{u})=0$ $\rho\frac{\partial \mathbf{u}}{\partial t}+\rho\mathbf{u}\cdot\nabla\mathbf{u}=-\nabla p+\nabla\cdot\left[2\mu(\dot{\gamma})\mathbf{S}-\frac{2}{3}\mu(\dot{\gamma})(\nabla\cdot\mathbf{u})\mathbf{I}\right]$ $\rho=\rho_{ref}\left[1+\beta\left(p-p_{ref}\right)\right]$
$\dot{\gamma}=\lvert 2\mathbf{S}\rvert=\sqrt{\frac{1}{2}(2\mathbf{S}):(2\mathbf{S})}$ *Note* $\rightarrow$ $\mathbf{a}:\mathbf{b}=a_{nm}b_{nm}$ (*indicial notation*)	ρ *constant* $\mu(\dot{\gamma},T)$ $\longrightarrow$	*Non-isothermal Incompressible Flow* (*Multiphysics*) (Ma<0.3) $\nabla\cdot\mathbf{u}=0$ $\rho\frac{\partial \mathbf{u}}{\partial t}+\rho\mathbf{u}\cdot\nabla\mathbf{u}=-\nabla p+\nabla\cdot\mu(\dot{\gamma},T)\left[\nabla\mathbf{u}+(\nabla\mathbf{u})^T\right]$ $\rho C_p\left(\frac{\partial T}{\partial t}+(\mathbf{u}\cdot\nabla)T\right)=\nabla\cdot(k\nabla T)+\boldsymbol{\tau}:\mathbf{S}$ *Viscosity's temp. dependence couples the momentum and energy equations*

$\mathbf{u}$	: *velocity field*	$\boldsymbol{\tau}$	: *stress tensor*	ρ_{ref}	: *density at reference pressure*	μ	: *dynamic viscosity* (*see Fluid Properties Section*)
p	: *pressure field*	β	: *fluid compressibility*	k	: *conductivity*		
T	: *temperature field*	$\mathbf{S}$	: *strain rate tensor*	C_p	: *specific heat at constant pressure*		
ρ	: *fluid density*	$\dot{\gamma}$	: *shear rate*	p_{ref}	: *reference pressure*		

3. PARAMETRIC ANALYSES

Parametric analyses were performed to study how geometric dimensions and fluid properties affect the velocity exponent α (Eq. (1.1)) of pistons with annular orifices or drilled cylindrical orifices. Instead of independently varying different dimensions, for instance gap width h in the annular case, a single parameter, representative of the general geometric relationships, that correlated with α was derived for each configuration. Since the interest was solely on force-velocity relationships, isothermal fluid dynamics was considered with μ_0 and κ corresponding to 25°C for SF1 and 20°C for SF30. Furthermore, in order to alleviate computational cost, imposed flow models and fluid incompressibility were assumed throughout this section.

3.1 Annular Orifice Geometry

Considerable insight is gained by first solving analytically a simplified version of this problem. In Figure 3-1, when $h \ll R_p$, flow through the annular region can be idealized as flow between parallel plates (Soong and Dargush 1997). Two limit cases may then be considered: prevalence of viscous effects or prevalence of inertial effects. (Please refer to Appendix B for a complete derivation of the following equations.) Assuming stationary flow, a Newtonian incompressible fluid, neglecting the piston's velocity, approximating the output force as $A_p \cdot \Delta p$ and neglecting convective acceleration in the momentum balance equation, the former limit case yields:

$$F_{viscous} = \frac{\left(R_p^{\,2} - R_v^{\,2}\right)^2 6\pi\mu_0 L_p}{R_p h^3} V \tag{3.1}$$

which results in a linear relationship between output force and piston velocity. If the same assumptions are made, but this time ignoring the viscosity instead of the convective acceleration, a quadratic relationship between force and velocity results:

$$F_{inertial} = \frac{\rho\pi\left(R_p^{\,2} - R_v^{\,2}\right)^3}{8R_p^{\,2}h^2}V^2 \tag{3.2}$$

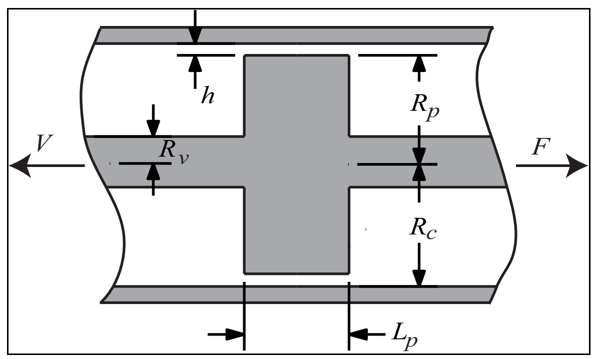

Figure 3-1: Annular orifice geometry.

Using an idea presented by Li et. al. (2006), the quotient of these two expressions offers an indication of how different parameters influence two very dominant trends of damper behavior.

$$\frac{F_{inertial}}{F_{viscous}} = \frac{\rho\left(R_p^{\,2} - R_v^{\,2}\right)h}{48\mu_0 L_p R_p}V \tag{3.3}$$

As density, velocity, piston radius and gap width increase, force-velocity will tend to a quadratic relationship ($\alpha = 2$). As viscosity and piston length increase, the behavior will tend to be linear ($\alpha = 1$). The quotient in (3.3) is, not surprisingly, related to the Reynolds number for flow between parallel plates, defined as $\mathrm{Re} = \rho Vh / \mu$.

For the fluids and the range of frequencies (up to 2 *Hz*) and amplitudes (up to 20 *cm*) considered in this thesis, flow dominated by viscous rather than inertial effects prevails largely in annular orifice dampers that produce a reasonable output force relative to their size. Accordingly, Reynolds numbers in the gap for the modeled configurations are low, generally Re < 100. As mentioned, this would result in a linear damper if the fluid was Newtonian, yet this is not the case for SF1 and SF30. Hou et. al. (2007) showed that shear thinning had a significant impact on the behavior of dampers filled with silicone oil, making the force-velocity relationship deviate from linear to $\alpha < 1$. This phenomenon is induced by the no slip condition. Inside the gap the velocity profile will resemble a parabolic shape (it would be parabolic in the case of a Newtonian fluid, theoretically). Maximum velocity, achieved approximately halfway through the gap (*h/2*), will have to compensate for the fluid with zero relative velocity at the walls, developing steep velocity gradients in that zone. Thus, shear rate enters the non-Newtonian range and the fluid thins. As the flow through the gap increases, viscosity will decrease even further. Force will therefore increase at a lower rate than linear as piston velocity increases, i.e., $\alpha < 1$.

It is intuitive that the amount the fluid thins will be related to the area of the annular orifice and the cross section area of the fluid chamber. For a given piston velocity, the smaller the ratio between these two, the greater the velocity in the gap and shear thinning. Average velocity in the gap can be estimated using continuity:

$$v_{ave} = \frac{\pi\left[\left(R_p + h\right)^2 - R_v^{\,2}\right]}{2\pi R_p h} V \tag{3.4}$$

The shear rate magnitude inside the gap may be roughly estimated assuming, for example, a linear velocity profile within the gap (Hou et. al. 2007). At maximum piston velocity, the corresponding average shear rate is:

$$\dot{\gamma}_{ave} = \frac{2v_{ave}}{h/2} = \frac{2\left[\left(R_p + h\right)^2 - R_v^2\right]}{R_p h^2} A \cdot 2\pi f \tag{3.5}$$

With shear thinning as the foremost cause of behavior to deviate from linear, $\dot{\gamma}_{ave}$ is a natural candidate to correlate with α. Consequently, a vast number of simulations were carried out with different combinations of R_p, R_v, h, L_c, A and f. The considered maximum input velocities ranged from 10 *cm/s* to 50 *cm/s* and gap widths h ranged from 10% to approximately 0.1% of R_p. To reduce calculation time, axisymmetry of the annular orifice geometry was used with the assumption that all variables were independent of the tangential coordinate and velocity was zero in that direction. After solving each case, α-values were fitted to the resulting force-velocity curves and plotted against its corresponding $\dot{\gamma}_{ave}$ as shown in Figure 3-2, evidencing the significant impact of shear thinning. Please see Appendix C for details on the geometries and results corresponding to the solved models.

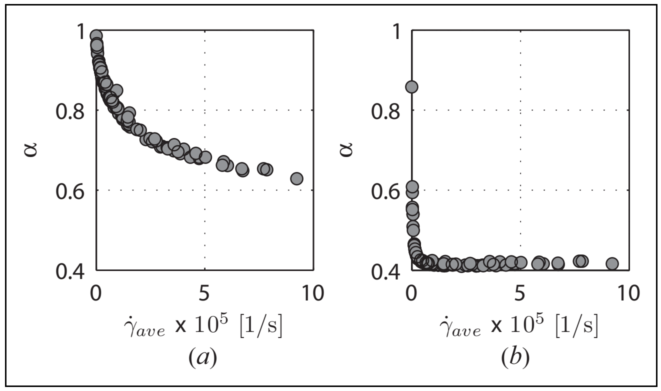

Figure 3-2: Variation of velocity exponent α as a function of average shear rate: (a) SF1, (b) SF30.

While SF1 displays a more gradual decrease in α as $\dot{\gamma}_{ave}$ increases, SF30 displays a sudden decline with α stabilizing at approximately 0.41. This is consistent and intimately related to the rheological behavior of the considered fluids, Eq. (2.9). Both curves in Figure 3-2 tend asymptotically to the value of parameter n, 0.43 for SF1 and 0.407 for SF30; while this trend is evident in the case of SF30, much higher shear rates would be needed to make it apparent in Figure 3-2 (a). How fast this asymptotic value is reached depends on parameter a.

Please note that no values of α greater than 1 were obtained, indicating that inertial effects, which would be responsible of generating exponents greater than unity, do not play a significant role in annular orifice configurations for the fluids and velocity range considered. Moreover, α-exponents close to one were only generated with values of $\dot{\gamma}_{ave}$ leading to negligible output forces in relation to damper size. In contrast, low values of α in the case of SF1 were generated with geometries that led to unrealistically high output forces. Considering that a "reasonable" geometric ratio

h / R_p would be close to 1%, SF1 would be associated to α-values in the range of 0.8 to 0.9, while SF30 to values of α close to 0.4.

3.2 Piston with Cylindrical Orifices

Again, we begin by analytically studying the two limit trends of behavior, dominance of viscous or inertial effects. (Please refer to Appendix B for a complete derivation of the following equations.) With the same assumptions as before and referring to Figure 3-3, the viscous case yields:

$$F_{viscous} = \frac{8\pi\mu_0 L_o \left(R_p^{\ 2} - R_v^{\ 2}\right)^2}{NR_o^{\ 4}} V \tag{3.6}$$

where N is the number of orifices in the piston. On the other hand, the inertial case resolves to:

$$F_{inertial} = \frac{\rho\pi\left(R_p^{\ 2} - R_v^{\ 2}\right)^3}{2N^2 R_o^{\ 4}} V^2 \tag{3.7}$$

Once more, the viscous limit case relates force and velocity linearly, while the inertial limit case quadratically. Dividing Eq. (3.7) by (3.6) yields:

$$\frac{F_{inercial}}{F_{viscous}} = \frac{\rho\left(R_p^{\ 2} - R_v^{\ 2}\right)}{16\mu_0 N L_o} V \tag{3.8}$$

As density, piston radius and velocity increase, inertial effects will become more important and α will tend to values greater than one. As viscosity, number of orifices and orifice length increase, viscous effects will become more important and α will tend to one (Li et. al. 2006) or less, depending on how much the fluid thins as discovered in the previous subsection.

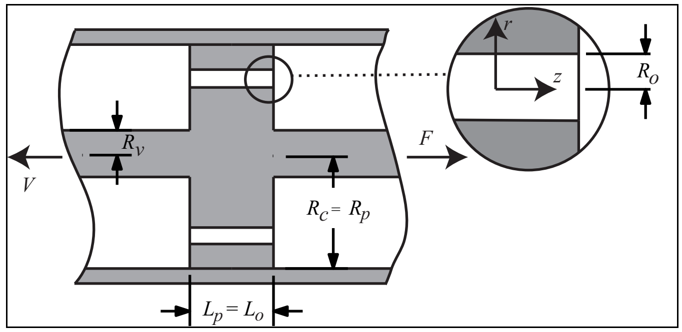

Figure 3-3: Geometry of the piston with cylindrical orifices.

Unlike the annular orifice configuration, inertial effects are more likely to dominate in flow through cylindrical orifices because there will be less fluid-solid contact area where the no slip condition causes viscous effects to prevail – naturally, this is true as long as the piston does not have too many, very small orifices. Hence, in addition to the previous focus on viscous flow and shear thinning, the cylindrical orifice case requires to account for an additional source of non-linearity, inertial effects advocating for $\alpha > 1$.

Shear rate within the orifices was estimated using continuity and assuming a parabolic velocity profile. The average shear rate for such a profile is:

$$\dot{\gamma}_{ave} = \frac{8v_{ave}}{3R_o} \tag{3.9}$$

and the corresponding average velocity at each orifice is:

$$v_{ave} = \frac{V \cdot \pi\left(R_p^{\,2} - R_v^{\,2}\right)}{N} \cdot \frac{1}{\pi R_o^{\,2}} \tag{3.10}$$

By substituting $\dot{\gamma}_{ave}$ in the Yasuda-Carreau equation, an average value of dynamic viscosity inside the orifice, μ_{ave}, can be obtained to replace μ_0 in Eq. (3.8) to account for shear thinning. The resulting expression leads to the parameter used in this case to correlate with α:

$$k_c = \frac{\rho\left(R_p^{\ 2} - R_v^{\ 2}\right)}{16\mu_{ave} N L_o} V_{\max} \tag{3.11}$$

A great number of models with different geometric dimensions and covering a wide range of k_c values were analyzed. Maximum input velocities ranged from 1 to 100 *cm/s*, orifice number from 2 to 40, piston lengths from 3 to 25 *cm*, piston radii from 5 to 15 *cm* and orifice radii from 1 to 10 *mm*. Please see Appendix C for details on the geometries and results corresponding to the solved models.

Contrary to the annular configuration, axial symmetry is lost in this case. However, an alternative method was implemented by modeling flow at each orifice independently, allowing the use of 2D axisymmetric coordinates. In the imposed flow approach, the total flow rate entering (or leaving) the fluid domain is $Q = \pi(R_p^{\ 2} - R_v^{\ 2})V$ and this flow rate is distributed among the N orifices. Since pressure is nearly uniform in each chamber, the orifices work in parallel and flow rate through each one is driven by the same pressure differential. Thus, flow rate through each orifice will depend on its own dimensions only. The simplest scenario is for equal orifices, as each flow rate q_i equals Q/N.

Taking the previous idea into account, the model used in the parametric analysis imposed the flow rate in an axisymmetric configuration of a single orifice and the corresponding Δp was determined. The corresponding geometry and boundary conditions used are shown in Figure 3-4. With the resulting pressure-flow rate relationship, damper output force was calculated using $F=A_p\cdot\Delta p$ and piston velocity with $V=q_iN\pi(R_p^{\,2}-R_v^{\,2})$.

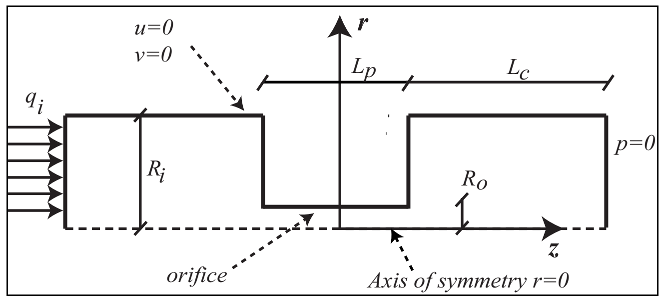

Figure 3-4: Model and boundary conditions used for parametric flow analysis of piston with cylindrical orifices.

Values of k_c versus α are plotted for each model in Figure 3-5, in which results are grouped according to similar levels of average shear rate (or μ_{ave}). It is apparent that as k_c increases, α also increases. For SF1 (Figure 3-5 (a)) exponents of $\alpha>1$ are easily achieved, unlike the annular orifice case, indicating that inertial effects play an important role in this type of configuration. Theoretically, the upper limit for α is 2, corresponding to fully developed turbulent flow in a pipe. For SF30 (Figure 3-5 (b)) the trend becomes clearer as average shear rate increases (μ_{ave} decreases), since high viscosities do not allow to achieve greater values of k_c. The α-value for the lowest k_c decreases as the shear rate increases due to shear thinning. For SF30 it seems to reach a lower limit at ~ 0.4 (again, the value of parameter n) as in the annular orifice geometry; hence, the lower limit for α is equal in both configurations. In comparison, cylindrical orifices offer more flexibility if exponents greater or close to one are desired by using a fluid of lower viscosity, such as SF1.

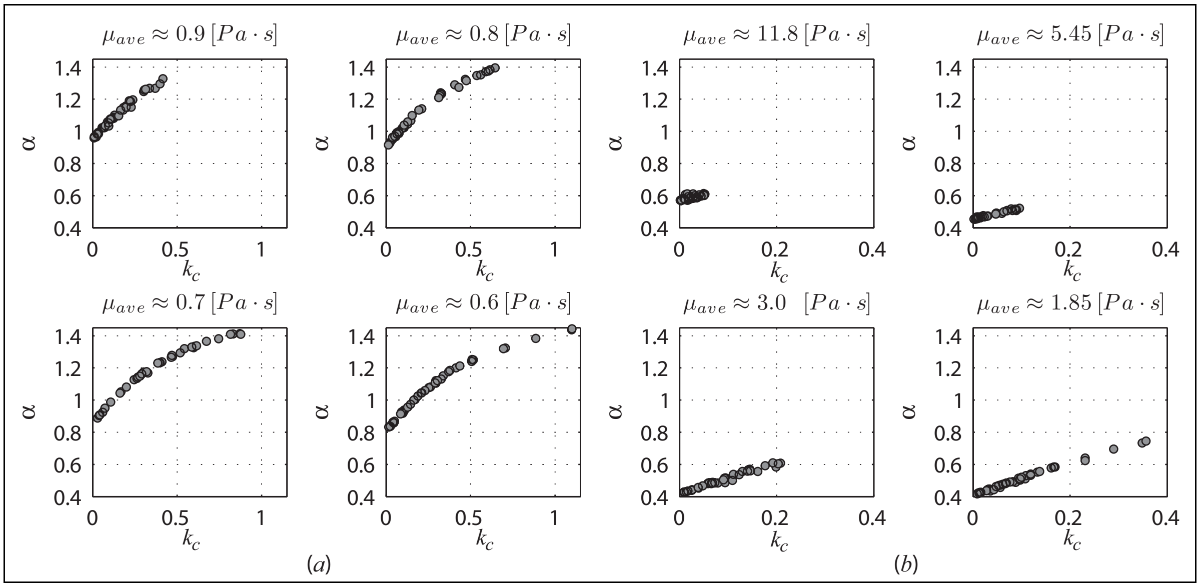

Figure 3-5: Relationship between the α-values and parameter k_c (Eq.(3.11)) for different values of μ_{ave}: (*a*) SF1, (*b*) SF30.

Results grouped under μ_{ave} = 11.8 *Pa·s* in Figure 3-5 (b) concentrate at very low values of k_c since the high μ_{ave} does not permit greater values given the range in which the other variables in k_c were decided to fluctuate.

3.3 Combining Different Types of Orifices

The independent orifice approach may be generalized to cover more complex cases, such as pistons with cylindrical orifices of different diameters, combinations of cylindrical and annular orifices or, ultimately, combinations of any kind of orifices. Again, the objective of this approach is to develop a technique that is sufficiently accurate, but computationally much more economical than modeling the complete piston geometry in 3D to obtain the force-velocity relationship.

The underlying principle is the same as previously explained; orifices in parallel share the same Δp across them and may be analyzed independently. If all orifices are not the same, a different flow rate will correspond to each type for a given Δp. However, if a pressure-flow rate curve is calculated for each orifice, the total flow rate Q passing through the piston may be obtained by horizontally adding the flow rates of each orifice at different Δp values. The damper force at that instant may then be approximated by $F=A_p{\cdot}\Delta p$ and the corresponding piston velocity calculated from $V = Q\,/\,\pi(R_c^{\,2} - R_v^{\,2})$. This is graphically explained in Figure 3-6.

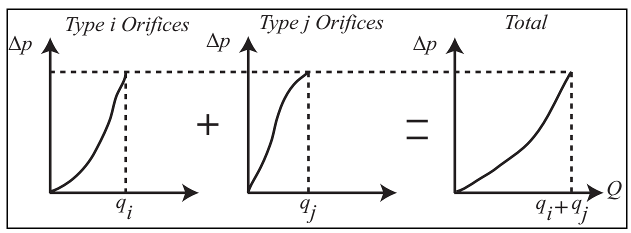

Figure 3-6: The left side shows the pressure-flow rate relationship for each different type of orifice. The pressure flow rate relationship for the complete piston may be derived by adding the flow rates.

Section 4 will show an example where an annular orifice was combined with cylindrical orifices to accomplish a target behavior.

3.4 Variable Area Orifice

In general, low values of exponent α are preferred for structural applications. Dampers with high α will develop excessive peak forces that may damage braces and connections if unexpected high velocities occur, for example, under near fault ground motion (Valdebenito et. al. 2010). On the contrary, peak forces will certainly be more controlled if α is low. A low exponent damper will also be more efficient and dissipate a greater amount of energy at similar levels of maximum force: its force-displacement curve will resemble a rectangle while a linear damper's curve, for example, will be elliptical.

In an effort to generate lower exponents than those achievable with cylindrical or annular orifices, an orifice with an area that varies as Δp increases was briefly studied. Simply put, this means using valves. To evaluate the potential of this idea, a cylindrical orifice with a spring loaded valve core attached at one of its ends was modeled, as seen in Figure 3-7. This is a fluid-structure interaction problem: as the drag force exerted by the fluid increases, the valve core repositions by compressing the spring, making the area available for fluid flow greater. To enhance the non linear effect, a preload was considered for the spring, thus the valve core only starts moving once the force exerted on it due to the flow exceeds the preload, F_0. Figure 3-8 shows the pressure-flow rate relationship obtained with SF30 for the following values: d_o = 8[*mm*], v_n = 3.3[*mm*], v_t = 4.6[*mm*], L_v = 15[*mm*], d_r = 1.3[*mm*], K = 160[*N/mm*] and F_o = 450[*N*]. The mass of the valve core was not considered in this model, but it may be, in which case the valve core-spring system becomes a dynamic system. Several of this type of orifices can be used in a piston, or even combined with other types, to achieve a desired behavior. The force-velocity relationship of the complete device may be then predicted with the independent orifice approach.

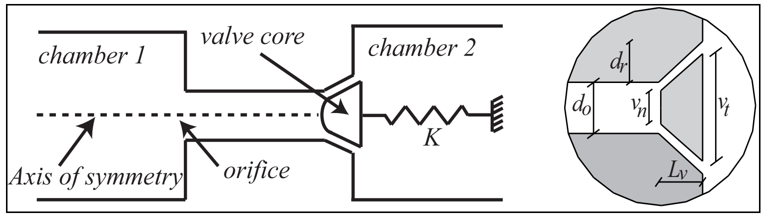

Figure 3-7: Variable area orifice model.

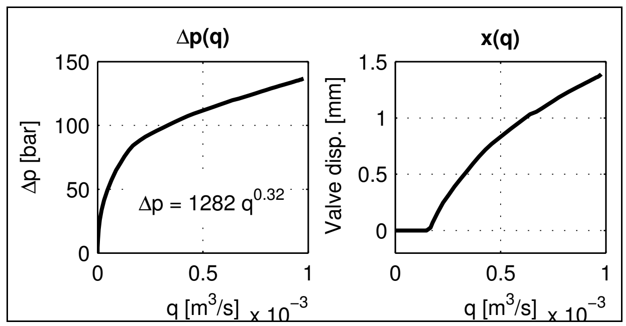

Figure 3-8: Pressure-flow rate relationship and valve core displacement for the modeled variable orifice.

It was previously seen that with annular or cylindrical orifices, the lowest achievable exponent was $\alpha = 0.41$; in this specific case, the variable orifice produced a considerably lower exponent of 0.32, demonstrating the effectiveness of this idea and its potential for obtaining even lower exponents. Furthermore, if the valve core is externally controllable, a semi-active device may be developed. These aspects certainly represent lines for future investigation.

4. DAMPER DESIGN

Based on the previous results, a full scale prototype with a ± 20 *cm* stroke, nominal capacity of 600 *kN,* and exchangeable piston was manufactured and tested in three different configurations. Other geometric dimensions common to all tested configurations of the device are internal radius R_c = 12 *cm*, wall thickness of 4.6 *cm*, radius of the piston rod R_v = 3.75 *cm* and cylinder length 60 *cm*. Images of the used meshes and post-process images of interesting results while simulating these designs can be seen in Appendix D.

The adopted design process is represented as a flow diagram in Figure 4-2. The first step consists in establishing target values for α and C, the two parameters that characterize damper behavior according to Eq. (1.1). However, an equivalent more straightforward alternative is to select a maximum force to be reached at a certain velocity. The next step is to choose a configuration and fluid viscosity that is compatible with the target values. For instance, the previous analysis showed that SF30, due to its more pronounced shear thinning, is more suitable than SF1 to produce low α-exponents, and that cylindrical orifices usually lead to higher α-exponents than annular orifices. The general procedure for both annular and cylindrical orifices is similar: the first step is to determine the parameter value ($\dot{\gamma}_{ave}$ for annular; k_c for cylindrical) that yields the target α. There is freedom to select the geometric properties of the damper as long as they satisfy Eq. (3.5) and Eq. (3.11). Because there are infinite combinations that yield a specific $\dot{\gamma}_{ave}$ or k_c value, several iterations may be needed until certain criteria, such as design feasibility, other geometric constraints, and minimum cost, is achieved. The remaining dimensions are determined by estimating the maximum force based on analytical viscous limit case approximations adapted to incorporate shear thinning. For the annular configuration this is:

$$F_{est\ annular} = \frac{6\pi\left(R_p{}^2 - R_v{}^2\right)^2 \mu_{ave} L_p}{R_p h^3} V \tag{4.1}$$

where μ_{ave} is the average viscosity obtained by replacing the corresponding $\dot{\gamma}_{ave}$ value, Eq.(3.5), into the Yasuda-Carreau equation, Eq. (2.9). For cylindrical orifices, the viscous limit case force is $F_{cv}=8\pi(R_p{}^2-R_v{}^2)^2\mu_{ave}L_oV/NR_o{}^4$, where μ_{ave} is calculated by replacing $\dot{\gamma}_{ave\ cyl}$ (Eq. (3.9)) into the Yasuda-Carreau equation. However, in the cylindrical orifice case inertial effects cannot be neglected. To resolve this, it was found that the percentage by which the maximum forces obtained in the parametric analysis models differed from F_{cv}, correlated almost linearly with k_c, as shown in Figure 4-1 for SF1.

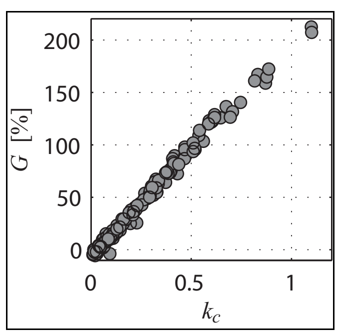

Figure 4-1: Difference between maximum damper forces obtained in the cylindrical orifice parametric analysis and maximum forces approximated considering the viscous limit case for SF1: $G = (F_{model} - F_{cv}) / F_{cv}$

Therefore, force in the cylindrical orifice case may be estimated through the expression:

$$F_{est\ cyl} = G\left(k_c\right) \cdot \frac{8\pi\left(R_p{}^2 - R_v{}^2\right)^2 \mu_{ave} L_o}{nR_o{}^4} V \tag{4.2}$$

where $G(k_c)$ may be obtained from Figure 4-1 for SF1 and μ_{ave} calculated by replacing $\dot{\gamma}_{ave\ cyl} = 8v_{ave} / 3R_o$ into Eq. (2.9). Again, the dimensions resulting from this process may not satisfy some design criteria and several iterations may be necessary.

A third alternative presented in Figure 4-2 is to combine annular and cylindrical orifices based on the independent orifice approach. First, the target force-velocity relationship is approximated with a pressure-flow rate relationship $\Delta p(Q)$ assuming values for R_p and R_v. Next, dimensions for the annular orifice are assumed and the corresponding pressure-flow rate relationship, $\Delta p(q_a)$, estimated with, for example, Eq. (4.1). Since Δp is nearly uniform at each chamber, the pressure-flow rate relationship for the cylindrical orifices, $\Delta p(q_c)$, is obtained by subtracting q_a from Q at different Δp values. The resulting $\Delta p(q_c)$ relationship will have an associated α_c and a certain $(q_c)_{max}$ that should be reached at Δp_{max}. With these target values, the remaining dimensions (N, R_o and L_o) are determined using the same procedure as for the cylindrical orifices, and design iterations may be needed as indicated. In one of the designs presented in this research (Design 1, subsection 4.1), the cylindrical orifice $\alpha > 1$ trend for SF1 is compensated with the $\alpha < 1$ trend of the annular orifice case.

Since only approximate expressions were involved up to this point, the final geometry needs to be verified using a fluid dynamics model. Finally, multiphysics should be incorporated to evaluate temperature-viscosity related effects. These last steps can be complemented with experimental work.

Table 4-1 summarizes the three designs presented herein in terms of configuration, target behavior, type of fluid, general dimensions and tests performed on them, including the initial fluid temperature. Additional objectives for Designs 2 and 3 were to calibrate the rheological parameters.

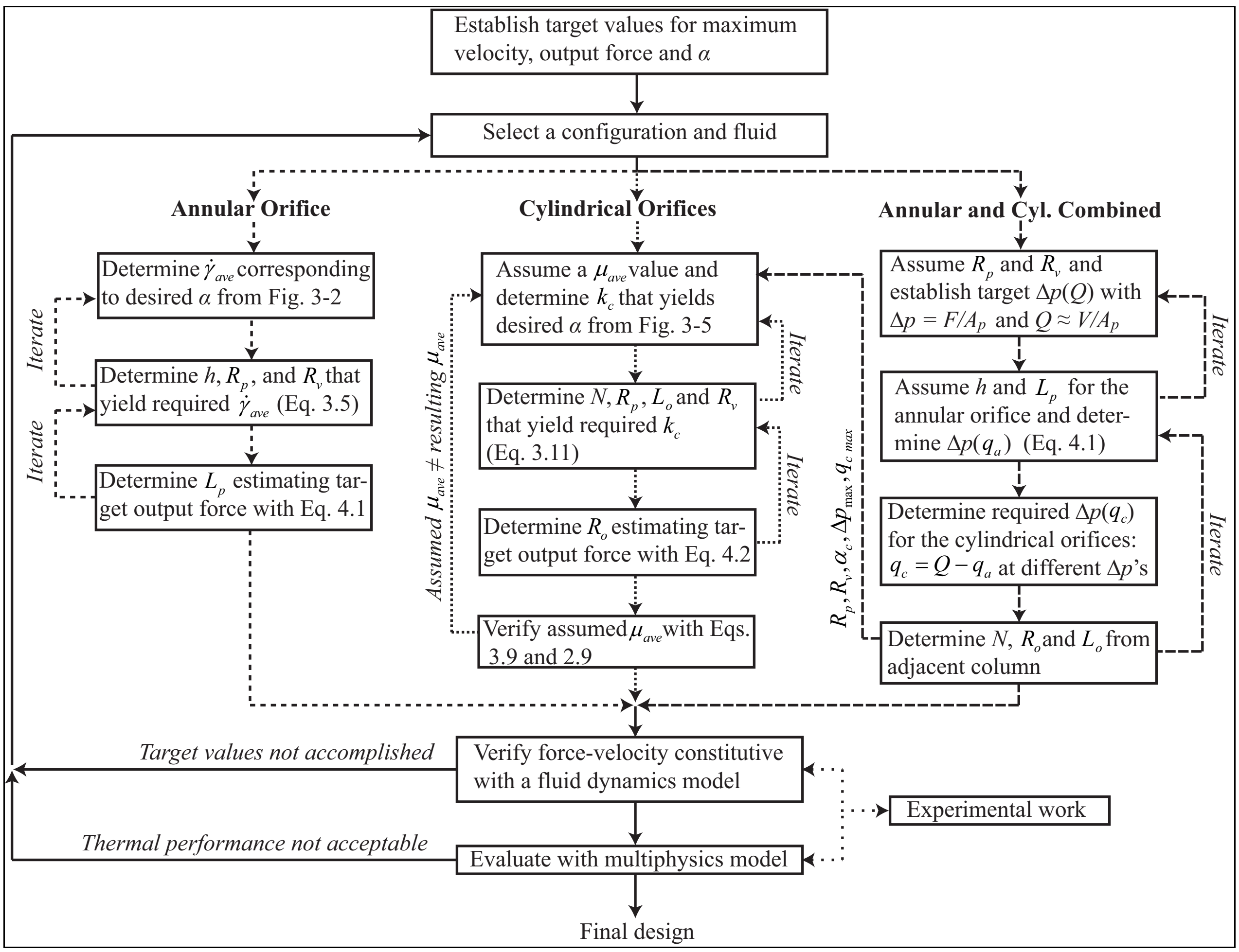

Figure 4-2: Flow diagram representing the design process.

Table 4-1: Summary of the three damper designs.

Design	Objectives	Fluid	General Dimensions	Performed Tests				
				ID	A [cm]	f [Hz]	$V_{\max}$ [cm/s]	T_i [°C]
1 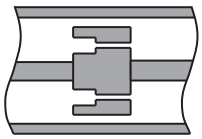	α = 1.0 and F = 600 kN at V = 46.5 cm/s	SF1	$h = 1.0\ mm,\ L_p = 15\ cm$ $R_o = 2.0\ mm,\ L_o = 10\ cm$ $N = 10$	1-1	12.4	0.14	10.9	27.6
				1-2	20.0	0.14	17.6	19.8
2 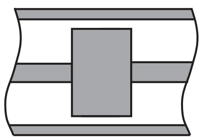	$\alpha \approx$ 0.85 and F $\approx$ 450 kN at V = 16.5 cm/s Model calibration	SF1	$h = 1.0\ mm$ $L_p = 15\ cm$	2-1	12.4	0.21	16.4	26.5
				2-2	2.0	1.0	12.6	28.6
3 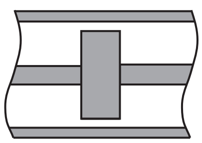	$\alpha \approx$ 0.45 and F $\approx$ 600 kN at V = 14 cm/s Model calibration	SF30	$h = 1.4\ mm$ $L_p = 10\ cm$	3-1	12.4	0.21	16.4	20.0
				3-2	5.0	0.5	15.7	30.7

4.1 Detailed Example: Linear Damper

The goal of Design 1 was to produce a linear damper (α = 1) able to achieve a force of 600 kN at a maximum velocity of 46.5 cm/s. Since SF30 shear thins very quickly, SF1 was chosen. However, shear thinning in SF1 is still sufficient to cause α < 1 in annular orifice configurations. A piston with cylindrical orifices, on the other hand, will easily achieve exponents equal to one or greater, as shown in Figure 3-5 (a). Although the latter is a viable option to achieve the α = 1 objective, it presents some slight difficulties such as the need for many small diameter orifices and seals between piston and cylinder. Alternatively, a combination of annular and cylindrical orifices was chosen, seeking that they would compensate each other's tendencies (α < 1 for annular and α > 1 for cylindrical orifices) and produce a linear outcome.

First, the use of a cylinder with radius R_c = 12 *cm* was established and a gap of 1 *mm* and length L_p = 15 *cm* were considered appropriate for the annular orifice. With the annular orifice selected, Figure 4-3 shows three pressure-flow rate relationships: the target considering all orifices (relationship is linear), the one resulting for the annular orifice and the one required for the cylindrical orifices, i.e., the subtraction of the previous two.

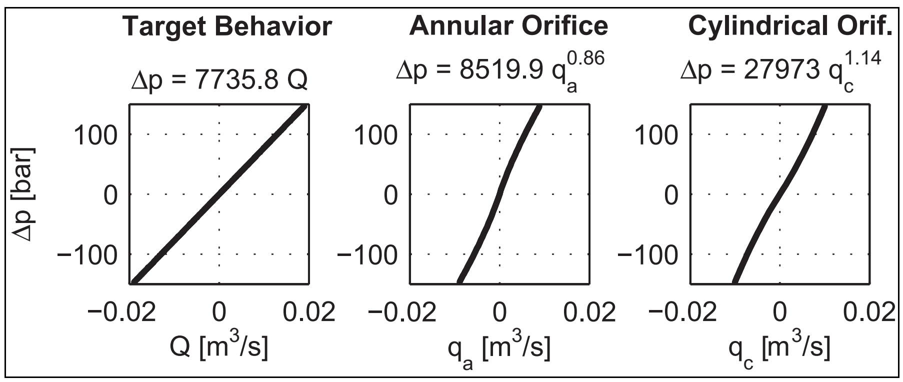

Figure 4-3: Pressure-flow rate relationships for the design of the linear damper.

With this, completing the design reduces to determining the dimensions and number of cylindrical orifices that generate the required pressure-flow rate curve. Figure 3-5 (a) shows that for SF1 experimenting an average shear rate associated to a viscosity of 0.6 $Pa \cdot s$ inside the orifices, $k_c \approx 0.35$ produces the sought velocity exponent of 1.14. A word of caution regarding the calculation of k_c and other expressions presented in subsection 3.2: piston velocity V should be replaced with $q_c / \pi(R_c^2 - R_v^2)$ where q_c is the flow rate through all the cylindrical orifices. The use of V corresponds to the case of a piston consisting solely of cylindrical orifices. Since part of the total flow is through the annular orifice in this case, that term needs to be adapted. For instance, V_{max} in Eq. (3.11) should be replaced with $V_{max} = q_{c\ max} / \pi(R_c^2 - R_v^2)$.

The other condition that must be satisfied is that Δp_{max} at $q_{c\ max}$ should be $\approx$ 145 *bar*, the required pressure differential to produce the output force of 600 *kN*. To estimate Δp_{max}, Eq.(4.2) was used assuming $R_p \approx R_c$:

$$\begin{aligned}
\Delta p_{\max} &= \frac{8\mu_{ave} L_o q_{c\ max}}{\pi N R_o^4} \cdot G\left(k_c\right) \\
\mu_{ave} &= \mu_0 \left[1 + \left(\kappa \left|\dot{\gamma}_{ave}\right|\right)^a\right]^{\frac{n-1}{a}} \\
\dot{\gamma}_{ave} &= \frac{8 q_{c\ max}}{3\pi N R_o^3}
\end{aligned} \tag{4.3}$$

The following dimensions were found to satisfy simultaneously all previous conditions and represent a feasible option in terms of manufacture: N = 10, R_o = 2 *mm*, L_o = 10 *cm*, which yield k_c = 0.35, μ_{ave} = 0.55 $Pa \cdot s$ and Δp_{max} = 144 *bar*. From Figure 4-1, $G(k_c)$ was established as 1.6.

5. NUMERICAL AND EXPERIMENTAL RESULTS

5.1 Force Velocity Results

The prototype was connected to a dynamic actuator which imposes prescribed displacements along its axis, with maximum loading capacity 980 *kN*, stroke +/-50 *cm* and, due to pump limitations, a maximum achievable velocity of approximately 17.5 *cm/s*. The experimental setting is shown in Figure 5-1. Actuator displacement and the damper output force were recorded by a data acquisition system. Additionally, pressure at each chamber was recorded with transducers and monitored to ensure operation below 500 *bar* and fluid temperature was measured at one point inside the fluid chamber (at one of the cylinder caps) and at the housing cylinder's outer surface. In each test, frequency was held constant and the amplitude increased from zero up to the target level; after that, a minimum of five complete cycles were counted. (Results for all the performed tests and treatment of the raw data are detailed in Appendix E.)

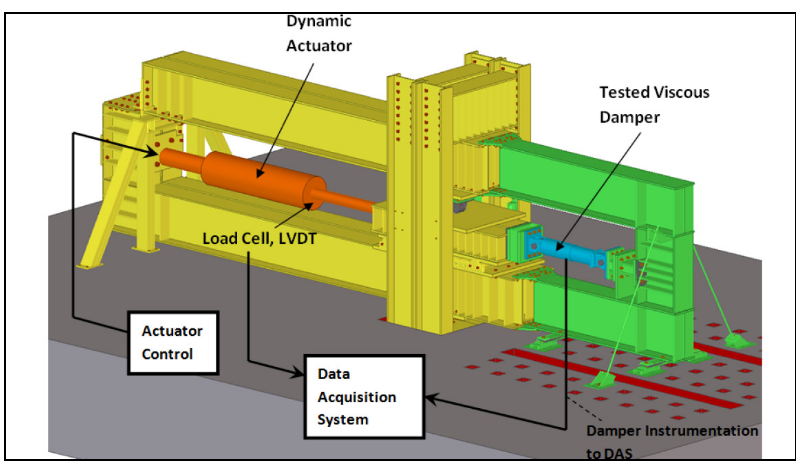

Figure 5-1: Experimental setting.

Displayed in Figure 5-2 through Figure 5-4 are the numerical and experimental force-velocity and force-displacement relationships obtained for the performed tests. The numerical results presented correspond to imposed flow models with compressibility; in these results heat transfer was neglected and temperature was kept constant at the initial fluid temperature (T_i in Table 4-1). For the annular configurations (Designs 2 and 3 in Table 4-1), two-dimensional axisymmetric coordinates were employed; for Design 1, the fluid domain consisted in a three-dimensional symmetric portion of the cylinder, considering the annular and cylindrical orifices simultaneously, not independently.

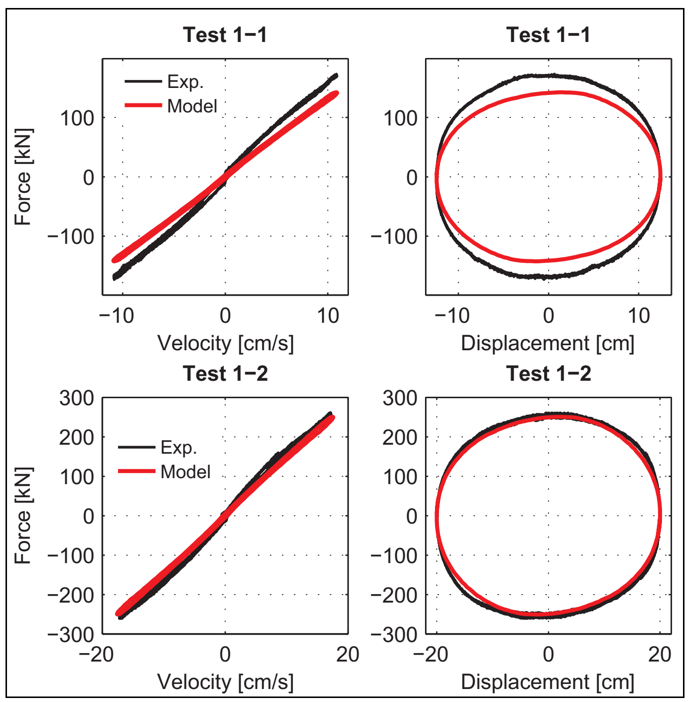

Figure 5-2: Experimental and numerical results for Design 1.

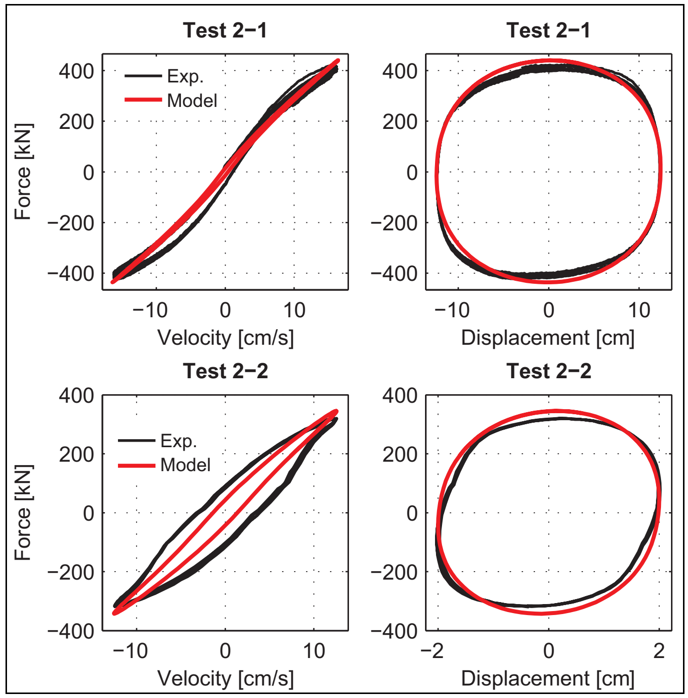

Figure 5-3: Experimental and numerical results for Design 2.

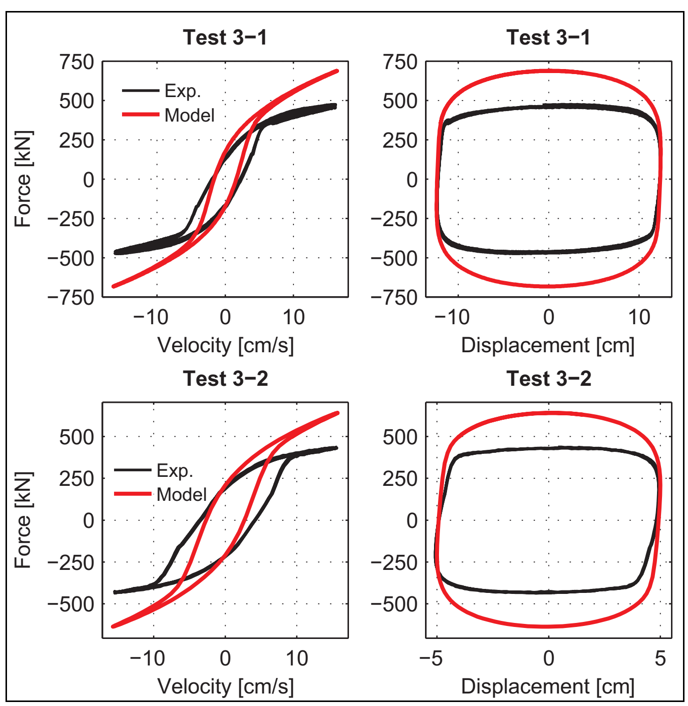

Figure 5-4: Experimental and numerical results for Design 3.

It is apparent from these figures that for Designs 1 and 2 (SF1), the predicted and measured force-velocity relationships show reasonable accuracy in terms of maximum force, though their α-values differ. For Design 3 (SF30), discrepancies are greater, both in maximum force and α-value (See Table 6-1). This is not surprising given the non-linear constitutive behaviors adopted to represent the fluids. For SF1, reported values for the Yasuda-Carreau parameters a, n and κ exist in the literature (Clasen et. al. 2010, Hou 2008, Hou et. al. 2007), but without general consensus; the used values (Table 2-1) were taken from Hou (2008). For SF30, these parameters were roughly estimated, as explained in detail in Appendix A.

To improve the accuracy of the numerical models, the Yasuda-Carreau parameters for each fluid were calibrated using Tests 2-1 and 3-1. Eq. (4.1), with V assuming a range of values, was used to construct analytical force-velocity curves. Since $F_{est\ annular}$ is a function of a, n and κ through μ_{ave}, these parameters were varied until the curve that best fit the experimental data was obtained. This procedure is explained in more detail in Appendix F. The resulting a, n and κ values are presented in Table 5-1, with κ corresponding to the reference temperatures of the fluids, 20°C for SF30 and 25°C for SF1. Tests 2-1 and 3-1 were specifically used because of the low hysteresis exhibited in their force-velocity relationships, an effect that Eq. Eq. (4.1) is not able to reproduce.

Table 5-1: Optimal Yasuda-Carreau parameters resulting from the fit of Eq. (4.1) to Tests 2-1 and 3-1.

Fluid	a	n	κ
SF1	2.0	0.44	4.03e-5 [s]
SF30	2.0	0.33	1.46e-3 [s]

Figure 5-5 displays a comparison between the experimental results and models using the calibrated parameters (Table 5-1) with greatly improved accuracy. Quantitative results for maximum forces and α-values are presented in Table 6-1.

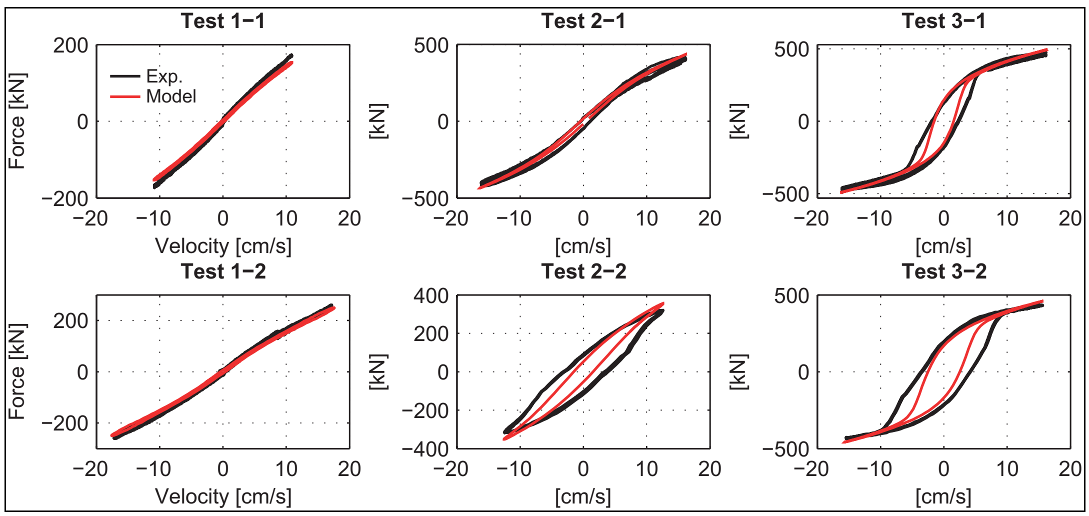

Figure 5-5: Experimental and numerical results using the calibrated Yasuda-Carreau parameters.

5.2 Temperature Related Effects

A zoom of the zone of maximum forces of the experimental force-velocity curves will show that force peaks tend to decrease with the number of cycles, as shown in Figure 5-6 for Test 2-1.

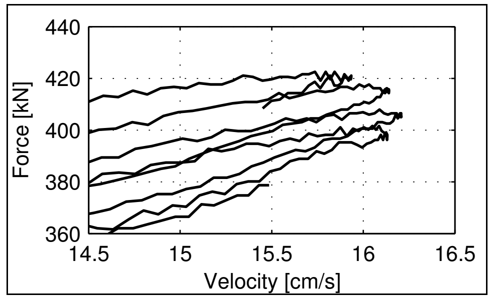

Figure 5-6: Zoom of the maximum force zone for Test 2-1.

To capture this effect, multiphysics models with mesh deformation were employed. Since the amount of dissipated energy (hence, heat production) does not vary importantly if fluid compressibility is included, incompressibility was assumed to decrease computing time. The piston displacement prescribed in the model was the measured dynamic displacement of the actuator, and the calibrated Yasuda-Carreau parameters (Table 5-1) were used. The fluid´s initial temperature can be seen in Table 4-1.

Shown in Figure 5-7 is an example of the resulting temperature field within the fluid and solid domains at the end of a test, specifically t =48.95 s for Test 3-1. The temperature rise concentrates in the length covered by the movement of the piston ($\pm$12.4 cm for this test) and temperature barely rises in the zone near the seals due to the fluid's low thermal conductivity. This is positive for the longevity of the seals which have upper limits for working temperature.

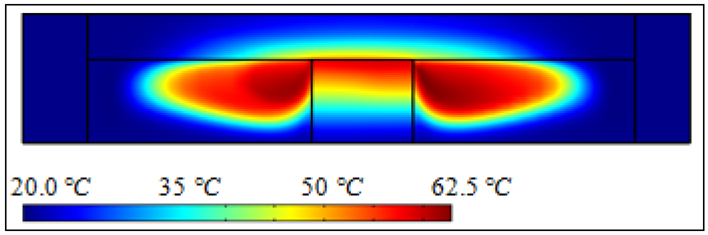

Figure 5-7: Temperature field at the end of Test 3-1.

This rise in temperature causes a decrease in viscosity, affecting the damper's maximum force. Figure 5-8 presents the numerically predicted and experimentally obtained peak forces and their variation with the number of complete full amplitude cycles for Tests 1-1, 2-1 and 3-1. Although the model is successful in capturing the force reduction effect, it tends to overestimate it. Between the first and fifth complete cycle, experimental results show for the three tests a peak force reduction of approximately 1.3%, 6.3% and 8.4%, respectively. Instead, numerical results show larger reductions of about 3.9%, 10.8% and 10.0%, respectively. In the case of Test 3-1, the peak force tends to stabilize after the fifth cycle in the experimental measurements, as opposed to the numerical model.

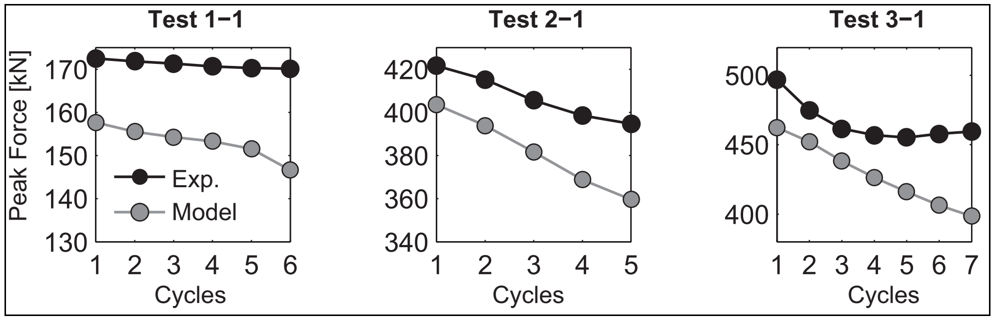

Figure 5-8: Peak forces vs. number of completed full amplitude cycles for Tests 1-1, 2-1 and 3-1.

Although speculative, the model overestimation may be explained by underestimating the heat flow out of the fluid domain due to the adiabatic rod boundary condition, or the convection boundary condition at the interface between cylinder and surrounding ambient air. Another potential error involves the modeling of fluid viscosity, specifically the shift factor that multiplies κ in Eq. (2.11); this model was derived by Swallow (2002) for fluids with very low n-value and may not be as accurate when n is greater, as is the case of SF1 and SF30. The merging beyond certain shear rate of curves corresponding to different temperatures is greater as n becomes lower. A greater merging of the curves in Figure 2-2 and Figure 2-3 would produce less viscosity decrease and, thus, less output force decrease with temperature. Moreover, Eq. (2.11) considers viscosity to vary only with $\dot{\gamma}$ and T; however, viscosity in liquids tends to increase with pressure. The model also neglects dimensional changes that occur due to thermal expansion of the steel components.

The multiphysics model may also be used to estimate the increase in pressure due to fluid thermal expansion, very relevant for design purposes. Pressure changes due to temperature variations may be roughly estimated as:

$$\Delta p = \zeta / \beta \cdot \Delta T \tag{5.1}$$

where $\zeta = 1.2 \cdot 10^{-3}$ $1/K$ is the coefficient of thermal expansion of the fluid. Temperature in the fluid domain was averaged at different time instants in the multiphysics model and the corresponding pressure increase, calculated using Eq. (5.1) was plotted in Figure 5-9. This figure also includes the average of the pressures measured within both chambers at discrete times during Tests 2-1 and 3-1, showing good agreement.

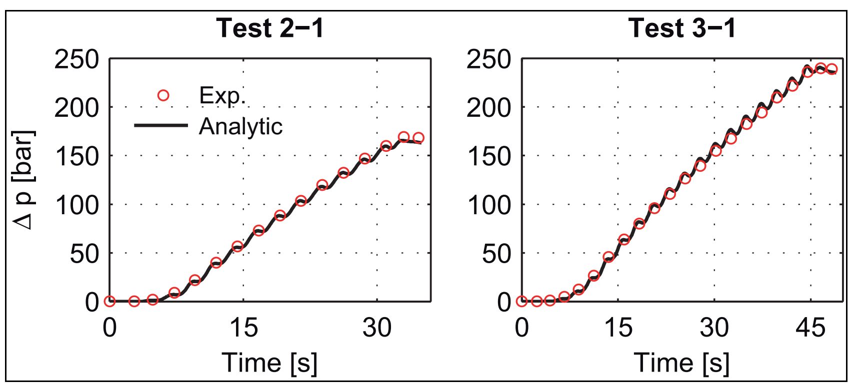

Figure 5-9: Pressure at both chambers averaged at discrete times during Test 2-1 and 3-1 compared to the analytical estimate substituting the average temperature at the fluid domain during the multiphysics simulation in Eq. (5.1)

6. NON-LINEAR MAXWELL MACROSCOPIC MODEL

The classic damper macroscopic model, Eq.(1.1), assumes a purely viscous behavior: force depends exclusively on the instantaneous velocity (zero memory), which implies no hysteresis. Based on Figure 5-2 through Figure 5-5, this type of model fits the lower frequency tests adequately. However, as frequencies increase, tests reveal hysteresis in the force-velocity relationship, for both the numerical and experimental results, implying that behavior is viscoelastic rather than purely viscous. Thus, a restoring force or stiffness component must be involved. Previous investigations have reported that some damper designs may lead to considerable restoring forces. For example, a device using a single instead of double ended rod will need an extra accumulator chamber to compensate for volume variations inside the cylinder as the piston strokes. Symans and Constantinou (1998) attributed the appearance of restoring forces when the damper was excited at frequencies beyond a cutoff value to the functioning of this accumulator. Then again, restoring forces have also been observed (Li et. al, 2006) at high frequency excitation in dampers that use double ended rods.

Before proposing a macroscopic model that is able to capture this phenomenon, the origin of these restoring forces in our prototype will be discussed. Shown in Figure 6-1 is the numerical result for Test 2-1 with an imposed flow model with and without compressibility. In the incompressible case, behavior is purely viscous, while in the compressible case, a restoring force appears due to the fluid's bulk modulus. An additional curve in Figure 6-1 shows the result of a simulation sharing the same maximum velocity, but a frequency two times greater, i.e., 2 *Hz*, demonstrating that the model is indeed able to capture the frequency dependency of this phenomenon. In contrast, if incompressibility is assumed, damper force depends only on velocity, regardless of the A and f combination that yields V. In the three cases, the achieved maximum force is virtually the same. This is true for the range of frequencies studied in this thesis but, in general, for a given velocity the maximum force will tend to decrease as frequency increases in the compressible case. If Eq.(1.1) is fitted to the results in Figure 6-1, both compressible results yield α = 0.87 and the incompressible result α = 0.88. These values are essentially the same, indicating that despite the appearance of hysteresis, the underlying non-linear backbone shape is preserved.

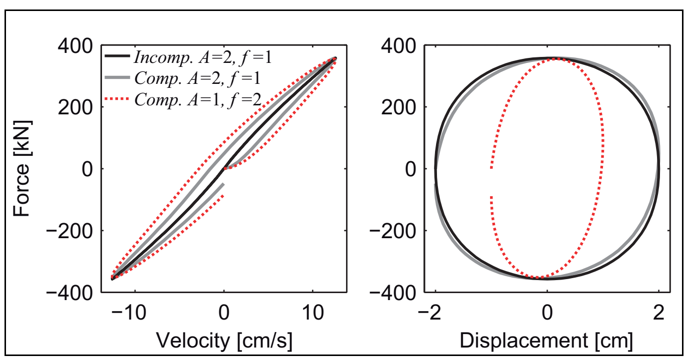

Figure 6-1: Numerical result for Test 2-2 with and without considering compressibility and an additional result considering twice the frequency and half the amplitude.

Previous investigations, such as Makris and Constantinou (1991), Makris and Constantinou (1993), and Lewandowski and Chorazyczewski (2010), have proposed modeling viscoelastic fluid dampers with Maxwell-type macroscopic models using derivatives of fractional or complex order. In this article, a simple approach is proposed based on the same idea of a dashpot (non-linear, with $F \propto V^{\alpha}$) and a spring connected in series, as can be seen in Figure 6-2. Solving for F in this case yields:

$$F = C\left|\dot{y} - \dot{F}/K\right|^{\alpha} \operatorname{sgn}\left(\dot{y} - \dot{F}/K\right) \tag{7.1}$$

As $K \rightarrow \infty$, i.e. an incompressible fluid, Eq. (7.1) reduces to (1.1). The appearance of $\dot{F}$ accounts for the input frequency dependence, since $\dot{F}$ will be an increasing function of ω.

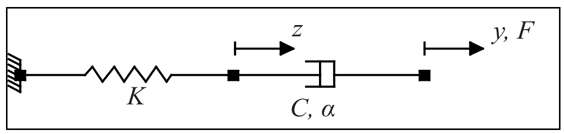

Figure 6-2: Non-linear Maxwell model consisting of a linear spring and non-linear dashpot connected in series.

For easy integration of Eq. (7.1) using a numerical scheme such as Runge-Kutta, $\dot{F}$ may be solved in terms of F by separating this equation in two cases:

$$F = \begin{cases} C\left(\dot{y} - \dot{F}/K\right)^{\alpha} & \text{if} \quad \left(\dot{y} - \dot{F}/K\right) > 0 \\ -C\left(\dot{F}/K - \dot{y}\right)^{\alpha} & \text{if} \quad \left(\dot{y} - \dot{F}/K\right) < 0 \end{cases} \tag{7.2}$$

If $\left(\dot{y} - \dot{F}/K\right) > 0$:

$$F = C\left(\dot{y} - \dot{F}/K\right)^{\alpha}$$
$$\left(F/C\right)^{1/\alpha} = \dot{y} - \dot{F}/K$$
$$\dot{F} = K \cdot \dot{y} - K \cdot \left(F/C\right)^{1/\alpha}$$

If $\left(\dot{y} - \dot{F}/K\right) < 0$:

$$F = -C\left(\dot{F}/K - \dot{y}\right)^{\alpha}$$
$$\left(-F/C\right)^{1/\alpha} = \dot{F}/K - \dot{y}$$
$$\dot{F} = K \cdot \dot{y} + K \cdot \left(-F/C\right)^{1/\alpha}$$

Hence,

$$\dot{F} = \begin{cases} K\dot{y} - K\left(F/C\right)^{1/\alpha} & if \quad \left(\dot{y} - \dot{F}/K\right) > 0 \\ K\dot{y} + K\left(-F/C\right)^{1/\alpha} & if \quad \left(\dot{y} - \dot{F}/K\right) < 0 \end{cases} \tag{7.3}$$

The proposed macroscopic model, in lieu of Eq. (1.1), is able to represent hysteretic effects as frequency increases, thus adapting very accurately to the experimental force-velocity results. Shown in Figure 6-3 is Eq. (7.1) fitted to these results. Instead of two parameters as in Eq. (1.1), three parameters are needed to characterize the curves: *C, α* and *K*.

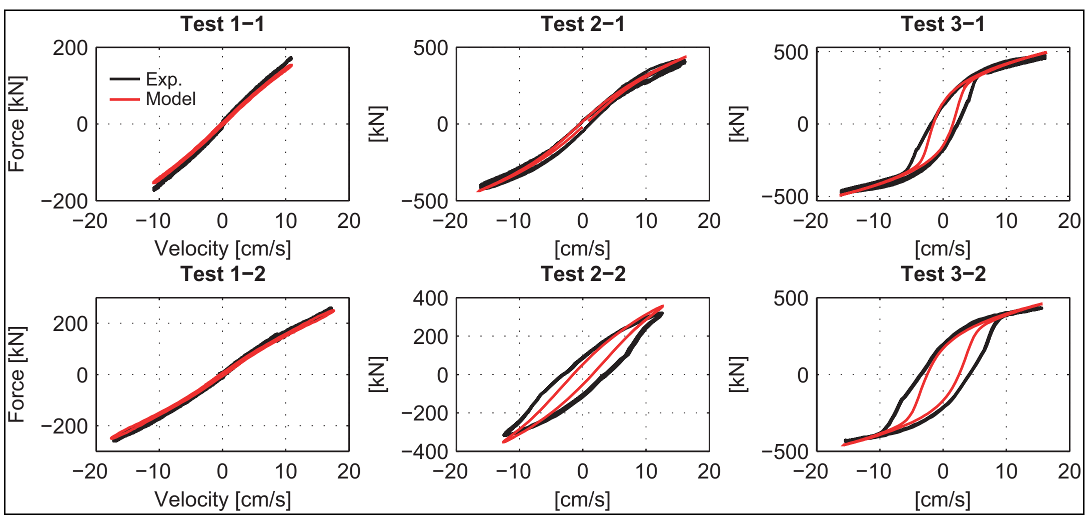

Figure 6-3: Non linear Maxwell model, Eq. (7.1), fitted to the experimental results; corresponding numerical values of *C*, *α* and *K* may be seen in Table 6-1.

Table 6-1 summarizes the best fit values of *C, α* and *K* corresponding to the experimental results and to the numerical results considering the originally presented Yasuda-Carreau parameter values (Table 2-1) and the calibrated ones (Table 5-1). Table 6-1 corroborates what was graphically evident in Figure 5-2 through Figure 5-4: the simulations carried out with the original Yasuda-Carreau parameters overestimated the experimental α-values. Simulations with the calibrated parameters, on the other hand, reproduce the experimental maximum force and α-values with much better accuracy, as can be graphically seen in Figure 5-5. Although an important dispersion may be observed in *K*, the sensitivity of the proposed model to this parameter is small. Thus, for the range of frequencies considered in this article, a representative value of *K* adopted after considering several tests may be used to characterize the damper without a significant loss of accuracy.

Table 6-1: Results of fitting Eq. (7.1) to the experimental and numerical results considering the originally presented Yasuda-Carreau parameters (Table 2-1) and the calibrated values (Table 5-1).

	Test	1-1	1-2	2-1	2-2	3-1	3-2
Exp.	F_{max} [kN]	172	189	424	326	501	441
	C [$kN/(m/s)^{\alpha}$]	1143	1159	1545	1640	906	891
	α	**0.86**	**0.86**	**0.73**	**0.77**	**0.36**	**0.37**
	K [kN/m]	89813	81326	89950	78821	105210	90781
Orig. YC	F_{max} [kN]	142	163	448	358	665	654
	C [$kN/(m/s)^{\alpha}$]	1139	1174	2165	2217	1496	1527
	α	0.94	0.95	0.86	0.87	0.44	0.45
	K [kN/m]	100070	190950	124560	225270	201460	212310
Calib. YC	F_{max} [kN]	142	160	409	344	475	475
	C [$kN/(m/s)^{\alpha}$]	953	958	1585	1639	928	952
	α	**0.86**	**0.86**	**0.74**	**0.75**	**0.37**	**0.38**
	K [kN/m]	112610	183150	112270	224080	200750	199830

7. CONCLUSIONS

The mathematical models presented herein have proven sufficiently accurate to be integrated as an effective tool in the design process of viscous dampers, both for thermal evaluation, and for estimating their force-velocity constitutive relationship. The greatest observed discrepancies between numerical and experimental results are in the vicinity of 10-15%.

The gross tendencies of different fluid passage configurations were approximated by analytically solving fluid mechanics limit cases, identifying that aspects such as passage length and viscosity advocate for viscous flow and aspects such as density, piston radius and velocity advocate for inertial flow. Furthermore, velocity exponent α correlates well with a parameter that estimates the shear deformation rate in the case of the annular orifice, and with the ratio of inertial to viscous effects in the case of cylindrical orifices. These correlations are valid for any damper size, allowing the design of any desired damper capacity. It was found that annular orifices are better suited to produce low exponent outputs ($\alpha < 1$), while cylindrical orifices offer more flexibility if exponents greater or close to one are sought by using a lower viscosity fluid (e.g., SF1).

The constitutive behavior of the fluid turned out to be essential to the damper's behavior. Highly viscous silicone oils ($\geq 1\ Pa{\cdot}s$) tend to low exponent outputs due to their rapid shear thinning, while lower viscosity silicone oils tend to higher exponents due to their smaller shear thinning. Quantitatively, as shear rate increases and viscous effects prevail, α will tend to the value of n from the Yasuda-Carreau equation. Since the silicone oils used in this research could not be tested thoroughly, the uncertain rheological data adopted led to discrepancies, for example, α being overestimated. This was corrected by calibrating the rheological parameters according to the experimental force-velocity results. It is clear that for precise predictive modeling, an accurate rheological characterization of the fluid is required.

Although rather complex damper models were developed, including aspects such as mesh deformation to account for piston movement, model simplifications led to successful results. In this regard, the imposed flow approach (allowing a stationary domain) and the independent orifice approach (allowing the combination of different orifices without having to reproduce the complete piston geometry) were exceedingly faster, yet sufficiently accurate to be used as a design tool and for parametric analyses.

The multiphysics models were found to overestimate the decrease in output force caused by fluid heating, however, they still provide a sufficiently accurate estimation of this phenomenon. Furthermore, it was shown how to estimate the pressure build up due to thermal expansion of the fluid, an essential aspect for design.

Both the numerical and experimental results showed that the classic purely viscous macroscopic model, Eq. (1.1), was accurate only at low frequencies, where damper restoring forces were negligible. At higher frequencies, significant viscoelastic behavior, attributed to the fluid's bulk modulus, becomes relevant. An extension of Eq. (1.1) was proposed by incorporating stiffness to a macroscopic model that can be used in structural analyses. The proposed model, consisting of a non-linear dashpot and a linear spring in series, was able to represent the experimental and numerical results extremely accurately.

Proposed future work includes the study of a much broader variety of fluids, increasing the ability to generate different α exponents and optimization in terms of manufacturing cost. Parametric analyses concerning thermal performance, for instance analyzing what geometric proportions or configurations are more favorable to reduce the output force decrease, could also be interesting alternatives. The multiphysics model can also be enhanced to include the influence of pressure on viscosity. Finally, a further enhancement would be a deeper study of variable area orifices and, eventually, make them controllable, transforming the viscous damper into a semi-active device.

BIBLIOGRAPHY

Ansys Inc. (2009). *ANSYS 12.1 user's manual*, Canonsburg, Pa, United States.

Ansys Inc. (2009). *ANSYS CFX-Pre User's Guide Release 12.1,* Canonsburg, PA, United States.

Cameron, B., and Makris, N. (2007). Viscous heating of fluid dampers under small and large amplitude motions: experimental studies and parametric modeling. *Journal of Engineering Mechanics,* 133(5), 566-577.

Cameron, B., and Makris, N. (2005). Viscous heating of fluid dampers under wind and seismic loading: experimental studies, mathematical modeling and design formulae. *Earthquake Engineering Research Center Rep. No. EERC 2006-01,* College of Engineering, University of California, Berkeley.

Clasen, C., Kavehpour, P., McKinley, G., (2010). Bridging tribology and Microrheology of thin films, *Applied Rheology*, 20(4), 45049-(1-13).

Clearco Products, *Compressibility of Silicone Fluids*, Bensalem, PA, United States. http://www.clearcoproducts.com/silicones_library.html

Comsol AB (2008). *COMSOL Multiphysics 3.5a User's Guide*, Stockholm, Sweden.

Constantinou, M. C., and Symans, M. D. (1992). Experimental and analytical investigation of seismic response of structures with supplemental fluid viscous dampers. *National Center for Earthquake Engineering Research Rep. No. NCEER-92-0032*, State Univ. of New York at Buffalo, Buffalo, N.Y..

Currie, C.C., and Smith, B.F. (1950). Flow characteristics of organopolysiloxane fluids and greases. *Ind. Eng. Chem.,* 42(12), 2457-2462.

Gelest, Inc. *Silicone Fluids: Stable, Inert Media*, Morrisville, PA, United States. (2004)

Ghannam, M., and Esmail, N. (1998). Rheological Properties of Poly(dimethylsiloxane). *Ind. Eng. Chem. Res.,* 37, 1335-1340.

Hou, C.Y. (2008). Fluid dynamics and behavior of nonlinear viscous fluid dampers. *Journal of Structural Engineering*, 134(1), 56-63.

Hou, C.Y., Hsu, D.S., Lee, Y.F., Chen, H. Y., and Lee, J.D. (2007). Shear thinning effects in annular orifice viscous fluid dampers. *Journal of the Chinese Institute of Engineers*, 30(2), 275-287.

Jiuhong, J., Jianye, D., Yu, W., and Hongxing, H. (2008). Design method for fluid viscous dampers. *Archive of Applied Mechanics*, 78, 737-746.

Lee, C.L., Pomanteer, K.E., and King, E. G. (1970). Flow behavior of narrow distribution polydimethylsiloxane. *J. Polym. Sci.,* Part A-2, 8, 1909-1916.

Lee, D., and Taylor, D.P. (2001). Viscous damper development and future trends. *The Structural Design of Tall Buildings*, 10, 311-320.

Lewandowski, R., and Chorazyczewski, B. (2010). Identification of the parameters of the Kelvin-Voigt and the Maxwell fractional models, used to modeling viscoelastic dampers. *Computers and Structures,* 88 (2010), 1-17.

Li, Z.Q., Xu, Y.L., and Zhou, L.M. (2006). Adjustable fluid damper with SMA actuators. *Smart Materials and Structures*, 15, 1483-1492.

Makris, N., and Constantinou, M.C. (1991). Fractional-derivative Maxwell model for viscous dampers. *Journal of Structural Engineering*, 117(9), 2708-2724.

Soong, T.T., and Dargush, G. (1997). *Passive Energy Dissipation Systems in Structural Engineering*. John Wiley & Sons Ltd., Chichester, United Kingdom.

Swallow, Frank E. (2002). Viscosity of Polydimethylsiloxane Gum: Shear and Temperature Dependence from Dynamic and Capillary Rheometry. *Journal of Applied Polymer Science,* Vol. 84, 2533-2540.

Symans, M.D., and Constantinou, M.C. (1997). Experimental testing and analytical modeling of semi-active fluid dampers for seismic protection. *Journal of Intelligent Material Systems and Structures*, 8(8), 644-657.

Symans, M.D., and Constantinou, M.C. (1998). Passive fluid viscous damping systems for seismic energy dissipation. *ISET Journal of Earthquake Technology*, 35(4), 185-206.

Valdebenito, G., Aparicio, A., Alvarez, J., and López-Almansa, F. (2010). Passive Seismic Energy Dissipation Applying Fluid Viscous Damping Technology: A State of the Art Review. *Congreso Chileno de Sismología e Ingeniería Antisísmica*. Santiago, Chile.

Wolfe, R.W., Yun, H.B., Masri, S., Tasbihgoo, F., and Benzoni, G. (2008). Fidelity of reduced-order models for large-scale nonlinear orifice viscous dampers. *Structural Control and Health Monitoring,* Wiley Interscience DOI: 10.1002/stc.256.

APPENDICES

APPENDIX A: RHEOLOGY TESTING OF SF30 SILICONE FLUID

Viscosity analysis of the SF30 silicone fluid ($\mu_0 = 30\left[Pa \cdot s\right]$ at 20°C) was hired at TA Professional Services (http://www.tainstruments.com). The experiments were performed on a TA Instruments AR-2000ex Rheometer with a Peltier plate for temperature control. A schematic representation of this instrument can be seen in Figure A-1.

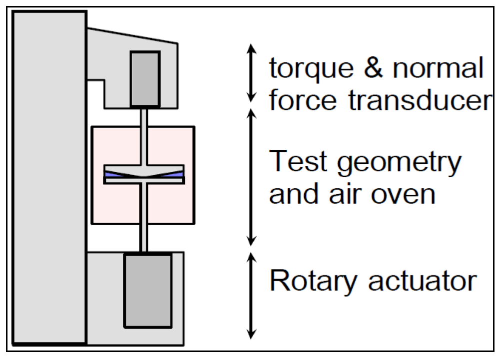

Figure A-1: Rheometer used to measure viscosity-shear rate relationships for SF30 silicone fluid at different temperatures.

In a rotational rheometer the sample is sheared between two plates or a cone and plate geometry and the viscosity is calculated as the ratio of the applied stress and the applied deformation rate (rotation speed). For the series of tests presented here, parallel plates were used, specifically a 25 *mm* diameter for the upper geometry and a Peltier plate for the lower geometry.

The original test procedure consisted in a steady state flow sweep, stepping shear rates from 1 [1/*s*] to a maximum of 10000[1/*s*]. Shear rates were to be equilibrated at discrete values for 10 seconds and viscosity collected and averaged for 5 seconds. This process was to be carried out for the following temperatures: 10°C, 20°C, 30°C, 40°C, 50°C, 60°C, 70°C, 80°C, 90°C, and 100°C.

Unfortunately, the projected maximum shear rate of 10000 1/s was not reached, due to the flow behavior exhibiting a distinct “edge failure” of the sample at different critical shear rates depending on the temperature. Viscosity data for higher shear rates was attempted using various cone diameters and angles and various parallel plates, and the conclusion was the same for all geometries. For each temperature, the sampled failed at relatively low critical shear rate levels regardless of the geometry used. Figure A-2 shows the specific results for 20°C to illustrate the described phenomenon. Figure A-3 overlays the plots corresponding to all tested temperatures.

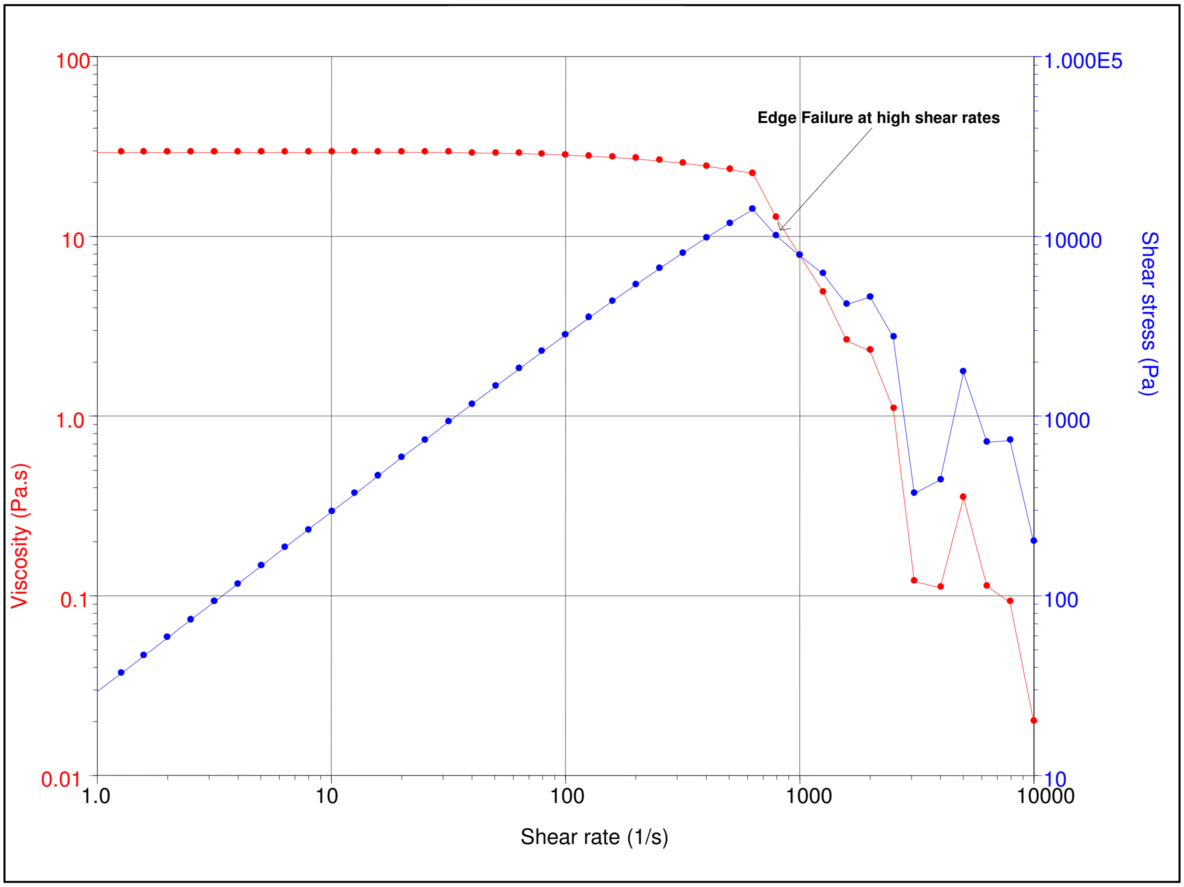

Figure A-2: Viscosity-shear rate relationship at 20°C obtained with a steady state flow sweep. In the Newtonian flow region the average viscosity is 29.3 $Pa{\cdot}s$. At about 800 [1/s] a distinct edge failure with flow instability is recognizable.

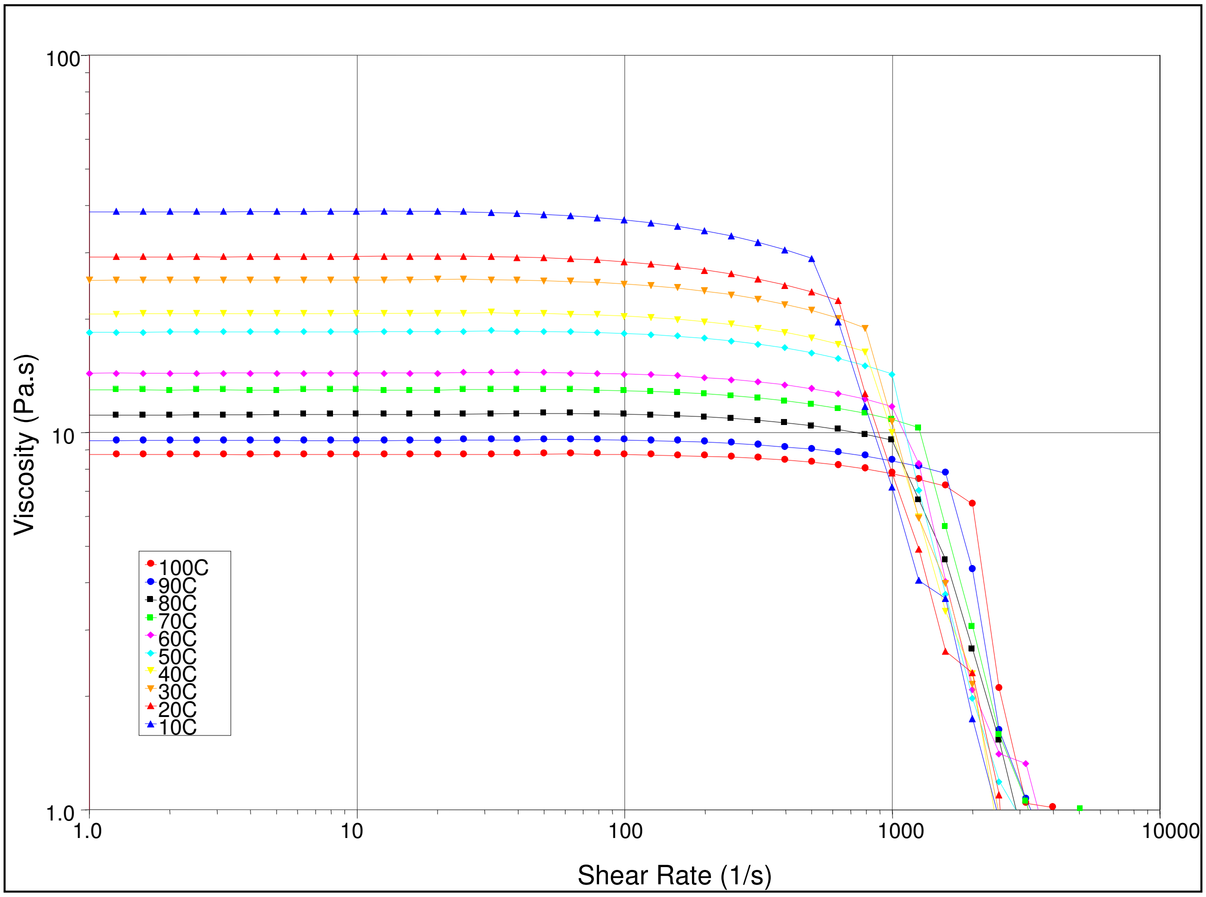

Figure A-3: Overlay of viscosity-shear rate plots for the different tested temperatures.

The data gathered from these tests was used to fit an Arrhenius type equation to model the zero shear rate viscosity (μ_0) dependence on temperature. The general model, Eq. (A.1), was fitted in a least squares sense to the average viscosities in the Newtonian flow regions measured at different temperatures.

$$f(x) = c \cdot \exp(b/x) \tag{A.1}$$

The calculated coefficients, with 95% confidence bounds, were c = 78.97 (52.74, 105.2) and b = 1746 (1646, 1846), as was presented in Table 2-1 in the body of this thesis. The units for c and b are $mPa{\cdot}s$ and K, respectively. Figure A-4 shows the experimental data and the fitted curve.

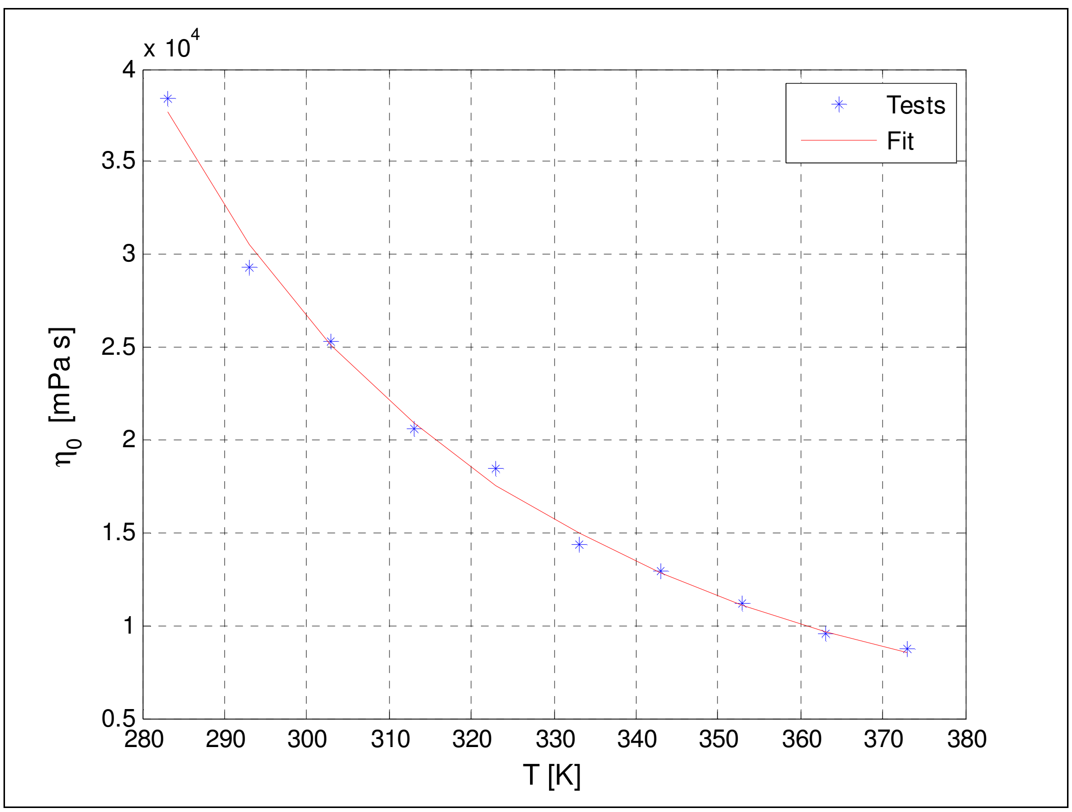

Figure A-4: Measured zero shear rate viscosities at different temperatures and curve fit.

Additionally, a Yasuda-Carreau equation (2.9) was fitted to the reliable test data corresponding to 20°C (μ_0 = 30 $Pa{\cdot}s$), that is, before the edge failure. Since higher shear rates were expected in the damper, it was decided to add an extra point to this data. This point was taken from a manual provided by a manufacturer of polydimethylsiloxane (Gelest Inc. 2004) stating that for a silicone fluid with μ_0 = 30 $Pa{\cdot}s$ at 25°C, a viscosity of 6 $Pa{\cdot}s$ is expected for a shear rate of 10000 1/s.

The general model used for the curve fitting, a Yasuda-Carreau equation, was:

$$f\left(x\right)=29300\cdot\left[1+\left(\kappa x\right)^{a}\right]^{\frac{n-1}{a}} \tag{A.2}$$

The calculated coefficients, with 95% confidence bounds, were n = 0.407 (0.3671, 0.447), a = 1.325 (1.244, 1.406) and κ = 0.001405 [s] (0.001193, 0.001617), as was presented in Table 2-1. Figure A-5 shows the experimental data and the fitted curve and Figure A-6 compares this result with a viscosity-shear rate curve for the equivalent fluid presented in the mentioned manual.

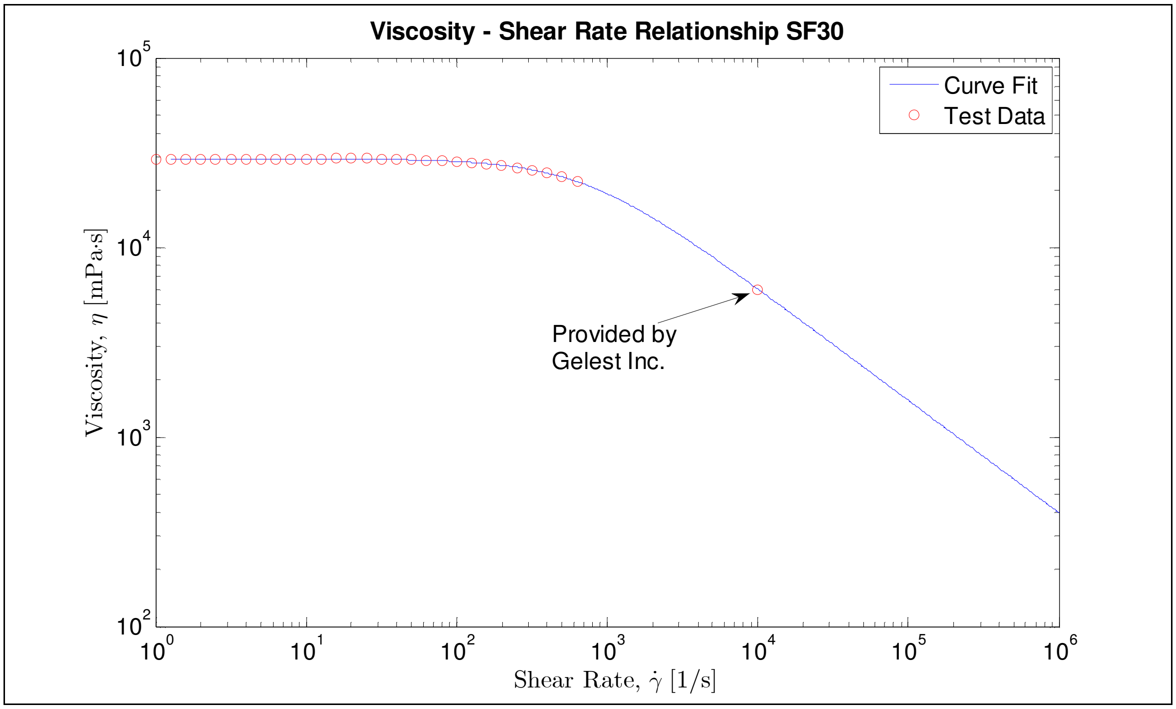

Figure A-5: Curve fitted to the experimental viscosity-shear rate data measured at 20°C and the extra point provided in the Gelest manual (Gelest Inc. 2004).

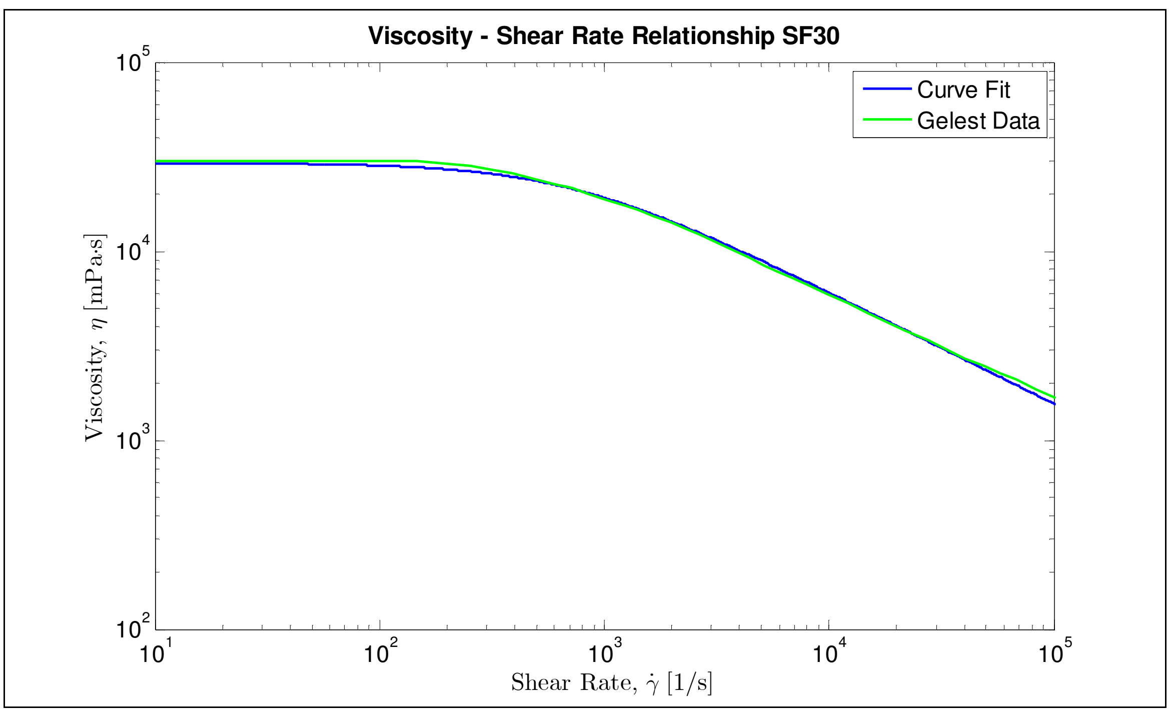

Figure A-6: Comparison of the fitted viscosity-shear rate relationship with an analogous curve presented in the Gelest manual (Gelest Inc. 2004).

APPENDIX B: LIMIT CASES FOR VISCOUS AND INERTIAL FLOW

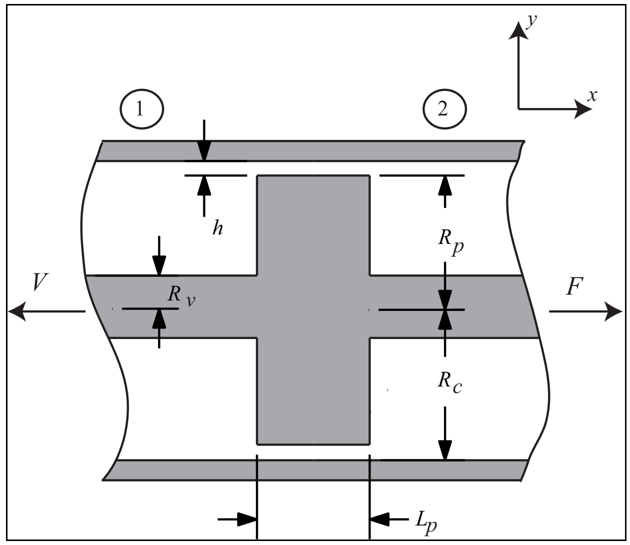

Figure B-1: Annular orifice geometry.

Figure B-1 displays the geometry corresponding to the annular orifice case. As the piston strokes with velocity *V*, fluid flows from chamber 1 to chamber 2. When $h << R_p$, flow through the annular region can be idealized as flow between parallel plates. If the fluid is considered incompressible, the momentum equation (Eq. (2.2)) reduces to:

$$\rho\left(\frac{\partial u}{\partial t}+u\frac{\partial u}{\partial x}\right)=-\frac{\partial p}{\partial x}+\frac{\partial \tau}{\partial y} \tag{B.1}$$

where *u* denotes velocity in the *x* direction. There are two limit cases for Eq. (B.1): dominance of viscous effects and dominance of inertial effects. For the viscous dominance case, convective acceleration can be neglected, and so can the transient acceleration term for low frequency excitation. Therefore:

$$\frac{\partial p}{\partial x}=\frac{\partial \tau}{\partial y} \tag{B.2}$$

On the other hand, for stationary unidirectional flow, $\partial p / \partial x = -\Delta p / L_p$, where $\Delta p = p_1 - p_2$. Assuming a symmetric velocity profile in the gap, i.e., $\tau(h/2) = 0$, and integrating yields:

$$\tau = \frac{\Delta p}{L_p}\left(\frac{h}{2} - y\right) \tag{B.3}$$

If the fluid is considered Newtonian, $\tau(y) = \mu_0 \cdot \partial u / \partial y$ and applying the no slip condition $u(h) = 0$, a further integration of Eq. (B.3) yields:

$$u(y) = \frac{\Delta p}{2\mu_0 L_p}\left(hy - y^2\right) \tag{B.4}$$

By combining Eq. (B.4) with the continuity principle, Eq. (B.5), Δp may be solved for.

$$V\pi\left(R_c^{\,2} - R_v^{\,2}\right) = 2\pi R_p \int_0^h u(y)\,dy \tag{B.5}$$

Then, using the $F = A_p \cdot \Delta p$ approximation and assuming $R_p \approx R_c$, the damper output force $F = \left(R_p^{\,2} - R_v^{\,2}\right)^2 6\pi\mu_0 L_p / \left(R_p h^3\right) \cdot V$ is obtained, that is, Eq. (3.1) in the body of this thesis.

If inertial effects dominate, the fluid can be idealized as inviscid, i.e., $\partial\tau / \partial y = 0$. Neglecting transient acceleration, Eq. (B.1) reduces further to:

$$\rho u \frac{\partial u}{\partial x} = -\frac{\partial p}{\partial x} \tag{B.6}$$

Assuming that velocity is equal to zero somewhere near the entrance of the gap and that fluid particles are then accelerated to velocity u_2, integrating the previous equation yields:

$$-\left(p_2 - p_1\right) = \Delta p = \frac{\rho u_2^2}{2} \tag{B.7}$$

Combining this with continuity:

$$V\pi\left(R_c^{\ 2} - R_v^{\ 2}\right) = 2\pi R_p h u_2 \tag{B.8}$$

Finally, assuming $R_p \approx R_c$, the relation between output force and velocity can be approximated by $F = A_p \cdot \Delta p$, resulting in $F = \rho\pi\left(R_p^{\ 2} - R_v^{\ 2}\right)^3 / 8R_p^{\ 2}h^2 \cdot V^2$, as expressed in Eq. (3.7).

The same analysis was done for the piston with cylindrical orifices, whose geometry can be seen in Figure B-2. The analysis focuses on the flow inside the orifices and assumes that pressure is uniform pressure in chambers 1 and 2.

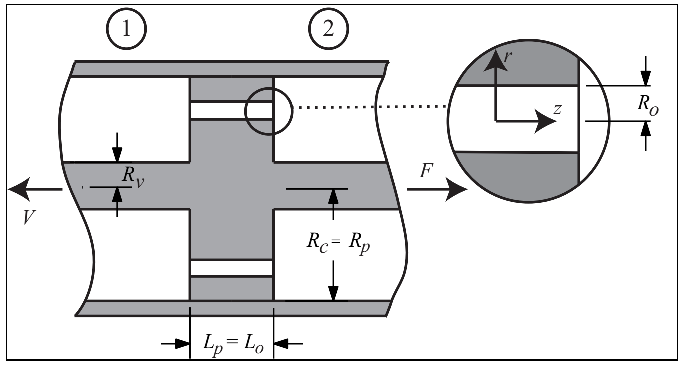

Figure B-2: Geometry for the piston with cylindrical orifices.

For an incompressible, Newtonian fluid, the momentum equation (Eq. (2.2)) inside the orifices in cylindrical coordinates reduces to:

$$\rho\left(\frac{\partial w}{dt}+w\frac{\partial w}{\partial z}\right)=-\frac{\partial p}{\partial z}+\mu_0\left[\frac{1}{r}\frac{\partial}{\partial r}\left(r\frac{\partial w}{\partial r}\right)\right] \tag{B.9}$$

where w denotes the velocity in the z direction and r denotes the radial direction inside the orifice. If viscous effects dominate, convective acceleration can be neglected, and so can the transient term for low frequencies. Eq. (B.9) becomes:

$$\frac{1}{\mu_0}\frac{\partial p}{\partial z}=\frac{1}{r}\frac{\partial}{\partial r}\left(r\frac{\partial w}{\partial r}\right) \tag{B.10}$$

Integrating this equation twice (assuming that velocity at the cylinder walls is zero and that velocity at $r = 0$ must be finite) and using that for stationary unidirectional flow, $\partial p / \partial z = -\Delta p / L_p$, the velocity profile inside the orifice is:

$$w(r)=\frac{1}{4\mu_0}\frac{\Delta p}{L_p}\left(R_o^{\,2}-r^2\right) \tag{B.11}$$

where R_o is the orifice radius. Applying continuity and integrating (B.11) yields:

$$V\pi\left(R_p{}^2 - R_v{}^2\right) = N\frac{\pi R_o{}^4}{8\mu_0}\frac{\Delta p}{L_p} \tag{B.12}$$

Assuming that $F \approx A_p \Delta p$, the output force for the damper is therefore $F = 8\pi\mu_0 L_p\left(R_p{}^2 - R_v{}^2\right)^2 / NR_o{}^4 \cdot V$, as expressed in Eq. (3.6).

If inertia effects dominate, the fluid can be idealized as inviscid. Neglecting transient acceleration, Eq. (B.9) reduces to:

$$\rho w\frac{\partial w}{\partial z} = -\frac{\partial p}{\partial z} \tag{B.13}$$

Assuming a zero velocity near the entrance of the orifice and that the fluid is accelerated to velocity w_2, integrating the previous equations results in:

$$-\left(p_2 - p_1\right) = \Delta p = \frac{\rho w_2^2}{2} \tag{B.14}$$

In this case, continuity can be expressed as $\pi\left(R_p{}^2 - R_v{}^2\right)V = N\pi R^2 w_2$. Substituting in Eq. (B.14) yields $F = \rho\pi\left(R_p{}^2 - R_v{}^2\right)^3 / 2N^2 R_o{}^4 \cdot V^2$, as expressed in (3.7).

APPENDIX C: PARAMETRIC ANALYSES

Annular Orifice Configuration

The geometric dimensions and corresponding force-velocity curves of the models solved to generate Figure 3-2 are listed next. The same geometries were used for both the SF1 fluid (Figure 3-2 (a)) and SF30 fluid (Figure 3-2 (b)).

$A = 3.2[cm] \quad f = 0.5[Hz]$

	h (mm)	R_p (cm)	R_v (cm)	L_p (cm)	$\dot{\gamma}_{ave}$ $(1/s)$
1	5	5	0	20	486.57
2	2	5	0.5	19	2693.22
3	2	8	0.5	18	4209.11
4	2	12	3	15	5857.6
5	1.5	13	4	12	10786.7
6	1.5	13	3	10	11267.9
7	1.3	14	2	15	16626.9
8	1.5	19	5	16	16071.9
9	0.9	12	3	13	28373.7
10	0.9	11	1	19	27527.7
11	1.1	15	2	14	24848.8
12	0.9	18	4	16	42921.9
13	1	20	2	20	40213.4
14	0.8	19	3	18	58705.9
15	0.8	21	4	20	64083.5
16	0.7	20	2.5	15	81359.3
17	0.5	18	2	15	143783
18	0.7	25	2	13	102501
19	0.5	20	4.2	13	154561
20	0.4	19	4	14	229185

$A = 4.0[cm] \quad f = 0.8[Hz]$

	***h* (*mm*)**	***R_p* (*cm*)**	***R_v* (*cm*)**	***L_p* (*cm*)**	$\dot{\gamma}_{ave}$ **(1/*s*)**
1	3	5	0	10	2510.15
2	1.8	5	0.5	19	6598.41
3	1.3	8	0.5	18	19584.8
4	2	12	3	15	11715.2
5	1.5	13	4	10	21573.4
6	1.5	13	4	25	21573.4
7	1.5	13	4	20	21573.4
8	1.5	19	5	16	32143.8
9	0.9	11	3	13	51444.8
10	0.9	11	3.6	19	49657.6
11	1.1	15	2	14	49697.7
12	0.6	12	3.75	16	122295
13	0.84	21	3	18	118197
14	0.8	20	4	20	121644
15	0.7	19	3.75	15	151003
16	0.4	12	2	15	295229
17	0.67	21	2	13	187614
18	0.5	20	5	16	303203
19	0.5	21	4.2	13	325883
20	0.45	20	3.5	14	386786

$A = 4.8[cm] \quad f = 1[Hz]$

	***h* (*mm*)**	***R_p* (*cm*)**	***R_v* (*cm*)**	***L_p* (*cm*)**	$\dot{\gamma}_{ave}$ **(1/*s*)**
1	3	5	0.2	10	3759.86
2	1.8	6	0.4	19	11800.7
3	1.3	7	0.5	18	25793.2
4	2	11	4	15	15002.9
5	1.5	14	3	10	36616.7
6	1.5	12	3	25	30968.6
7	1.5	14	3.5	20	35994.4
8	1	8	4.7	16	32813.3
9	0.9	13	3.2	13	92286.9
10	0.9	9	3.6	19	57644.5
11	1.1	13	2.1	14	64215.4
12	0.95	12	3.75	16	73644.7
13	1.1	20	3.1	18	98404.6
14	0.5	12	4.1	20	258148
15	0.65	20	3.75	15	277352
16	0.5	15	2.2	15	356543
17	0.6	15	2.2	13	247936
18	1.2	37	5	16	153162
19	0.48	19	4.3	13	474458
20	0.44	20	3.7	14	604544

$A = 6.4[cm]$ $f = 1[Hz]$

	***h* (*mm*)**	***R_p* (*cm*)**	***R_v* (*cm*)**	***L_p* (*cm*)**	$\dot{\gamma}_{ave}$ **(1/*s*)**
1	3.2	5	0.2	13	4439.45
2	1.9	6	0.4	21	14167.6
3	1.2	7	0.5	14	40247.8
4	1.9	11	4	11	22119.6
5	2	10	3	15	19108.9
6	1.7	15	3	26	41024.8
7	1.3	14	3.5	21	63703.1
8	1.1	15	4.7	18	91379.4
9	1	13	3.2	14	99831.9
10	0.9	15	3.6	21	142149
11	1.5	23	2.1	13	82602.5
12	0.9	16	3.75	19	151929
13	0.5	11	3.1	17	328988
14	0.78	21	4.1	19	269085
15	0.45	12	3.75	17	433630
16	0.55	18	2.2	15	474341
17	0.69	24	2.2	16	404346
18	0.4	15	5	19	674233
19	0.54	22	4.3	14	586573
20	0.4	19	3.7	19	922852

$A = 4[cm]$ $f = 2[Hz]$

	***h* (*mm*)**	***R_p* (*cm*)**	***R_v* (*cm*)**	***L_p* (*cm*)**	$\dot{\gamma}_{ave}$ **(1/*s*)**
1	3.6	4.5	0.2	13	4064.61
2	2	7	0.4	21	18555.1
3	1.12	8	0.5	14	65671.5
4	1.8	10	4	11	27190.6
5	1.65	13.6	3	15	49001.6
6	1.9	14.9	3	26	40876.3
7	1.2	11.3	3.5	21	73005.1
8	1.1	11	4.7	18	76544.1
9	1	15	3.2	14	145951
10	0.8	12.7	3.6	21	185983
11	1.6	24	2.1	13	94787
12	0.85	15.3	3.75	19	202472
13	0.55	12	3.1	17	375850
14	0.8	23.4	4.1	19	358800
15	0.67	21	3.75	17	458303
16	0.58	17	2.2	15	502998
17	0.45	12	2.2	16	580192
18	0.5	18	5	19	671999
19	0.5	20	4.3	14	771098
20	0.55	24.1	3.7	19	785706

SF1 Annular Orif. Parametric Analysis Results A = 3.2 [cm] f = 0.5 [Hz]

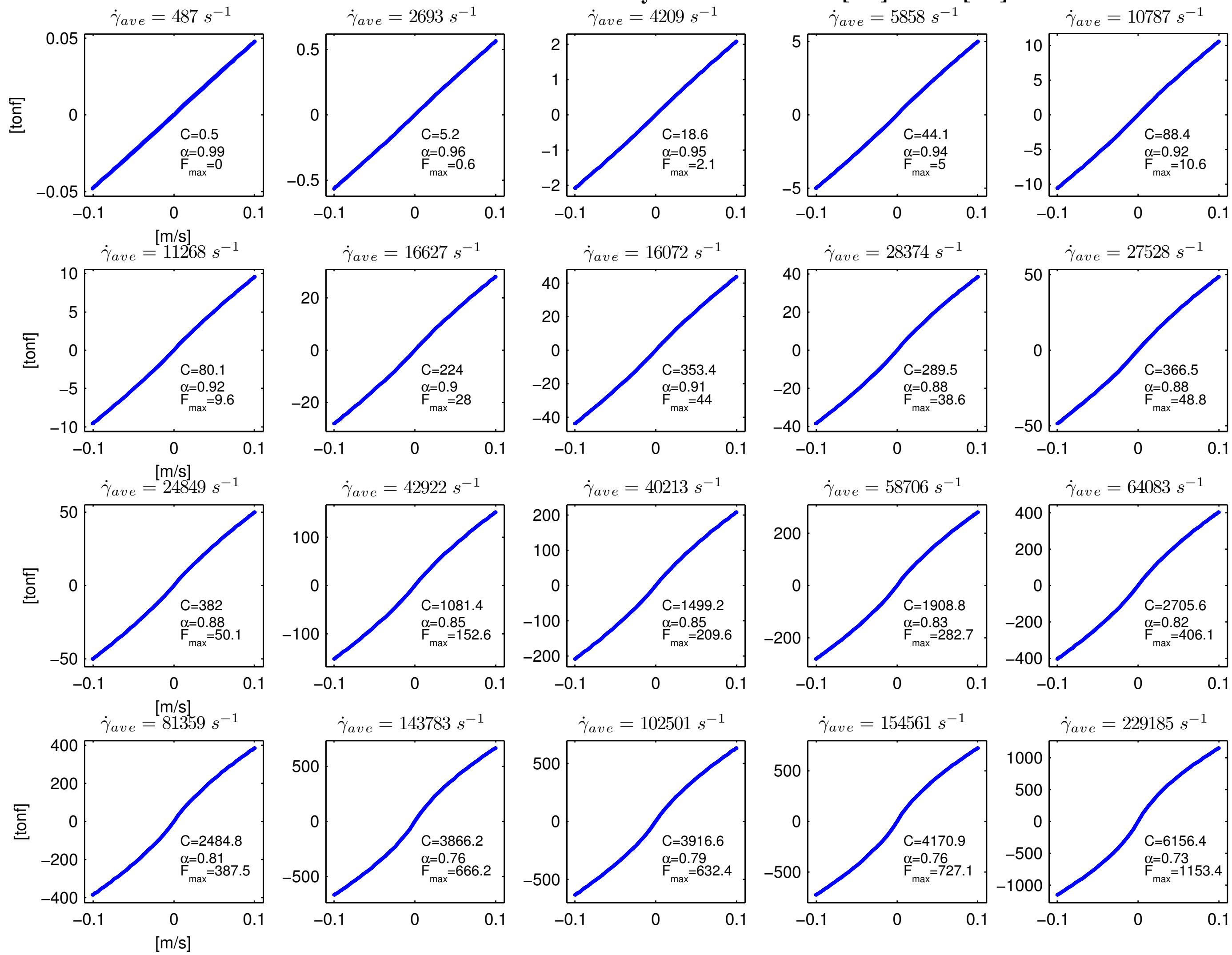

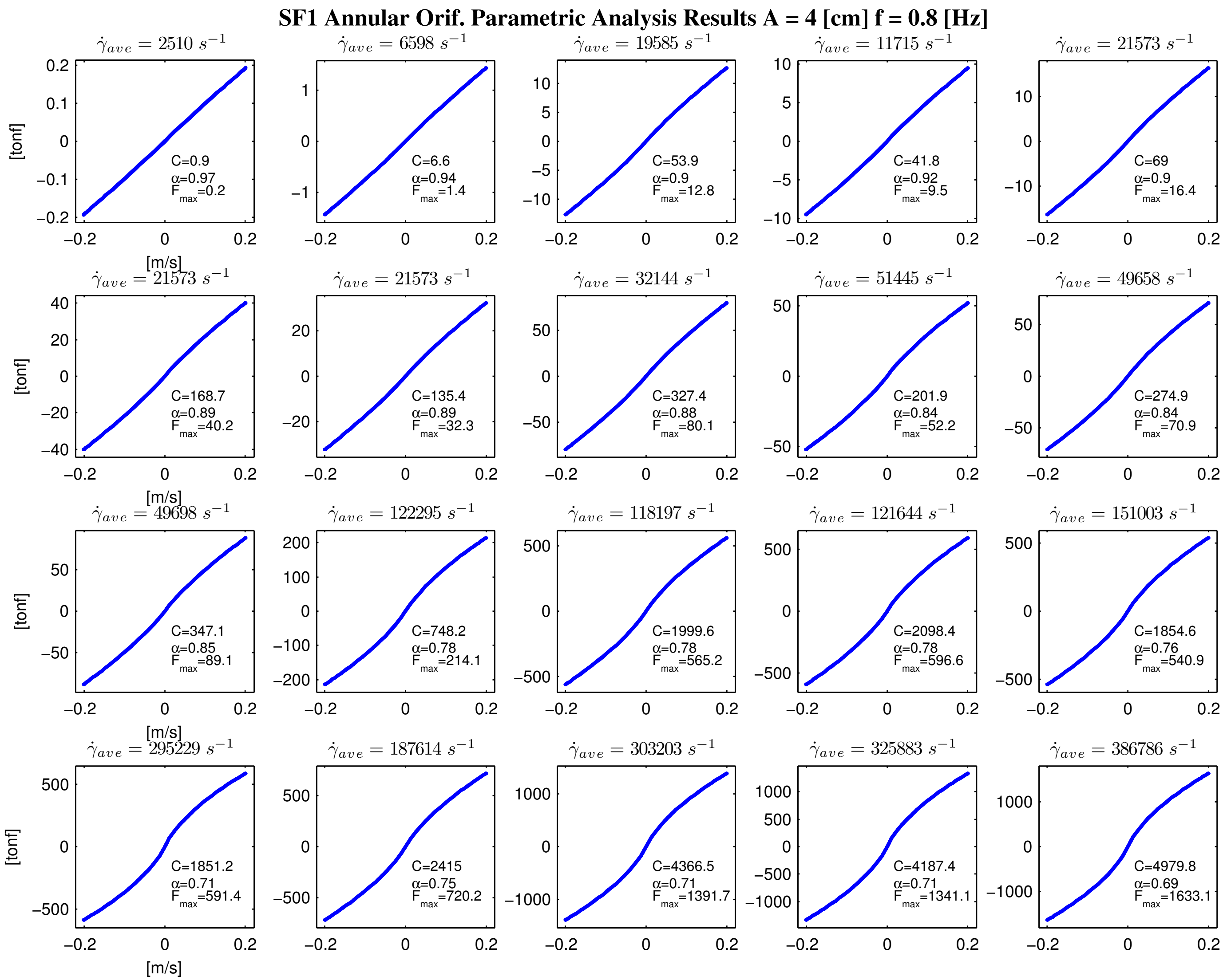
SF1 Annular Orif. Parametric Analysis Results A = 4 [cm] f = 0.8 [Hz]
$\dot{\gamma}_{ave} = 2510\ s^{-1}$
C=0.9
α=0.97
F_{max}=0.2
$\dot{\gamma}_{ave} = 6598\ s^{-1}$
C=6.6
α=0.94
F_{max}=1.4
$\dot{\gamma}_{ave} = 19585\ s^{-1}$
C=53.9
α=0.9
F_{max}=12.8
$\dot{\gamma}_{ave} = 11715\ s^{-1}$
C=41.8
α=0.92
F_{max}=9.5
$\dot{\gamma}_{ave} = 21573\ s^{-1}$
C=69
α=0.9
F_{max}=16.4
$\dot{\gamma}_{ave} = 21573\ s^{-1}$
C=168.7
α=0.89
F_{max}=40.2
$\dot{\gamma}_{ave} = 21573\ s^{-1}$
C=135.4
α=0.89
F_{max}=32.3
$\dot{\gamma}_{ave} = 32144\ s^{-1}$
C=327.4
α=0.88
F_{max}=80.1
$\dot{\gamma}_{ave} = 51445\ s^{-1}$
C=201.9
α=0.84
F_{max}=52.2
$\dot{\gamma}_{ave} = 49658\ s^{-1}$
C=274.9
α=0.84
F_{max}=70.9
$\dot{\gamma}_{ave} = 49698\ s^{-1}$
C=347.1
α=0.85
F_{max}=89.1
$\dot{\gamma}_{ave} = 122295\ s^{-1}$
C=748.2
α=0.78
F_{max}=214.1
$\dot{\gamma}_{ave} = 118197\ s^{-1}$
C=1999.6
α=0.78
F_{max}=565.2
$\dot{\gamma}_{ave} = 121644\ s^{-1}$
C=2098.4
α=0.78
F_{max}=596.6
$\dot{\gamma}_{ave} = 151003\ s^{-1}$
C=1854.6
α=0.76
F_{max}=540.9
$\dot{\gamma}_{ave} = 295229\ s^{-1}$
C=1851.2
α=0.71
F_{max}=591.4
$\dot{\gamma}_{ave} = 187614\ s^{-1}$
C=2415
α=0.75
F_{max}=720.2
$\dot{\gamma}_{ave} = 303203\ s^{-1}$
C=4366.5
α=0.71
F_{max}=1391.7
$\dot{\gamma}_{ave} = 325883\ s^{-1}$
C=4187.4
α=0.71
F_{max}=1341.1
$\dot{\gamma}_{ave} = 386786\ s^{-1}$
C=4979.8
α=0.69
F_{max}=1633.1
[tonf]
[m/s]

SF1 Annular Orif. Parametric Analysis Results A = 4.8 [cm] f = 1 [Hz]

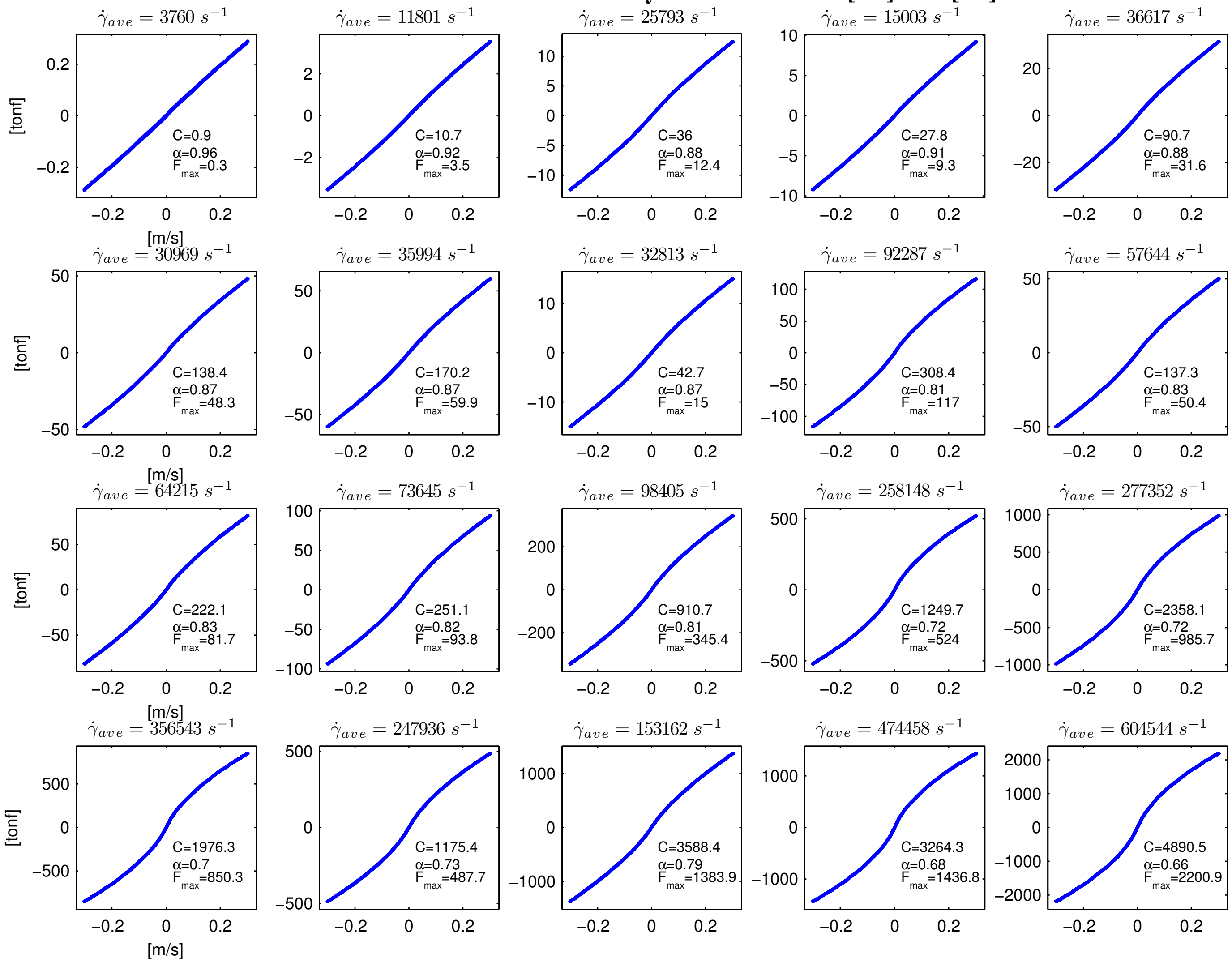

SF1 Annular Orif. Parametric Analysis Results A = 6.4 [cm] f = 1 [Hz]

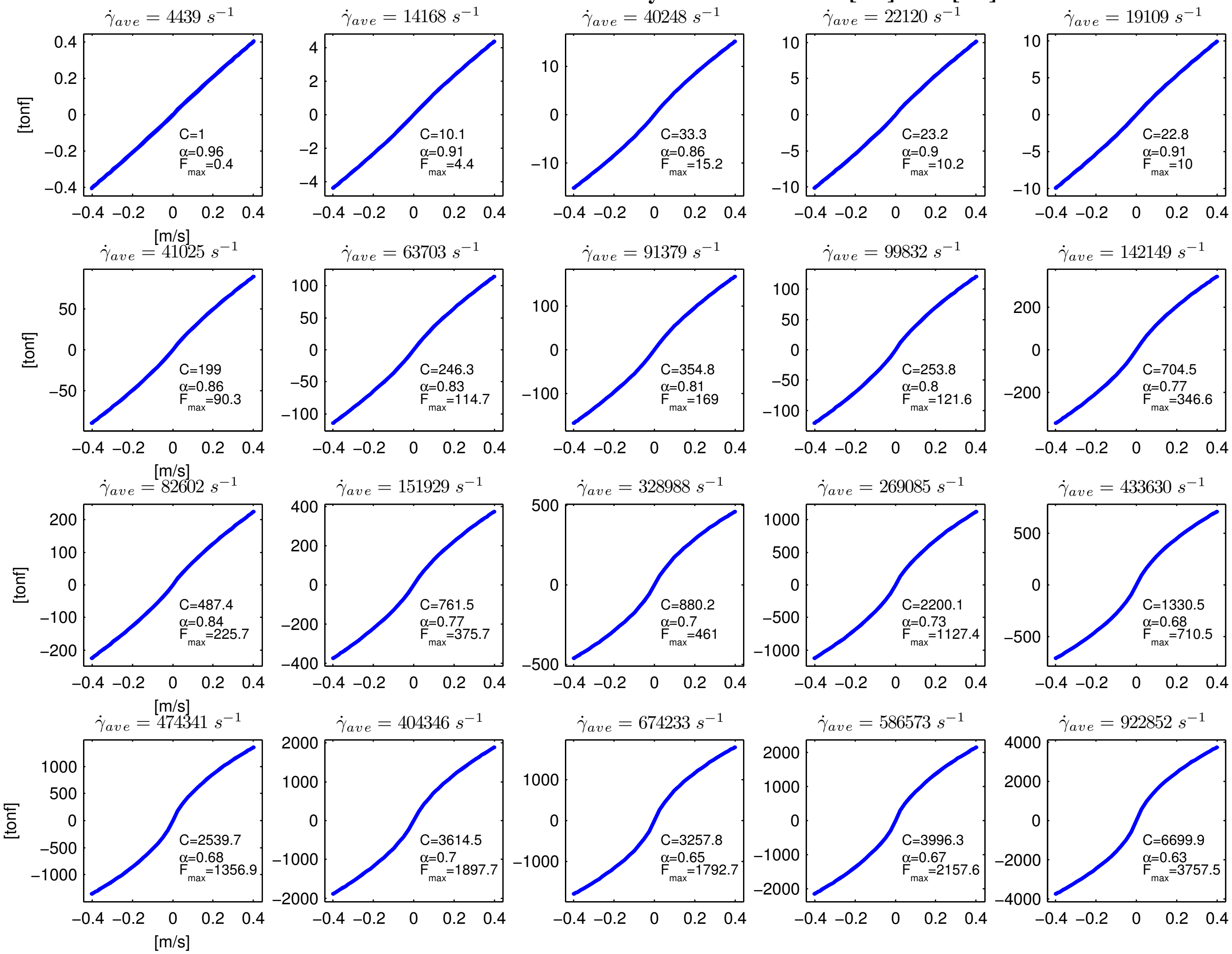

SF1 Annular Orif. Parametric Analysis Results A = 4 [cm] f = 2 [Hz]

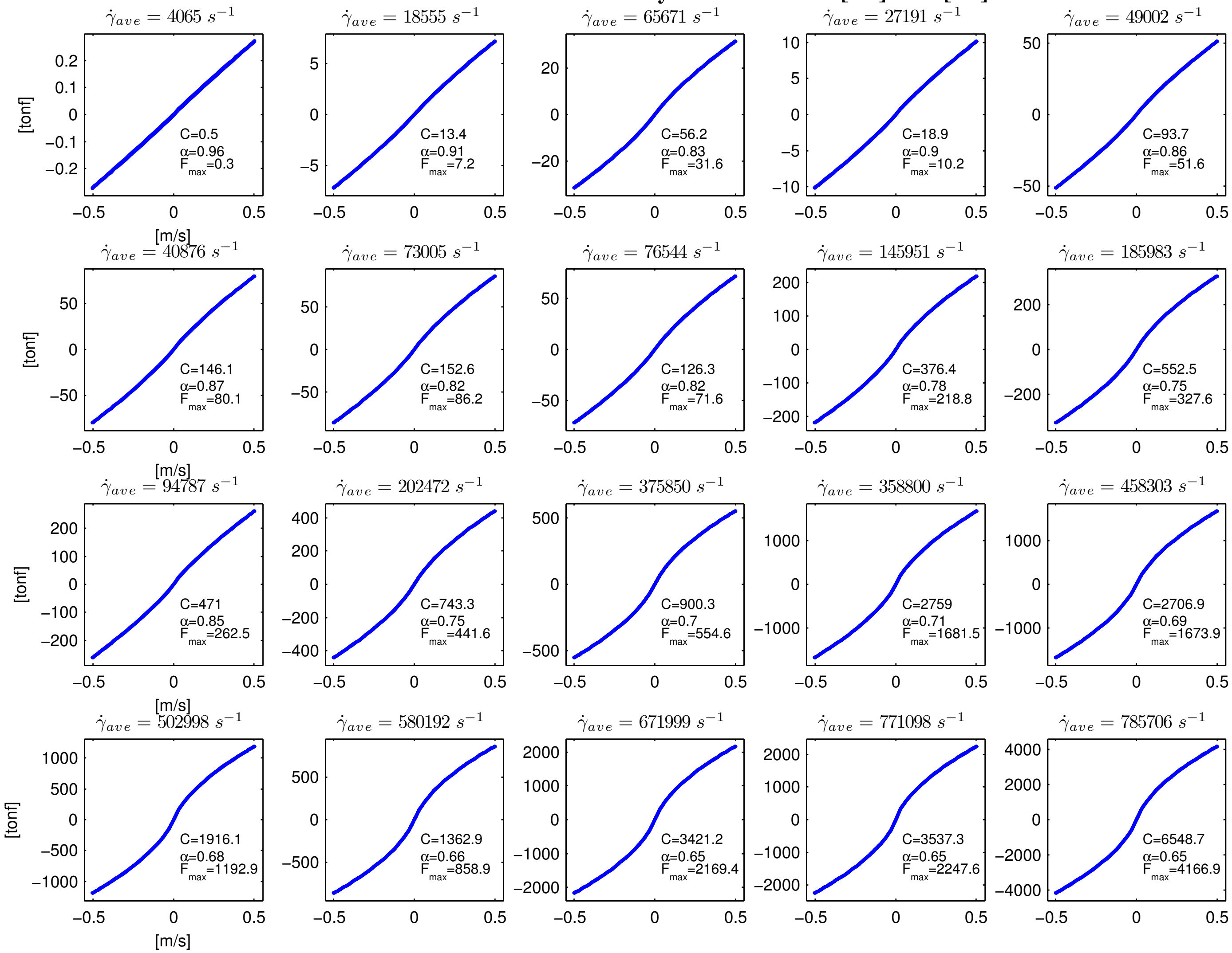

SF30 Annular Orif. Parametric Analysis Results A = 3.2 [cm] f = 0.5 [Hz]

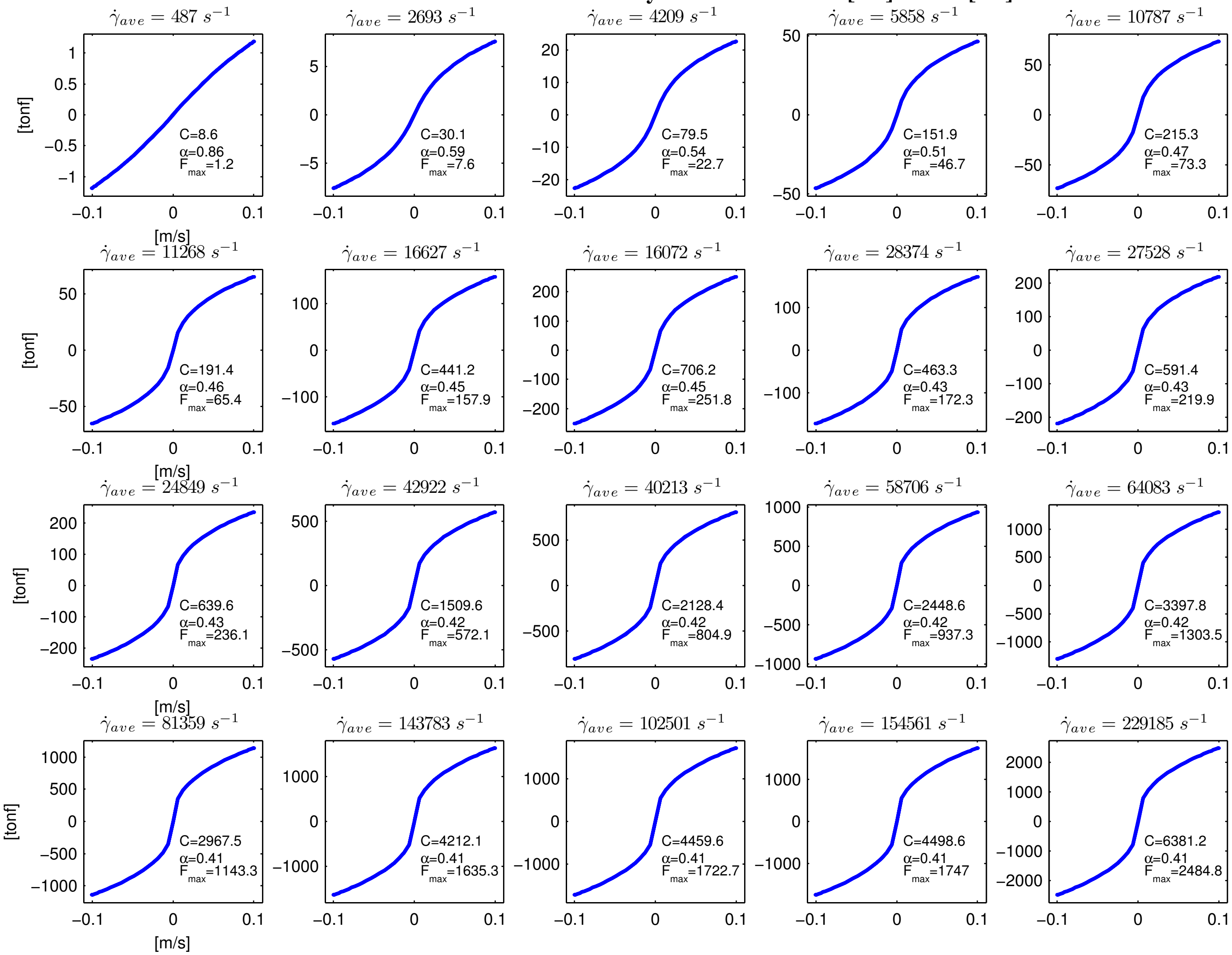

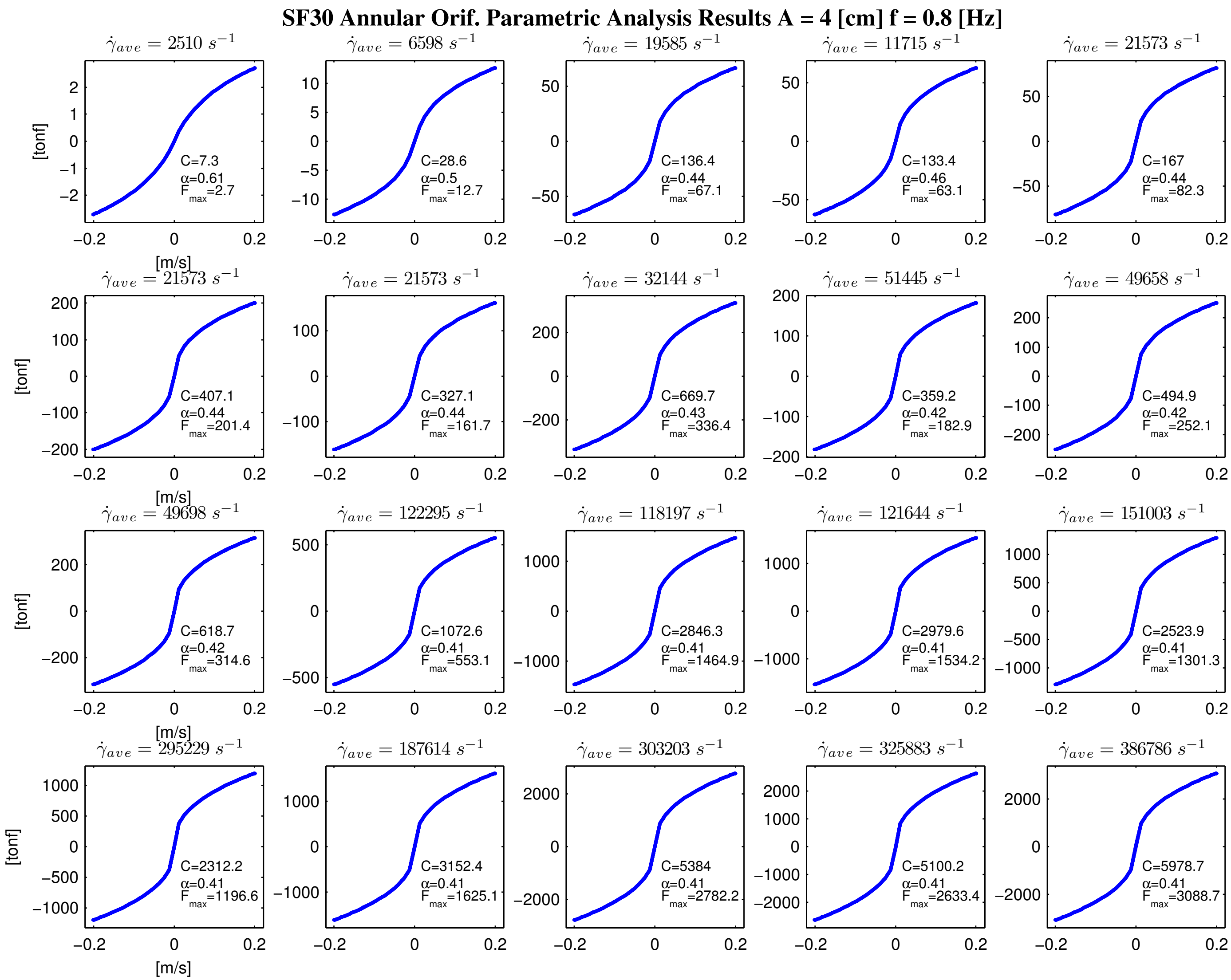
SF30 Annular Orif. Parametric Analysis Results A = 4 [cm] f = 0.8 [Hz]
$\dot{\gamma}_{ave} = 2510\ s^{-1}$
C=7.3
α=0.61
F_{max}=2.7
$\dot{\gamma}_{ave} = 6598\ s^{-1}$
C=28.6
α=0.5
F_{max}=12.7
$\dot{\gamma}_{ave} = 19585\ s^{-1}$
C=136.4
α=0.44
F_{max}=67.1
$\dot{\gamma}_{ave} = 11715\ s^{-1}$
C=133.4
α=0.46
F_{max}=63.1
$\dot{\gamma}_{ave} = 21573\ s^{-1}$
C=167
α=0.44
F_{max}=82.3
$\dot{\gamma}_{ave} = 21573\ s^{-1}$
C=407.1
α=0.44
F_{max}=201.4
$\dot{\gamma}_{ave} = 21573\ s^{-1}$
C=327.1
α=0.44
F_{max}=161.7
$\dot{\gamma}_{ave} = 32144\ s^{-1}$
C=669.7
α=0.43
F_{max}=336.4
$\dot{\gamma}_{ave} = 51445\ s^{-1}$
C=359.2
α=0.42
F_{max}=182.9
$\dot{\gamma}_{ave} = 49658\ s^{-1}$
C=494.9
α=0.42
F_{max}=252.1
$\dot{\gamma}_{ave} = 49698\ s^{-1}$
C=618.7
α=0.42
F_{max}=314.6
$\dot{\gamma}_{ave} = 122295\ s^{-1}$
C=1072.6
α=0.41
F_{max}=553.1
$\dot{\gamma}_{ave} = 118197\ s^{-1}$
C=2846.3
α=0.41
F_{max}=1464.9
$\dot{\gamma}_{ave} = 121644\ s^{-1}$
C=2979.6
α=0.41
F_{max}=1534.2
$\dot{\gamma}_{ave} = 151003\ s^{-1}$
C=2523.9
α=0.41
F_{max}=1301.3
$\dot{\gamma}_{ave} = 295229\ s^{-1}$
C=2312.2
α=0.41
F_{max}=1196.6
$\dot{\gamma}_{ave} = 187614\ s^{-1}$
C=3152.4
α=0.41
F_{max}=1625.1
$\dot{\gamma}_{ave} = 303203\ s^{-1}$
C=5384
α=0.41
F_{max}=2782.2
$\dot{\gamma}_{ave} = 325883\ s^{-1}$
C=5100.2
α=0.41
F_{max}=2633.4
$\dot{\gamma}_{ave} = 386786\ s^{-1}$
C=5978.7
α=0.41
F_{max}=3088.7
[tonf]
[m/s]

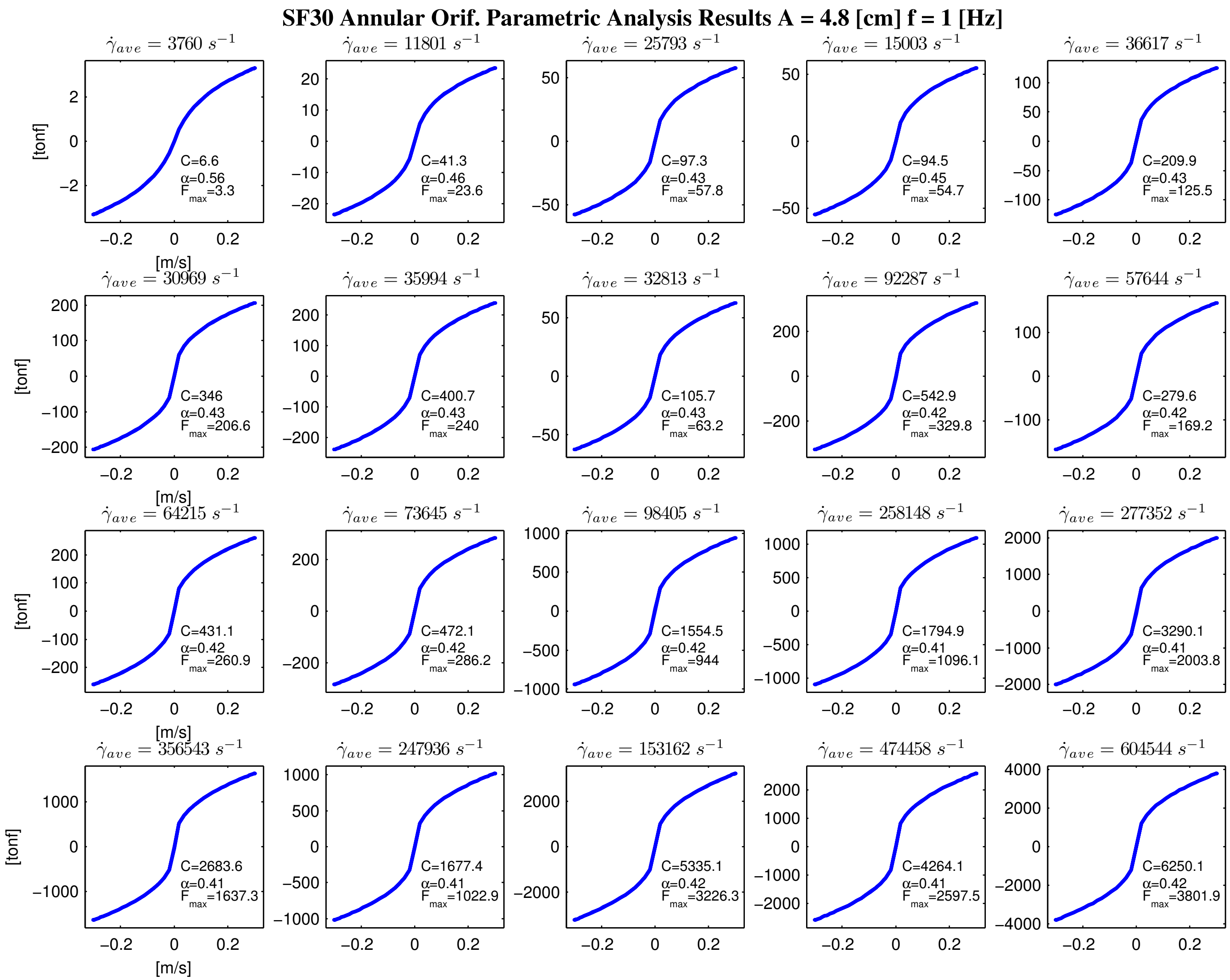

SF30 Annular Orif. Parametric Analysis Results A = 4.8 [cm] f = 1 [Hz]
$\dot{\gamma}_{ave} = 3760\ s^{-1}$
C=6.6
α=0.56
F_{max}=3.3
$\dot{\gamma}_{ave} = 11801\ s^{-1}$
C=41.3
α=0.46
F_{max}=23.6
$\dot{\gamma}_{ave} = 25793\ s^{-1}$
C=97.3
α=0.43
F_{max}=57.8
$\dot{\gamma}_{ave} = 15003\ s^{-1}$
C=94.5
α=0.45
F_{max}=54.7
$\dot{\gamma}_{ave} = 36617\ s^{-1}$
C=209.9
α=0.43
F_{max}=125.5
$\dot{\gamma}_{ave} = 30969\ s^{-1}$
C=346
α=0.43
F_{max}=206.6
$\dot{\gamma}_{ave} = 35994\ s^{-1}$
C=400.7
α=0.43
F_{max}=240
$\dot{\gamma}_{ave} = 32813\ s^{-1}$
C=105.7
α=0.43
F_{max}=63.2
$\dot{\gamma}_{ave} = 92287\ s^{-1}$
C=542.9
α=0.42
F_{max}=329.8
$\dot{\gamma}_{ave} = 57644\ s^{-1}$
C=279.6
α=0.42
F_{max}=169.2
$\dot{\gamma}_{ave} = 64215\ s^{-1}$
C=431.1
α=0.42
F_{max}=260.9
$\dot{\gamma}_{ave} = 73645\ s^{-1}$
C=472.1
α=0.42
F_{max}=286.2
$\dot{\gamma}_{ave} = 98405\ s^{-1}$
C=1554.5
α=0.42
F_{max}=944
$\dot{\gamma}_{ave} = 258148\ s^{-1}$
C=1794.9
α=0.41
F_{max}=1096.1
$\dot{\gamma}_{ave} = 277352\ s^{-1}$
C=3290.1
α=0.41
F_{max}=2003.8
$\dot{\gamma}_{ave} = 356543\ s^{-1}$
C=2683.6
α=0.41
F_{max}=1637.3
$\dot{\gamma}_{ave} = 247936\ s^{-1}$
C=1677.4
α=0.41
F_{max}=1022.9
$\dot{\gamma}_{ave} = 153162\ s^{-1}$
C=5335.1
α=0.42
F_{max}=3226.3
$\dot{\gamma}_{ave} = 474458\ s^{-1}$
C=4264.1
α=0.41
F_{max}=2597.5
$\dot{\gamma}_{ave} = 604544\ s^{-1}$
C=6250.1
α=0.42
F_{max}=3801.9
[tonf]
[m/s]

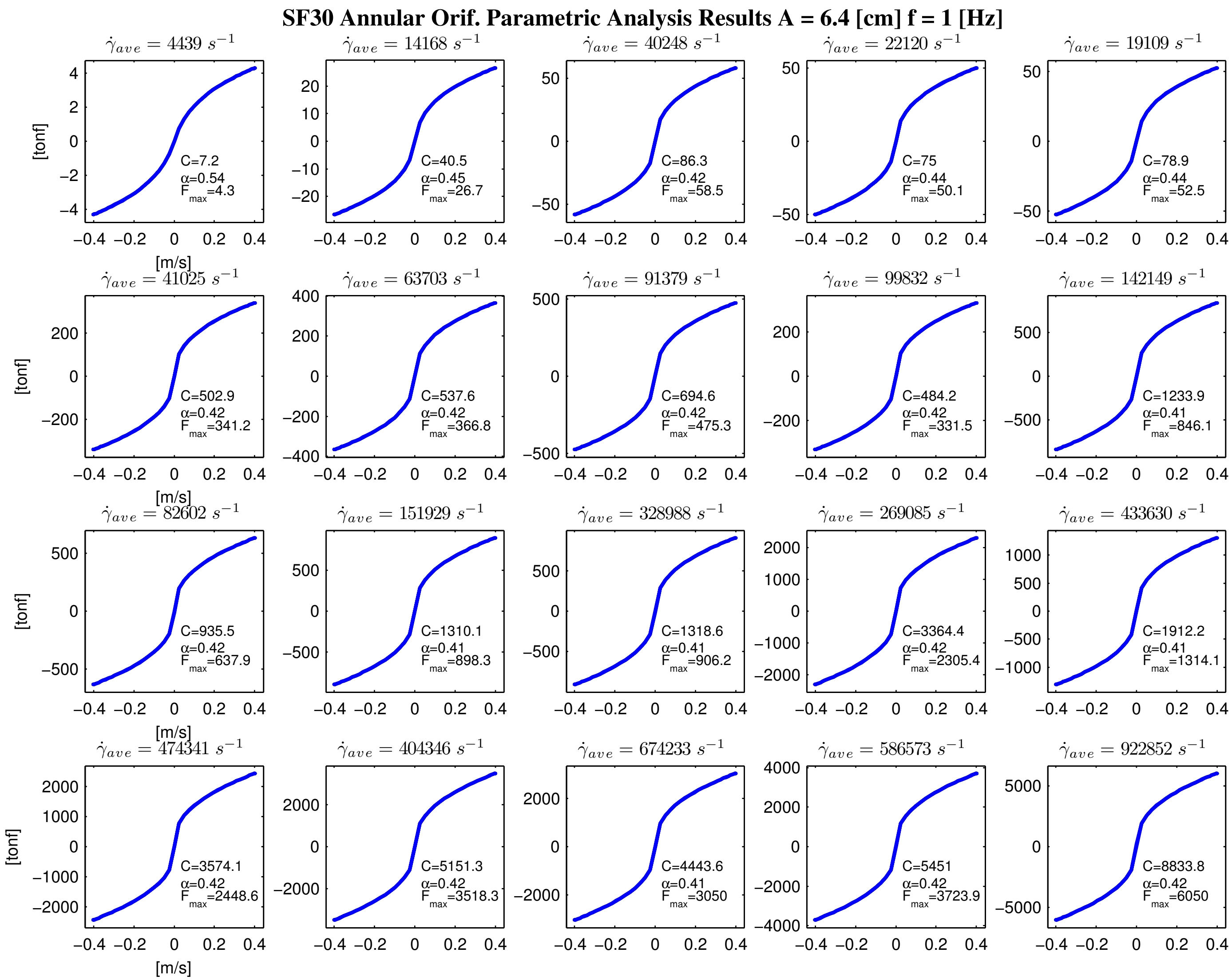
SF30 Annular Orif. Parametric Analysis Results A = 6.4 [cm] f = 1 [Hz]
$\dot{\gamma}_{ave} = 4439\ s^{-1}$
C=7.2
α=0.54
F_{max}=4.3
$\dot{\gamma}_{ave} = 14168\ s^{-1}$
C=40.5
α=0.45
F_{max}=26.7
$\dot{\gamma}_{ave} = 40248\ s^{-1}$
C=86.3
α=0.42
F_{max}=58.5
$\dot{\gamma}_{ave} = 22120\ s^{-1}$
C=75
α=0.44
F_{max}=50.1
$\dot{\gamma}_{ave} = 19109\ s^{-1}$
C=78.9
α=0.44
F_{max}=52.5
$\dot{\gamma}_{ave} = 41025\ s^{-1}$
C=502.9
α=0.42
F_{max}=341.2
$\dot{\gamma}_{ave} = 63703\ s^{-1}$
C=537.6
α=0.42
F_{max}=366.8
$\dot{\gamma}_{ave} = 91379\ s^{-1}$
C=694.6
α=0.42
F_{max}=475.3
$\dot{\gamma}_{ave} = 99832\ s^{-1}$
C=484.2
α=0.42
F_{max}=331.5
$\dot{\gamma}_{ave} = 142149\ s^{-1}$
C=1233.9
α=0.41
F_{max}=846.1
$\dot{\gamma}_{ave} = 82602\ s^{-1}$
C=935.5
α=0.42
F_{max}=637.9
$\dot{\gamma}_{ave} = 151929\ s^{-1}$
C=1310.1
α=0.41
F_{max}=898.3
$\dot{\gamma}_{ave} = 328988\ s^{-1}$
C=1318.6
α=0.41
F_{max}=906.2
$\dot{\gamma}_{ave} = 269085\ s^{-1}$
C=3364.4
α=0.42
F_{max}=2305.4
$\dot{\gamma}_{ave} = 433630\ s^{-1}$
C=1912.2
α=0.41
F_{max}=1314.1
$\dot{\gamma}_{ave} = 474341\ s^{-1}$
C=3574.1
α=0.42
F_{max}=2448.6
$\dot{\gamma}_{ave} = 404346\ s^{-1}$
C=5151.3
α=0.42
F_{max}=3518.3
$\dot{\gamma}_{ave} = 674233\ s^{-1}$
C=4443.6
α=0.41
F_{max}=3050
$\dot{\gamma}_{ave} = 586573\ s^{-1}$
C=5451
α=0.42
F_{max}=3723.9
$\dot{\gamma}_{ave} = 922852\ s^{-1}$
C=8833.8
α=0.42
F_{max}=6050
[tonf]
[m/s]

SF30 Annular Orif. Parametric Analysis Results A = 4 [cm] f = 2 [Hz]

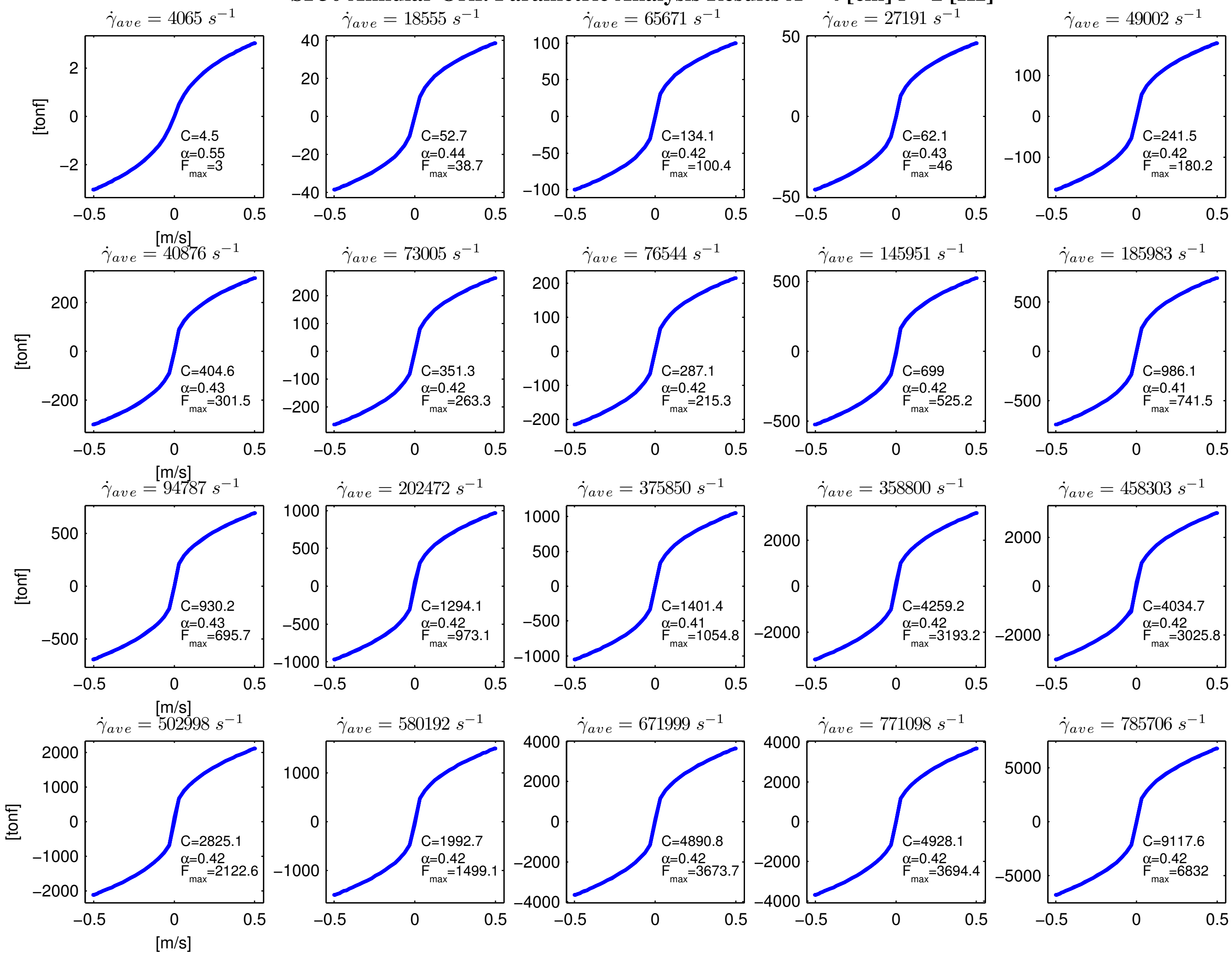

Piston with Cylindrical Orifices Using SF1 Fluid

The geometric dimensions and corresponding force-velocity curves of the models solved to generate Figure 3-5 (a) were:

Group 1

	N	R_p (cm)	R_v (cm)	R_o (mm)	L_p (cm)	R_i (mm)	A (cm)	f $(1/s)$	k_c	μ_{ave} $(Pa{\cdot}s)$
1	23	14.827	4.200	2.900	14.898	29.649	1.689	0.368	0.0155	0.902
2	13	4.930	0.900	3.100	19.467	13.444	5.276	0.979	0.0207	0.883
3	14	7.607	4.500	3.800	16.940	16.393	5.197	0.835	0.0290	0.905
4	20	12.302	3.800	3.800	13.855	26.164	16.001	0.099	0.0329	0.908
5	22	14.063	4.000	4.500	12.025	28.744	2.911	0.675	0.0563	0.914
6	12	9.253	1.200	4.100	12.033	26.484	11.594	0.222	0.0641	0.893
7	15	8.439	2.000	3.200	3.571	21.168	7.019	0.193	0.0710	0.912
8	8	10.944	2.900	5.300	15.212	37.308	2.899	0.779	0.0870	0.905
9	8	6.615	0.900	4.000	5.800	23.170	3.120	1.010	0.1244	0.893
10	6	6.078	1.400	5.000	8.433	24.145	17.374	0.247	0.1243	0.908
11	15	13.797	3.100	5.400	14.126	34.712	3.637	0.982	0.1302	0.891
12	11	8.127	1.100	5.000	8.527	24.279	7.300	0.830	0.1796	0.888
13	7	9.709	2.700	5.500	7.530	35.250	5.750	0.460	0.1830	0.909
14	16	11.959	3.200	5.500	9.610	28.809	3.000	1.790	0.1980	0.892
15	21	10.841	2.400	4.500	4.170	23.069	7.996	0.480	0.2068	0.902
16	5	6.788	1.000	6.400	13.386	30.024	17.061	0.483	0.2380	0.889
17	9	8.940	0.300	7.100	13.300	29.783	14.400	0.738	0.3025	0.893
18	6	9.229	1.100	8.000	16.240	37.408	10.400	0.808	0.3061	0.901
19	8	13.178	2.700	7.400	12.930	45.601	2.721	1.800	0.3350	0.896
20	16	10.490	3.000	5.900	7.540	25.130	8.036	1.278	0.3713	0.882

Group 2

	N	R_p (*cm*)	R_v (*cm*)	R_o (*mm*)	L_p (*cm*)	R_i (*mm*)	A (*cm*)	f (1/*s*)	k_c	μ_{ave} (*Pa·s*)
1	14	6.464	1.616	2.500	18.852	16.726	1.862	0.745	0.009	0.897
2	19	8.982	2.246	2.900	19.324	19.953	1.550	0.739	0.010	0.911
3	9	6.899	1.725	3.500	15.690	22.266	2.728	0.742	0.027	0.900
4	18	6.934	1.733	3.300	11.100	15.824	2.186	1.501	0.031	0.901
5	18	7.130	1.533	3.500	15.209	16.412	3.800	1.190	0.034	0.889
6	8	13.772	3.443	3.400	5.293	47.147	2.296	0.182	0.075	0.899
7	7	6.620	1.655	5.400	15.048	24.228	1.500	3.800	0.094	0.905
8	24	7.967	1.992	6.000	21.342	15.745	14.851	1.311	0.095	0.902
9	16	15.051	3.763	5.900	20.384	36.434	2.438	1.546	0.104	0.898
10	5	9.074	2.268	4.500	9.173	39.290	1.300	1.171	0.109	0.894
11	16	10.561	2.640	6.100	17.673	25.563	5.500	1.280	0.109	0.907
12	14	7.017	1.754	4.200	4.217	18.157	9.756	0.477	0.153	0.906
13	10	11.054	2.764	6.500	20.409	33.847	4.987	1.373	0.165	0.888
14	13	9.321	2.330	6.500	18.026	25.031	13.999	0.941	0.197	0.885
15	6	13.614	3.404	7.500	20.050	53.815	5.900	0.600	0.217	0.898
16	4	6.809	1.702	7.400	12.327	32.962	14.482	0.420	0.223	0.918
17	11	8.973	2.243	8.000	16.673	26.197	7.700	1.735	0.229	0.913
18	14	12.311	3.078	7.400	17.543	31.857	13.706	0.918	0.314	0.883
19	16	15.954	3.988	5.300	5.017	38.618	3.200	0.970	0.398	0.883
20	7	14.972	3.743	6.200	6.292	54.792	6.200	0.330	0.416	0.894

Group 3

	N	R_p (*cm*)	R_v (*cm*)	R_o (*mm*)	L_p (*cm*)	R_i (*mm*)	A (*cm*)	f (1/*s*)	k_c	μ_{ave} (*Pa·s*)
1	13	6.357	1.589	2.000	19.324	17.072	1.550	1.663	0.019	0.796
2	20	12.557	3.139	2.200	18.852	27.188	1.862	0.710	0.025	0.799
3	23	8.769	2.192	2.600	20.409	17.704	4.987	1.066	0.039	0.795
4	16	6.318	1.580	1.800	4.217	15.294	9.756	0.217	0.056	0.806
5	20	15.502	3.876	1.800	5.017	33.563	9.800	0.054	0.057	0.789
6	13	6.462	1.615	3.100	18.026	17.352	3.999	1.861	0.058	0.817
7	20	6.971	1.743	3.200	20.050	15.093	5.900	1.869	0.059	0.815
8	6	13.060	3.265	3.100	17.673	51.626	5.500	0.161	0.063	0.812
9	7	12.555	3.139	3.400	20.384	45.946	2.438	0.767	0.093	0.790
10	14	6.344	1.586	2.600	6.292	16.418	7.200	0.681	0.098	0.817
11	22	15.340	3.835	2.800	11.100	31.666	2.186	1.104	0.106	0.781
12	22	9.171	2.293	3.600	17.543	18.932	13.706	0.944	0.127	0.791
13	23	7.712	1.928	3.300	9.173	15.570	10.300	1.140	0.145	0.812
14	16	12.787	3.197	4.100	15.209	30.953	3.800	1.835	0.211	0.793
15	9	13.431	3.358	4.700	15.048	43.349	3.500	1.517	0.318	0.794
16	6	14.491	3.623	4.700	15.690	57.282	2.728	1.175	0.324	0.789
17	12	12.948	3.237	5.300	16.673	36.192	7.700	1.142	0.323	0.815
18	14	9.922	2.481	5.500	21.342	25.676	14.851	1.510	0.329	0.802
19	5	13.577	3.394	3.900	5.293	58.792	2.296	0.579	0.406	0.814
20	6	14.235	3.559	5.400	12.327	56.267	14.482	0.269	0.468	0.814

Group 4

	N	R_p (*cm*)	R_v (*cm*)	R_o (*mm*)	L_p (*cm*)	R_i (*mm*)	A (*cm*)	f (1/*s*)	k_c	μ_{ave} (*Pa·s*)
1	15	14.001	3.500	1.400	9.039	35.002	1.290	0.171	0.014	0.792
2	4	7.067	1.767	2.900	21.914	34.211	15.627	0.099	0.038	0.819
3	7	7.361	1.840	2.600	14.274	26.937	3.463	0.620	0.052	0.802
4	22	7.818	1.955	3.300	22.957	16.140	12.400	0.979	0.065	0.803
5	18	11.797	2.949	3.500	22.901	26.923	4.700	1.026	0.072	0.810
6	14	6.046	1.512	2.600	11.370	15.646	4.910	1.492	0.076	0.788
7	4	8.638	2.160	1.900	3.841	41.819	0.407	0.877	0.077	0.800
8	16	14.687	3.672	2.600	5.595	35.551	2.726	0.375	0.107	0.819
9	13	7.455	1.864	3.700	14.308	20.021	10.956	0.899	0.129	0.814
10	19	15.619	3.905	4.200	17.063	34.695	7.856	0.600	0.155	0.816
11	12	14.173	3.543	3.900	10.438	39.615	2.019	1.377	0.194	0.819
12	21	9.998	2.499	4.100	7.590	21.124	9.100	1.255	0.312	0.819
13	13	7.450	1.862	4.100	6.335	20.005	9.073	1.592	0.431	0.807
14	7	10.314	2.579	5.100	12.763	37.746	4.772	1.859	0.475	0.795
15	7	11.499	2.875	5.700	15.754	42.081	6.100	1.637	0.538	0.795
16	32	14.693	3.673	4.200	6.092	25.149	11.017	1.022	0.561	0.794
17	8	15.106	3.777	5.000	8.043	51.713	5.800	0.650	0.589	0.811
18	6	8.599	2.150	4.700	7.862	33.989	5.500	1.563	0.605	0.795
19	9	13.749	3.437	4.100	4.778	44.375	8.138	0.386	0.616	0.801
20	5	6.844	1.711	5.200	9.038	29.637	18.847	0.743	0.646	0.803

Group 5

	N	R_p (*cm*)	R_v (*cm*)	R_o (*mm*)	L_p (*cm*)	R_i (*mm*)	A (*cm*)	f (1/*s*)	k_c	μ_{ave} (*Pa·s*)
1	20	10.401	2.600	1.600	18.182	22.519	3.916	0.480	0.029	0.695
2	17	7.537	1.884	2.200	11.234	17.698	16.888	0.426	0.108	0.707
3	15	6.908	1.727	2.600	18.024	17.271	9.522	1.275	0.108	0.710
4	10	8.407	2.102	2.700	13.679	25.741	3.913	1.627	0.167	0.705
5	8	11.181	3.600	3.700	23.236	37.424	10.454	0.723	0.245	0.708
6	4	8.665	2.166	3.600	21.732	41.948	3.139	1.891	0.262	0.700
7	5	12.718	3.180	3.500	20.480	55.071	1.977	1.668	0.268	0.695
8	12	8.810	2.203	3.600	20.391	24.625	12.187	1.421	0.281	0.699
9	7	10.574	2.644	3.500	16.646	38.698	4.933	1.219	0.291	0.708
10	16	13.788	3.447	2.900	9.351	33.375	3.600	1.299	0.301	0.706
11	23	6.680	1.670	2.400	4.751	13.486	12.924	1.231	0.328	0.708
12	16	14.754	3.688	4.400	24.122	35.713	15.357	0.906	0.395	0.709
13	8	12.761	3.190	4.100	20.173	43.685	10.567	0.738	0.399	0.704
14	14	11.271	2.818	2.400	4.141	29.168	14.795	0.248	0.410	0.699
15	9	12.377	3.094	3.800	13.711	39.947	4.854	1.543	0.472	0.703
16	3	8.891	2.223	4.300	18.772	49.700	9.699	0.685	0.469	0.710
17	5	14.577	3.894	4.100	14.911	62.821	5.821	0.707	0.598	0.693
18	4	12.951	3.238	4.200	13.899	62.701	7.600	0.520	0.602	0.708
19	16	13.436	3.859	3.100	4.024	32.175	5.333	1.127	0.832	0.708
20	14	10.235	2.559	3.900	8.705	26.484	14.463	1.361	0.870	0.695

Group 6

	N	R_p (cm)	R_v (cm)	R_o (mm)	L_p (cm)	R_i (mm)	*A* (cm)	*f* (1/s)	k_c	μ_{ave} (Pa·s)
1	14	11.254	2.814	1.800	18.352	29.123	6.619	0.232	0.039	0.700
2	16	7.389	1.847	1.600	11.544	17.885	4.399	0.644	0.043	0.701
3	16	15.727	3.932	1.800	13.290	38.070	15.126	0.065	0.060	0.688
4	18	11.303	2.826	2.300	18.785	25.796	13.458	0.281	0.072	0.710
5	13	7.920	1.980	2.900	18.444	21.269	7.610	1.582	0.161	0.700
6	14	12.963	3.241	3.100	19.463	33.544	5.829	1.073	0.199	0.693
7	16	6.938	1.735	3.100	12.289	16.795	18.991	1.189	0.280	0.706
8	21	9.658	2.415	3.400	16.308	20.407	17.767	1.180	0.291	0.701
9	8	13.635	3.409	2.800	9.505	46.676	7.885	0.318	0.319	0.687
10	7	9.935	2.484	3.400	10.948	36.357	15.400	0.388	0.385	0.713
11	24	10.849	2.712	2.600	4.411	21.441	16.687	0.495	0.466	0.704
12	5	13.720	3.430	4.400	19.854	59.408	5.996	0.820	0.468	0.712
13	15	10.046	2.511	3.600	11.302	25.114	16.452	1.034	0.519	0.697
14	4	12.714	3.179	3.900	12.910	61.553	3.428	0.995	0.542	0.703
15	7	13.413	3.353	3.700	9.676	49.085	17.253	0.254	0.586	0.709
16	3	11.201	2.800	3.500	8.138	62.613	19.798	0.119	0.616	0.704
17	6	8.279	3.070	3.100	4.934	31.389	15.405	0.408	0.674	0.709
18	13	14.611	3.653	4.500	13.288	39.238	8.829	1.361	0.745	0.712
19	17	15.329	3.832	4.600	12.098	35.997	9.589	1.500	0.816	0.719
20	16	14.484	2.621	3.600	7.150	35.612	5.055	1.770	0.877	0.689

Group 7

	N	R_p (cm)	R_v (cm)	R_o (mm)	L_p (cm)	R_i (mm)	*A* (cm)	*f* (1/s)	k_c	μ_{ave} (Pa·s)
1	14	7.781	0.900	1.350	22.794	20.656	1.889	1.388	0.031	0.605
2	4	8.126	2.621	1.900	19.990	38.459	1.064	1.887	0.092	0.612
3	15	8.089	1.735	1.900	22.841	20.401	6.828	1.220	0.098	0.590
4	19	8.999	3.653	1.200	4.973	18.869	12.658	0.186	0.108	0.596
5	20	7.341	3.832	1.800	14.614	14.001	8.112	1.599	0.108	0.611
6	24	12.000	3.750	2.000	15.000	23.268	7.400	1.000	0.172	0.591
7	22	12.754	3.409	1.500	5.961	26.202	10.709	0.219	0.172	0.598
8	10	6.567	3.932	2.000	9.092	16.633	16.534	0.799	0.253	0.604
9	7	11.219	2.826	1.600	5.129	41.036	9.306	0.133	0.262	0.589
10	14	7.040	3.430	1.800	6.135	16.431	10.722	0.976	0.294	0.596
11	8	9.455	2.511	3.000	24.903	32.229	7.174	1.582	0.295	0.611
12	21	9.596	1.847	1.800	5.501	20.549	5.950	1.118	0.326	0.597
13	8	11.972	3.070	3.000	22.263	40.913	10.952	0.655	0.338	0.608
14	5	10.685	2.484	2.500	10.455	46.474	12.109	0.264	0.414	0.609
15	24	15.121	2.712	2.800	13.577	30.366	10.569	1.104	0.508	0.594
16	9	15.052	2.415	2.500	8.130	49.522	1.831	1.485	0.509	0.614
17	5	9.358	1.980	2.900	13.276	40.905	11.621	0.563	0.517	0.607
18	8	11.619	3.353	2.900	10.244	39.330	15.649	0.471	0.706	0.601
19	5	7.842	2.800	2.800	7.303	32.758	15.567	0.612	0.887	0.601
20	6	7.757	3.241	2.600	4.279	28.770	13.392	0.682	1.098	0.613

Group 8

	N	R_p (cm)	R_v (cm)	R_o (mm)	L_p (cm)	R_i (mm)	A (cm)	f ($1/s$)	k_c	μ_{ave} ($Pa{\cdot}s$)
1	5	9.677	2.419	1.100	20.473	41.901	1.064	0.293	0.016	0.619
2	17	13.894	3.473	1.000	6.358	32.627	1.889	0.206	0.040	0.618
3	23	7.006	1.752	0.950	9.590	14.145	12.109	0.164	0.026	0.602
4	7	7.518	1.880	1.500	23.609	27.515	5.950	0.377	0.046	0.590
5	18	8.060	2.015	1.200	10.123	18.395	6.828	0.345	0.050	0.603
6	16	8.057	2.014	1.600	13.082	19.502	7.400	0.640	0.086	0.610
7	17	10.053	2.513	1.300	5.232	23.608	5.567	0.341	0.129	0.597
8	16	11.518	2.879	2.400	28.920	27.880	16.534	0.510	0.144	0.599
9	9	9.883	2.471	2.200	18.590	31.896	10.709	0.443	0.163	0.605
10	4	8.374	2.093	2.100	14.240	40.539	1.831	1.416	0.189	0.603
11	21	8.941	2.235	2.500	20.754	18.891	10.569	1.828	0.208	0.609
12	4	6.867	1.717	2.300	16.674	33.243	12.658	0.401	0.212	0.603
13	10	6.915	1.729	2.100	12.316	21.173	15.649	0.634	0.230	0.597
14	18	8.290	2.072	2.300	13.085	18.918	9.306	1.787	0.291	0.595
15	5	13.719	3.430	2.900	24.253	59.406	5.112	0.642	0.304	0.599
16	18	13.819	3.455	2.200	7.937	31.538	10.952	0.432	0.371	0.609
17	10	11.309	2.827	3.100	20.148	34.626	9.221	1.120	0.379	0.618
18	6	12.419	3.105	3.100	17.765	49.092	5.722	0.909	0.437	0.616
19	15	7.048	1.762	2.200	4.782	17.621	13.392	1.249	0.695	0.595
20	8	10.845	2.711	2.900	6.305	37.125	7.174	1.116	1.101	0.606

SF1 Cyl. Orif. Parametric Analysis Results Group 1, $\eta_{ave} \approx 0.9\,[Pa \cdot s]$

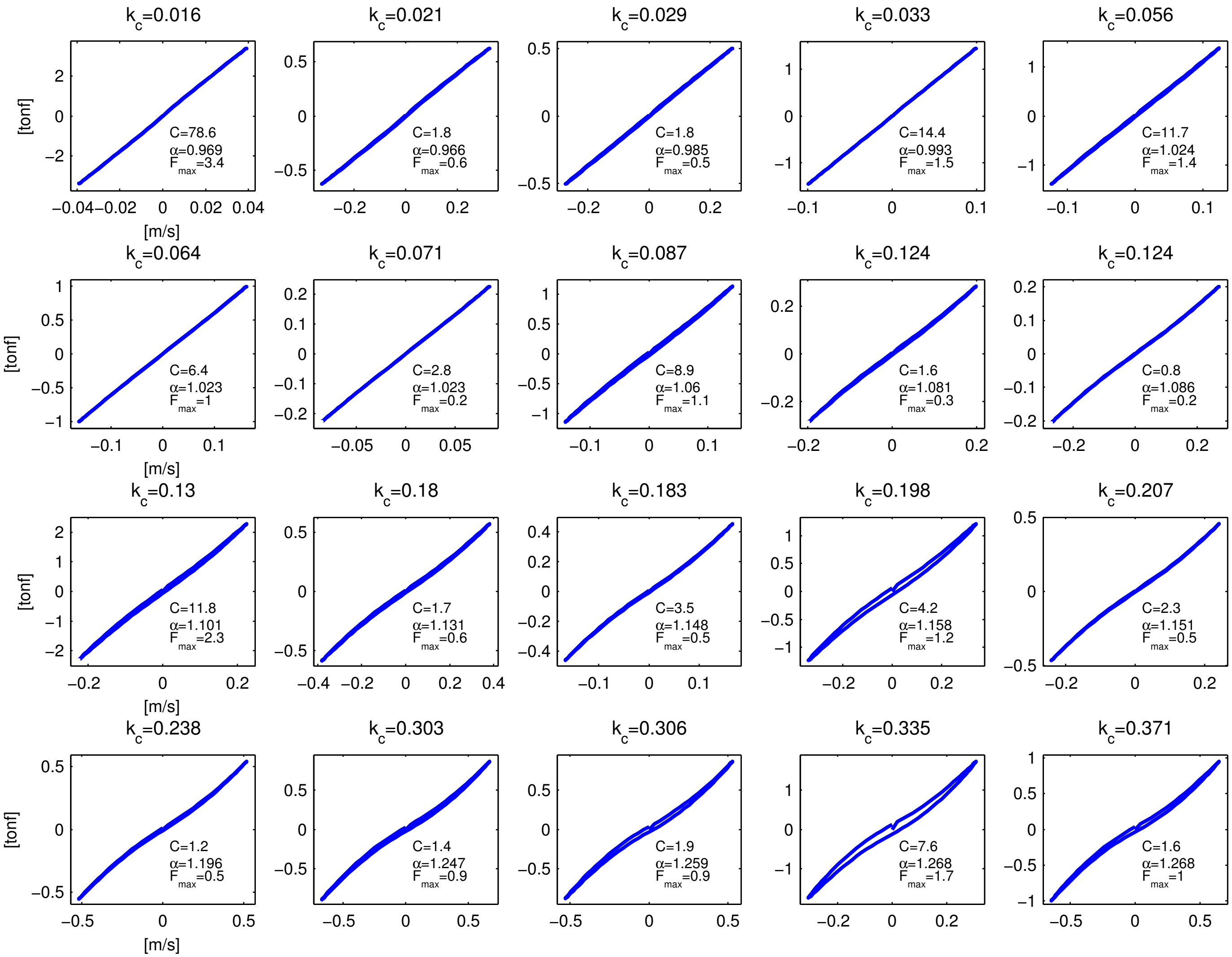

SF1 Cyl. Orif. Parametric Analysis Results Group 2, $\eta_{ave} \approx 0.9\,[Pa \cdot s]$

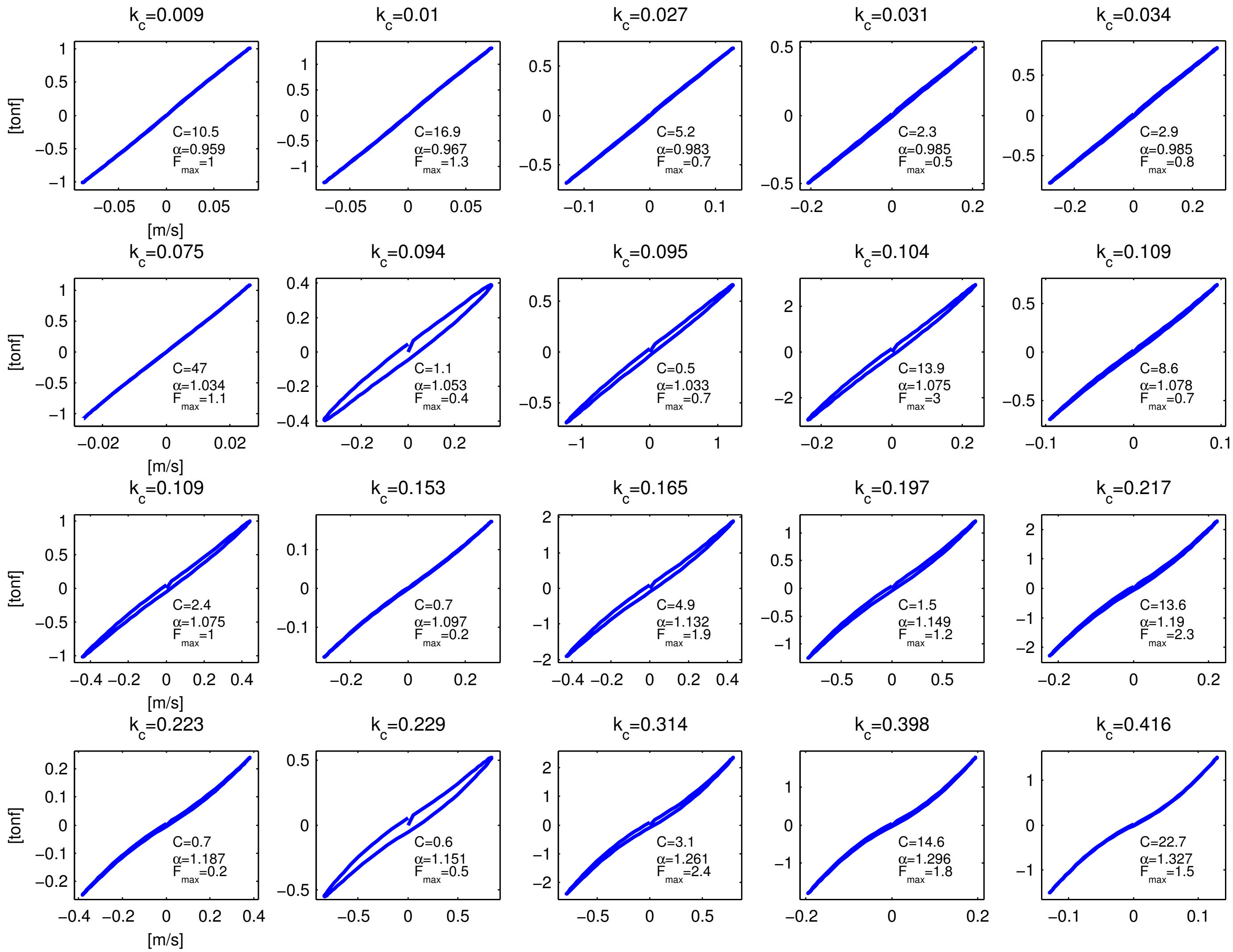

SF1 Cyl. Orif. Parametric Analysis Results Group 3, $\eta_{ave} \approx 0.8\,[Pa \cdot s]$

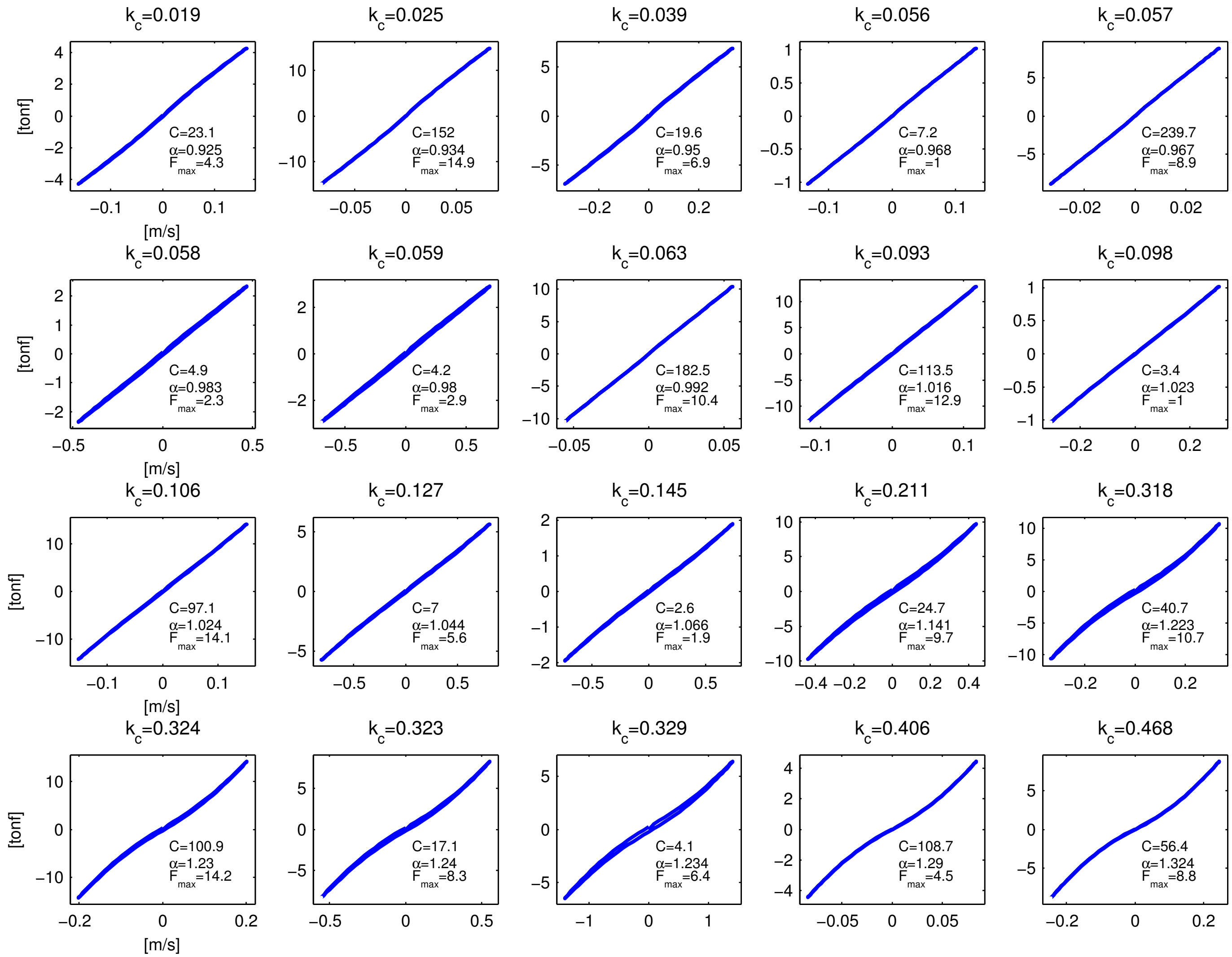

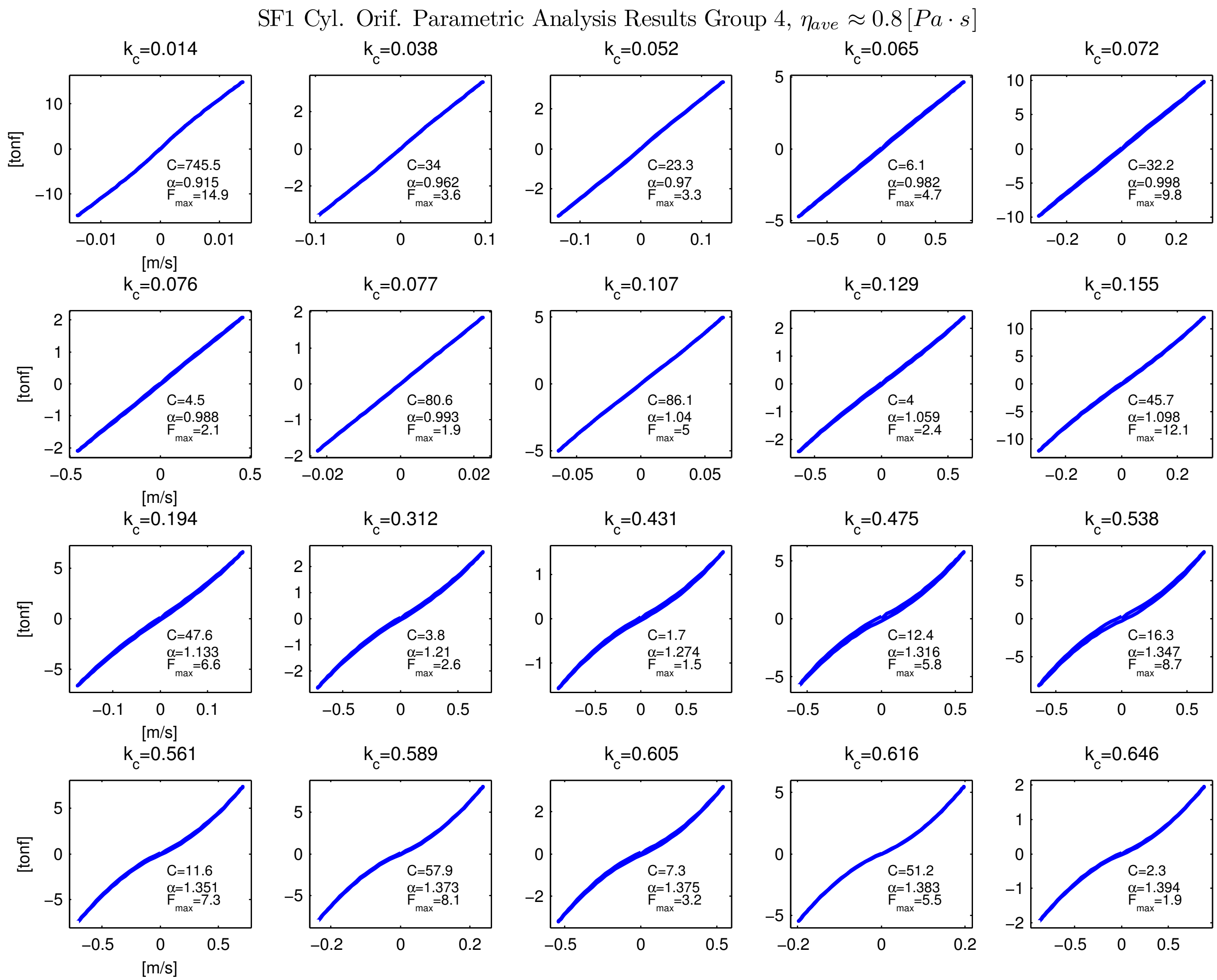
SF1 Cyl. Orif. Parametric Analysis Results Group 4, $\eta_{ave} \approx 0.8\,[Pa \cdot s]$
k_c=0.014
C=745.5
α=0.915
F_{max}=14.9
k_c=0.038
C=34
α=0.962
F_{max}=3.6
k_c=0.052
C=23.3
α=0.97
F_{max}=3.3
k_c=0.065
C=6.1
α=0.982
F_{max}=4.7
k_c=0.072
C=32.2
α=0.998
F_{max}=9.8
k_c=0.076
C=4.5
α=0.988
F_{max}=2.1
k_c=0.077
C=80.6
α=0.993
F_{max}=1.9
k_c=0.107
C=86.1
α=1.04
F_{max}=5
k_c=0.129
C=4
α=1.059
F_{max}=2.4
k_c=0.155
C=45.7
α=1.098
F_{max}=12.1
k_c=0.194
C=47.6
α=1.133
F_{max}=6.6
k_c=0.312
C=3.8
α=1.21
F_{max}=2.6
k_c=0.431
C=1.7
α=1.274
F_{max}=1.5
k_c=0.475
C=12.4
α=1.316
F_{max}=5.8
k_c=0.538
C=16.3
α=1.347
F_{max}=8.7
k_c=0.561
C=11.6
α=1.351
F_{max}=7.3
k_c=0.589
C=57.9
α=1.373
F_{max}=8.1
k_c=0.605
C=7.3
α=1.375
F_{max}=3.2
k_c=0.616
C=51.2
α=1.383
F_{max}=5.5
k_c=0.646
C=2.3
α=1.394
F_{max}=1.9
[tonf]
[m/s]

SF1 Cyl. Orif. Parametric Analysis Results Group 5, $\eta_{ave} \approx 0.7\,[Pa \cdot s]$

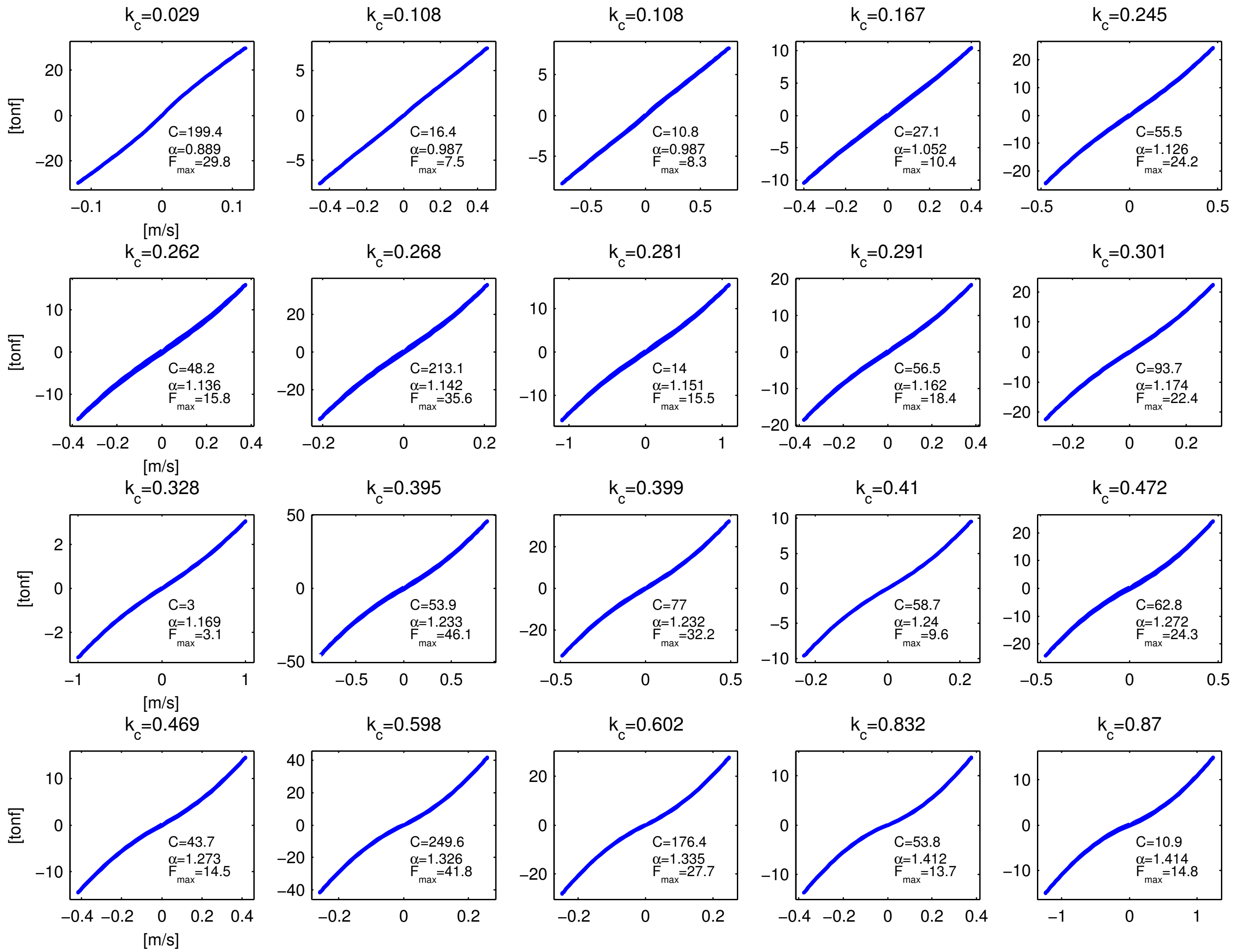

SF1 Cyl. Orif. Parametric Analysis Results Group 6, $\eta_{ave} \approx 0.7\,[Pa \cdot s]$

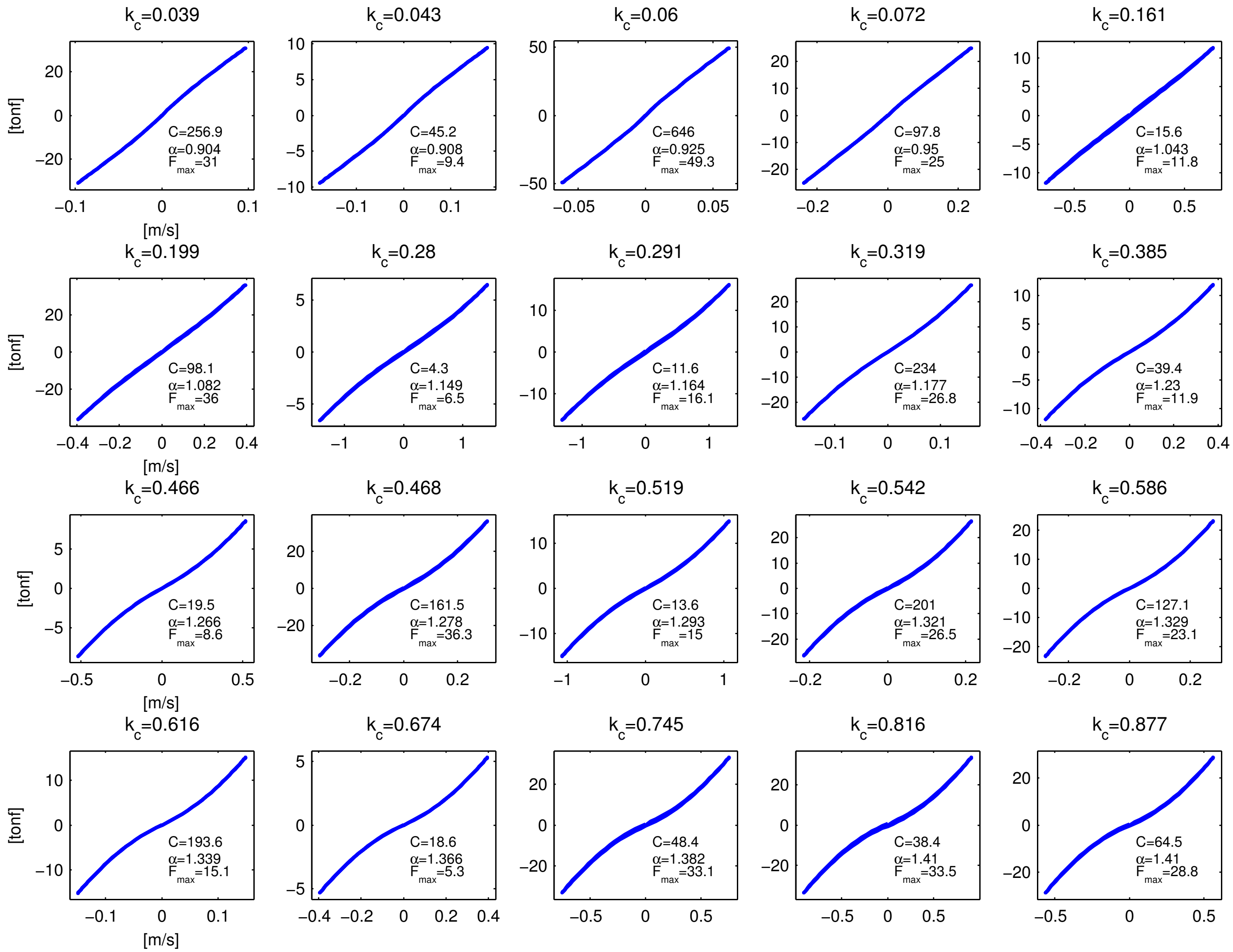

SF1 Cyl. Orif. Parametric Analysis Results Group 7, $\eta_{ave} \approx 0.6\,[Pa \cdot s]$

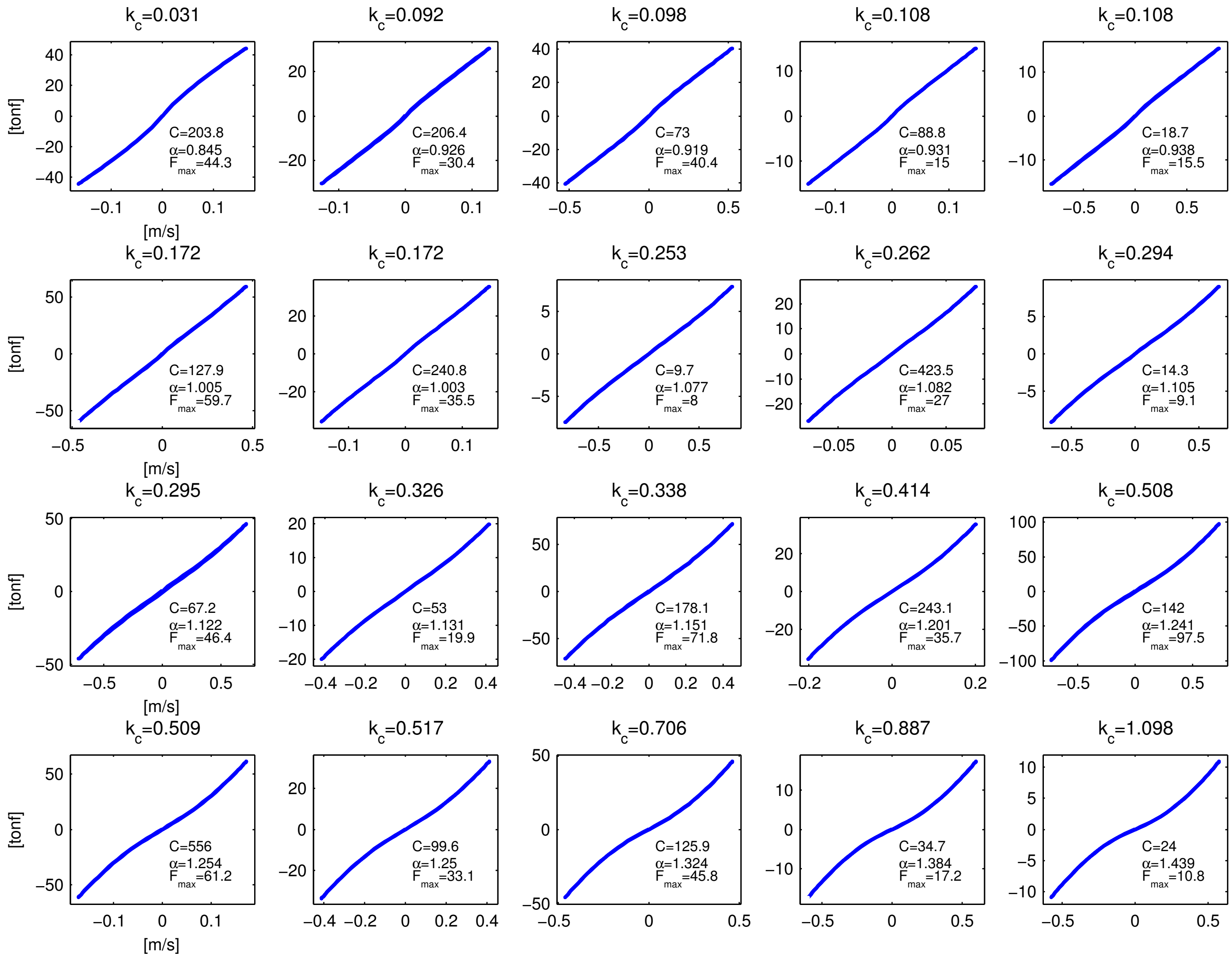

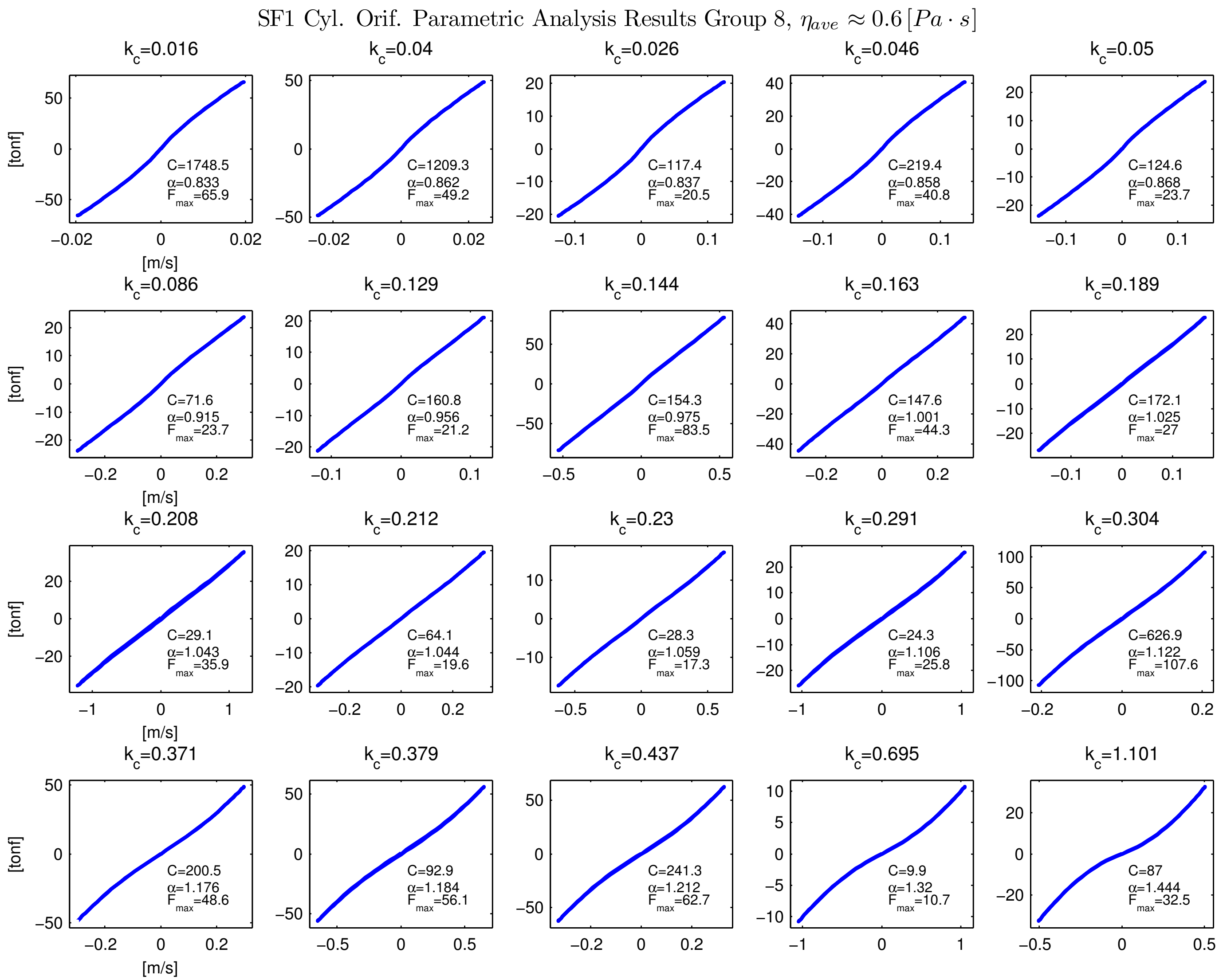
SF1 Cyl. Orif. Parametric Analysis Results Group 8, $\eta_{ave} \approx 0.6\,[Pa \cdot s]$
k_c=0.016
C=1748.5
α=0.833
F_{max}=65.9
k_c=0.04
C=1209.3
α=0.862
F_{max}=49.2
k_c=0.026
C=117.4
α=0.837
F_{max}=20.5
k_c=0.046
C=219.4
α=0.858
F_{max}=40.8
k_c=0.05
C=124.6
α=0.868
F_{max}=23.7
k_c=0.086
C=71.6
α=0.915
F_{max}=23.7
k_c=0.129
C=160.8
α=0.956
F_{max}=21.2
k_c=0.144
C=154.3
α=0.975
F_{max}=83.5
k_c=0.163
C=147.6
α=1.001
F_{max}=44.3
k_c=0.189
C=172.1
α=1.025
F_{max}=27
k_c=0.208
C=29.1
α=1.043
F_{max}=35.9
k_c=0.212
C=64.1
α=1.044
F_{max}=19.6
k_c=0.23
C=28.3
α=1.059
F_{max}=17.3
k_c=0.291
C=24.3
α=1.106
F_{max}=25.8
k_c=0.304
C=626.9
α=1.122
F_{max}=107.6
k_c=0.371
C=200.5
α=1.176
F_{max}=48.6
k_c=0.379
C=92.9
α=1.184
F_{max}=56.1
k_c=0.437
C=241.3
α=1.212
F_{max}=62.7
k_c=0.695
C=9.9
α=1.32
F_{max}=10.7
k_c=1.101
C=87
α=1.444
F_{max}=32.5
[tonf]
[m/s]

Piston with Cylindrical Orifices Using SF30 Fluid

The geometric dimensions and corresponding force-velocity curves of the models solved to generate Figure 3-5 (b) were:

Group 1

	N	R_p (cm)	R_v (cm)	R_o (mm)	L_p (cm)	R_i (mm)	A (cm)	f $(1/s)$	k_c	μ_{ave} $(Pa{\cdot}s)$
1	15	4.930	0.900	4.000	19.467	12.515	3.276	0.979	0.000556	17.656
2	23	14.827	4.200	4.100	14.898	29.649	1.689	0.368	0.000794	17.585
3	16	7.607	4.500	5.100	16.940	15.334	5.197	0.835	0.001288	17.803
4	22	12.302	3.800	4.900	13.855	24.946	15.001	0.099	0.001446	17.624
5	24	14.063	4.000	5.700	12.025	27.520	2.911	0.675	0.002699	17.478
6	14	9.253	1.200	5.800	12.033	24.520	11.594	0.222	0.002794	17.564
7	17	8.439	2.000	4.100	3.571	19.884	7.019	0.193	0.003221	17.729
8	10	10.944	2.900	6.800	15.212	33.369	2.899	0.779	0.003598	17.512
9	10	6.615	0.900	5.500	5.800	20.723	3.120	1.010	0.005110	17.394
10	6	6.078	1.400	6.800	8.433	24.145	17.374	0.247	0.006424	17.565
11	15	13.797	3.100	8.100	14.126	34.712	3.637	0.982	0.006656	17.429
12	11	8.127	1.100	7.700	8.527	24.279	7.300	0.830	0.009025	17.677
13	7	9.709	2.700	7.500	7.530	35.250	5.750	0.460	0.009389	17.707
14	16	11.959	3.200	8.200	9.610	28.809	3.000	1.790	0.010130	17.439
15	21	10.841	2.400	6.300	4.170	23.069	7.996	0.480	0.010744	17.364
16	5	6.788	1.000	9.800	13.386	30.024	17.061	0.483	0.012015	17.607
17	9	8.940	0.300	10.100	13.300	29.783	12.400	0.738	0.013203	17.621
18	6	9.229	1.100	11.400	16.240	37.408	10.400	0.808	0.015692	17.573
19	8	13.178	2.700	10.800	12.930	45.601	2.721	1.800	0.017212	17.436
20	16	10.490	3.000	9.300	7.540	25.130	8.036	1.278	0.018769	17.457

Group 2

	N	R_p (cm)	R_v (cm)	R_o (mm)	L_p (cm)	R_i (mm)	A (cm)	f $(1/s)$	k_c	μ_{ave} $(Pa{\cdot}s)$
1	14	6.464	1.616	3.650	18.852	16.726	1.862	0.745	0.000447	17.536
2	19	8.982	2.246	3.850	19.324	19.953	1.550	0.739	0.000513	17.519
3	9	6.899	1.725	5.000	15.690	22.266	2.728	0.742	0.001392	17.491
4	18	6.934	1.733	4.700	11.100	15.824	2.186	1.501	0.001602	17.595
5	18	7.130	1.533	5.350	15.209	16.412	3.800	1.190	0.001738	17.556
6	8	13.772	3.443	4.900	5.293	47.147	2.296	0.182	0.003809	17.592
7	7	6.620	1.655	7.500	15.048	24.228	1.500	3.800	0.004819	17.577
8	24	7.967	1.992	8.400	21.342	15.745	14.851	1.311	0.004956	17.384
11	16	15.051	3.763	8.600	20.384	36.434	2.438	1.546	0.005302	17.636
9	5	9.074	2.268	6.700	9.173	39.290	1.300	1.171	0.005514	17.689
10	16	10.561	2.640	8.300	17.673	25.563	5.500	1.280	0.005675	17.473
12	14	7.017	1.754	5.800	4.217	18.157	9.756	0.477	0.007864	17.635
13	10	11.054	2.764	10.000	20.409	33.847	4.987	1.373	0.008294	17.656
14	13	9.321	2.330	10.100	18.026	25.031	13.999	0.941	0.009971	17.501
15	6	13.614	3.404	10.900	20.050	53.815	5.900	0.600	0.011072	17.591
16	4	6.809	1.702	9.400	12.327	32.962	14.482	0.420	0.011634	17.554
17	11	8.973	2.243	10.500	16.673	26.197	7.700	1.735	0.011912	17.587
18	14	12.311	3.078	11.700	17.543	31.857	13.706	0.918	0.015810	17.539
19	16	15.954	3.988	8.300	5.017	38.618	3.200	0.970	0.020166	17.428
20	7	14.972	3.743	9.200	6.292	54.792	6.200	0.330	0.021107	17.617

Group 3

	N	R_p (cm)	R_v (cm)	R_o (mm)	L_p (cm)	R_i (mm)	A (cm)	f $(1/s)$	k_c	μ_{ave} $(Pa{\cdot}s)$
1	20	10.401	2.600	3.750	18.182	22.519	3.916	0.480	0.001675	11.921
2	17	7.537	1.884	4.950	11.234	17.698	16.888	0.426	0.006497	11.756
3	15	6.908	1.727	5.800	18.024	17.271	9.522	1.275	0.006510	11.758
4	10	8.407	2.102	6.150	13.679	25.741	3.913	1.627	0.009874	11.900
5	8	11.181	3.600	8.400	23.236	37.424	10.454	0.723	0.014463	11.997
6	4	8.665	2.166	8.200	21.732	41.948	3.139	1.891	0.015735	11.635
7	5	12.718	3.180	8.150	20.480	55.071	1.977	1.668	0.015776	11.789
8	12	8.810	2.203	8.280	20.391	24.625	12.187	1.421	0.016662	11.778
9	7	10.574	2.644	7.800	16.646	38.698	4.933	1.219	0.017716	11.627
10	16	13.788	3.447	6.600	9.351	33.375	3.600	1.299	0.017816	11.908
11	19	6.980	1.170	5.450	7.751	15.786	12.924	0.923	0.012358	11.824
12	16	14.754	3.688	9.900	24.122	35.713	15.357	0.906	0.023638	11.851
13	8	12.761	3.190	9.400	20.173	43.685	10.567	0.738	0.023471	11.975
14	14	11.271	2.818	5.500	4.141	29.168	14.795	0.248	0.024495	11.703
15	9	12.377	3.094	8.600	13.711	39.947	4.854	1.543	0.028417	11.684
16	3	8.891	2.223	9.600	18.772	49.700	9.699	0.685	0.028337	11.759
17	5	14.577	3.894	9.590	14.911	62.821	5.821	0.707	0.035135	11.808
18	4	12.951	3.238	9.400	13.899	62.701	7.600	0.520	0.036393	11.708
19	16	13.436	3.859	7.000	4.024	32.175	5.333	1.127	0.049518	11.898
20	14	10.235	2.559	9.000	8.705	26.484	14.463	1.361	0.051937	11.635

Group 4

	N	R_p (cm)	R_v (cm)	R_o (mm)	L_p (cm)	R_i (mm)	A (cm)	f ($1/s$)	k_c	μ_{ave} ($Pa{\cdot}s$)
1	14	11.254	2.814	4.138	18.352	29.123	6.619	0.232	0.002292	11.810
2	16	7.389	1.847	3.660	11.544	17.885	4.399	0.644	0.002536	11.786
3	16	15.727	3.932	4.270	13.290	38.070	15.126	0.065	0.003471	11.818
4	18	11.303	2.826	5.150	18.785	25.796	13.458	0.281	0.004328	11.800
5	13	7.920	1.980	6.660	18.444	21.269	7.610	1.582	0.009533	11.800
6	14	12.963	3.241	7.300	19.463	33.544	5.829	1.073	0.011555	11.918
7	16	6.938	1.735	7.100	12.289	16.795	18.991	1.189	0.016426	12.019
8	21	9.658	2.415	7.800	16.308	20.407	17.767	1.180	0.017265	11.813
9	8	13.635	3.409	6.650	9.505	46.676	7.885	0.318	0.018620	11.755
10	7	9.935	2.484	7.600	10.948	36.357	15.400	0.388	0.022952	11.958
11	24	10.849	2.712	5.900	4.411	21.441	16.687	0.495	0.027864	11.778
12	5	13.720	3.430	9.800	19.854	59.408	5.996	0.820	0.028208	11.801
13	15	10.046	2.511	8.320	11.302	25.114	16.452	1.034	0.030800	11.738
14	4	12.714	3.179	8.900	12.910	61.553	3.428	0.995	0.032223	11.835
15	7	13.413	3.353	8.310	9.676	49.085	17.253	0.254	0.035134	11.819
16	3	11.201	2.800	7.900	8.138	62.613	19.798	0.119	0.037131	11.682
17	6	8.279	3.070	7.000	4.934	31.389	15.405	0.408	0.040043	11.933
18	13	14.611	3.653	10.020	13.288	39.238	8.829	1.361	0.044858	11.818
19	17	15.329	3.832	10.000	12.098	35.997	9.589	1.500	0.050008	11.734
20	16	14.484	2.621	8.520	7.150	35.612	5.055	1.770	0.051093	11.831

Group 5

	N	R_p (cm)	R_v (cm)	R_o (mm)	L_p (cm)	R_i (mm)	A (cm)	f ($1/s$)	k_c	μ_{ave} ($Pa{\cdot}s$)
1	13	6.357	1.589	2.180	19.324	17.072	1.550	1.663	0.002695	5.498
2	20	12.557	3.139	2.350	18.852	27.188	1.862	0.710	0.003667	5.381
3	23	8.769	2.192	2.850	20.409	17.704	4.987	1.066	0.005634	5.522
4	16	6.318	1.580	1.900	4.217	15.294	9.756	0.217	0.008135	5.508
5	20	15.502	3.876	2.000	5.017	33.563	9.800	0.054	0.008285	5.431
6	13	6.462	1.615	3.130	18.026	17.352	3.999	1.861	0.008648	5.475
7	20	6.971	1.743	3.230	20.050	15.093	5.900	1.869	0.008817	5.412
8	6	13.060	3.265	3.200	17.673	51.626	5.500	0.161	0.009210	5.522
9	7	12.555	3.139	3.800	20.384	45.946	2.438	0.767	0.013356	5.524
10	14	6.344	1.586	2.600	6.292	16.418	7.200	0.681	0.014855	5.385
11	22	15.340	3.835	3.200	11.100	31.666	2.186	1.104	0.015260	5.441
12	22	9.171	2.293	4.000	17.543	18.932	13.706	0.944	0.018305	5.501
13	23	7.712	1.928	3.400	9.173	15.570	10.300	1.140	0.021477	5.503
14	16	12.787	3.197	4.500	15.209	30.953	3.800	1.835	0.030628	5.464
15	9	13.431	3.358	5.100	15.048	43.349	3.500	1.517	0.046906	5.384
16	6	14.491	3.623	5.200	15.690	57.282	2.728	1.175	0.047270	5.401
17	12	12.948	3.237	5.400	16.673	36.192	7.700	1.142	0.048092	5.472
18	14	9.922	2.481	5.850	21.342	25.676	14.851	1.510	0.048491	5.441
19	5	13.577	3.394	4.000	5.293	58.792	2.296	0.579	0.059757	5.532
20	6	14.235	3.559	5.500	12.327	56.267	14.482	0.269	0.070002	5.435

Group 6

	N	R_p (cm)	R_v (cm)	R_o (mm)	L_p (cm)	R_i (mm)	A (cm)	f $(1/s)$	k_c	μ_{ave} $(Pa{\cdot}s)$
1	15	14.001	3.500	1.540	9.039	35.002	1.290	0.171	0.002103	5.428
2	4	7.067	1.767	2.900	21.914	34.211	15.627	0.099	0.005760	5.439
3	7	7.361	1.840	2.750	14.274	26.937	3.463	0.620	0.007697	5.398
4	22	7.818	1.955	3.500	22.957	16.140	12.400	0.979	0.009632	5.446
5	18	11.797	2.949	3.600	22.901	26.923	4.700	1.026	0.010782	5.395
6	14	6.046	1.512	2.900	11.370	15.646	4.910	1.492	0.011013	5.455
7	4	8.638	2.160	2.050	3.841	41.819	0.407	0.877	0.011240	5.504
8	16	14.687	3.672	2.600	5.595	35.551	2.726	0.375	0.016138	5.454
9	13	7.455	1.864	3.740	14.308	20.021	10.956	0.899	0.019566	5.373
10	19	15.619	3.905	4.240	17.063	34.695	7.856	0.600	0.023365	5.418
11	12	14.173	3.543	3.900	10.438	39.615	2.019	1.377	0.029194	5.454
12	21	9.998	2.499	4.100	7.590	21.124	9.100	1.255	0.047041	5.437
13	13	7.450	1.862	4.300	6.335	20.005	9.073	1.592	0.063291	5.491
14	7	10.314	2.579	5.530	12.763	37.746	4.772	1.859	0.069845	5.403
15	7	11.499	2.875	6.200	15.754	42.081	6.100	1.637	0.078795	5.426
16	32	14.693	3.673	4.600	6.092	25.149	11.017	1.022	0.081386	5.471
17	8	15.106	3.777	5.200	8.043	51.713	5.800	0.650	0.086270	5.535
18	6	8.599	2.150	5.100	7.862	33.989	5.500	1.563	0.089109	5.399
19	9	13.749	3.437	4.400	4.778	44.375	8.138	0.386	0.089750	5.494
20	5	6.844	1.711	5.500	9.038	29.637	18.847	0.743	0.095386	5.437

Group 7

	N	R_p (cm)	R_v (cm)	R_o (mm)	L_p (cm)	R_i (mm)	A (cm)	f $(1/s)$	k_c	μ_{ave} $(Pa{\cdot}s)$
1	14	7.781	0.900	1.350	22.794	20.656	1.889	1.388	0.010016	1.867
2	4	8.126	2.621	1.900	19.990	38.459	1.064	1.887	0.029442	1.922
3	15	8.089	1.735	1.900	22.841	20.401	6.828	1.220	0.032966	1.753
4	19	8.999	3.653	1.200	4.973	18.869	12.658	0.186	0.035790	1.795
5	20	7.341	3.832	1.800	14.614	14.001	8.112	1.599	0.034628	1.914
6	24	12.000	3.750	2.000	15.000	23.268	7.400	1.000	0.057713	1.763
7	22	12.754	3.409	1.500	5.961	26.202	10.709	0.219	0.056542	1.816
8	10	6.567	3.932	2.000	9.092	16.633	16.534	0.799	0.082271	1.861
9	7	11.219	2.826	1.600	5.129	41.036	9.306	0.133	0.088177	1.750
10	14	7.040	3.430	1.800	6.135	16.431	10.722	0.976	0.097511	1.798
11	8	9.455	2.511	3.000	24.903	32.229	7.174	1.582	0.094318	1.912
12	21	9.596	1.847	1.800	5.501	20.549	5.950	1.118	0.107795	1.804
13	8	11.972	3.070	3.000	22.263	40.913	10.952	0.655	0.108628	1.891
14	5	10.685	2.484	2.500	10.455	46.474	12.109	0.264	0.132907	1.896
15	24	15.121	2.712	2.800	13.577	30.366	10.569	1.104	0.168962	1.786
16	9	15.052	2.415	2.500	8.130	49.522	1.831	1.485	0.161187	1.938
17	5	9.358	1.980	2.900	13.276	40.905	11.621	0.563	0.166773	1.882
18	8	11.619	3.353	2.900	10.244	39.330	15.649	0.471	0.231146	1.835
19	5	7.842	2.800	2.800	7.303	32.758	15.567	0.612	0.289867	1.840
20	6	7.757	3.241	2.600	4.279	28.770	13.392	0.682	0.348678	1.930

Group 8

	N	R_p (cm)	R_v (cm)	R_o (mm)	L_p (cm)	R_i (mm)	A (cm)	f $(1/s)$	k_c	μ_{ave} $(Pa{\cdot}s)$
1	5	9.677	2.419	1.400	19.473	41.901	0.706	0.993	0.012799	1.882
2	17	13.894	3.473	1.000	6.358	32.627	1.889	0.206	0.012599	1.972
3	23	7.006	1.752	0.950	9.590	14.145	12.109	0.164	0.008544	1.846
4	7	7.518	1.880	1.500	23.609	27.515	5.950	0.377	0.015588	1.758
5	18	8.060	2.015	1.200	10.123	18.395	6.828	0.345	0.016193	1.851
6	16	8.057	2.014	1.600	13.082	19.502	7.400	0.640	0.027526	1.905
7	17	10.053	2.513	1.300	5.232	23.608	5.567	0.341	0.042648	1.805
8	16	11.518	2.879	2.400	28.920	27.880	16.534	0.510	0.047345	1.822
9	9	9.883	2.471	2.200	18.590	31.896	10.709	0.443	0.052875	1.870
10	4	8.374	2.093	2.100	14.240	40.539	1.831	1.416	0.061500	1.854
11	21	8.941	2.235	2.500	20.754	18.891	10.569	1.828	0.066624	1.900
12	4	6.867	1.717	2.300	16.674	33.243	12.658	0.401	0.069088	1.853
13	10	6.915	1.729	2.100	12.316	21.173	15.649	0.634	0.076068	1.808
14	18	8.290	2.072	2.300	13.085	18.918	9.306	1.787	0.096910	1.788
15	5	13.719	3.430	2.900	24.253	59.406	5.112	0.642	0.099946	1.820
16	18	13.819	3.455	2.200	7.937	31.538	10.952	0.432	0.118945	1.899
17	10	11.309	2.827	3.100	20.148	34.626	9.221	1.120	0.118913	1.969
18	6	12.419	3.105	3.100	17.765	49.092	5.722	0.909	0.137624	1.954
19	15	7.048	1.762	2.200	4.782	17.621	13.392	1.249	0.230964	1.791
20	8	10.845	2.711	2.900	6.305	37.125	7.174	1.116	0.356070	1.872

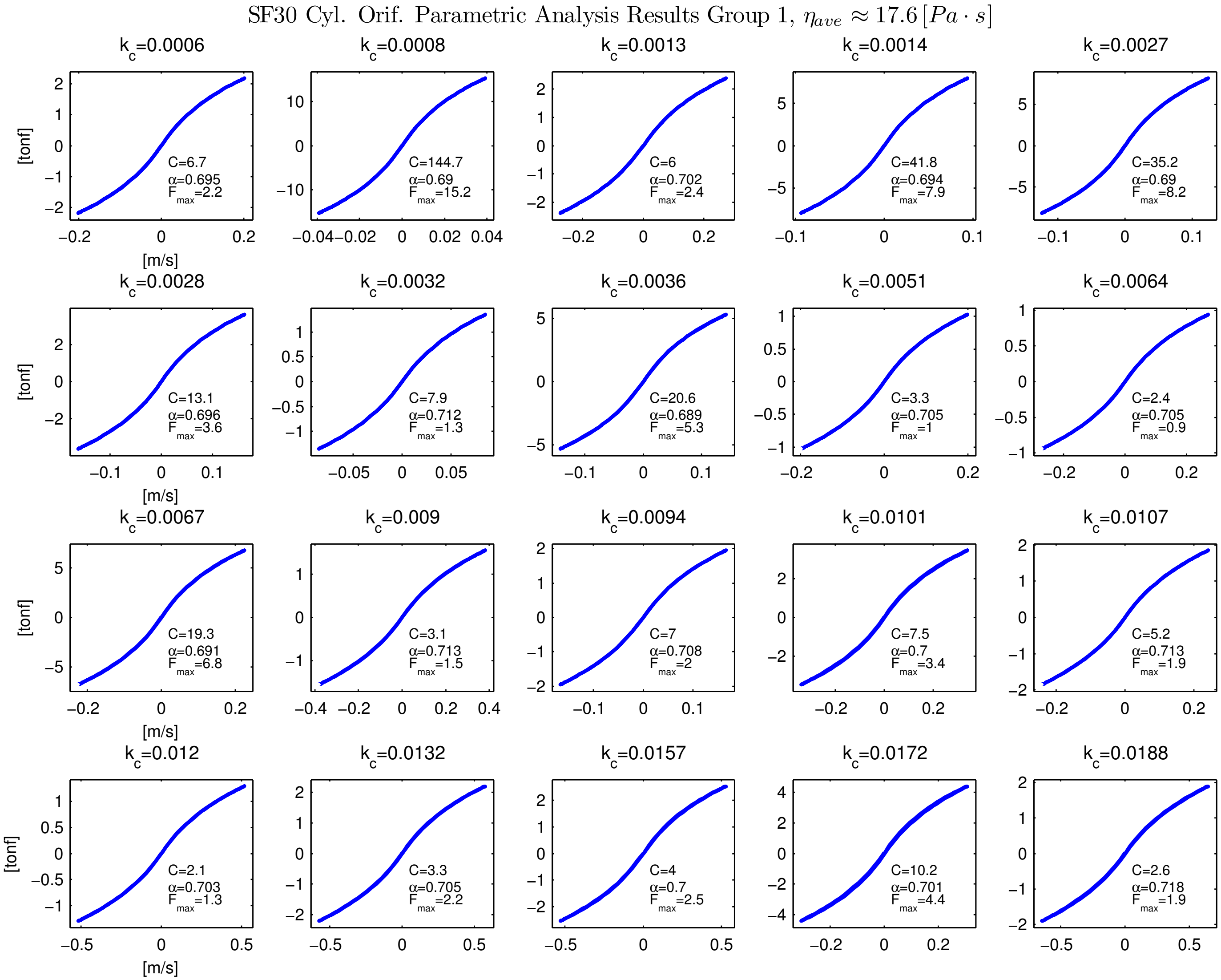
SF30 Cyl. Orif. Parametric Analysis Results Group 1, $\eta_{ave} \approx 17.6\,[Pa \cdot s]$
k_c=0.0006
C=6.7
α=0.695
F_{max}=2.2
k_c=0.0008
C=144.7
α=0.69
F_{max}=15.2
k_c=0.0013
C=6
α=0.702
F_{max}=2.4
k_c=0.0014
C=41.8
α=0.694
F_{max}=7.9
k_c=0.0027
C=35.2
α=0.69
F_{max}=8.2
k_c=0.0028
C=13.1
α=0.696
F_{max}=3.6
k_c=0.0032
C=7.9
α=0.712
F_{max}=1.3
k_c=0.0036
C=20.6
α=0.689
F_{max}=5.3
k_c=0.0051
C=3.3
α=0.705
F_{max}=1
k_c=0.0064
C=2.4
α=0.705
F_{max}=0.9
k_c=0.0067
C=19.3
α=0.691
F_{max}=6.8
k_c=0.009
C=3.1
α=0.713
F_{max}=1.5
k_c=0.0094
C=7
α=0.708
F_{max}=2
k_c=0.0101
C=7.5
α=0.7
F_{max}=3.4
k_c=0.0107
C=5.2
α=0.713
F_{max}=1.9
k_c=0.012
C=2.1
α=0.703
F_{max}=1.3
k_c=0.0132
C=3.3
α=0.705
F_{max}=2.2
k_c=0.0157
C=4
α=0.7
F_{max}=2.5
k_c=0.0172
C=10.2
α=0.701
F_{max}=4.4
k_c=0.0188
C=2.6
α=0.718
F_{max}=1.9
[tonf]
[m/s]

SF30 Cyl. Orif. Parametric Analysis Results Group 2, $\eta_{ave} \approx 17.6\,[Pa \cdot s]$

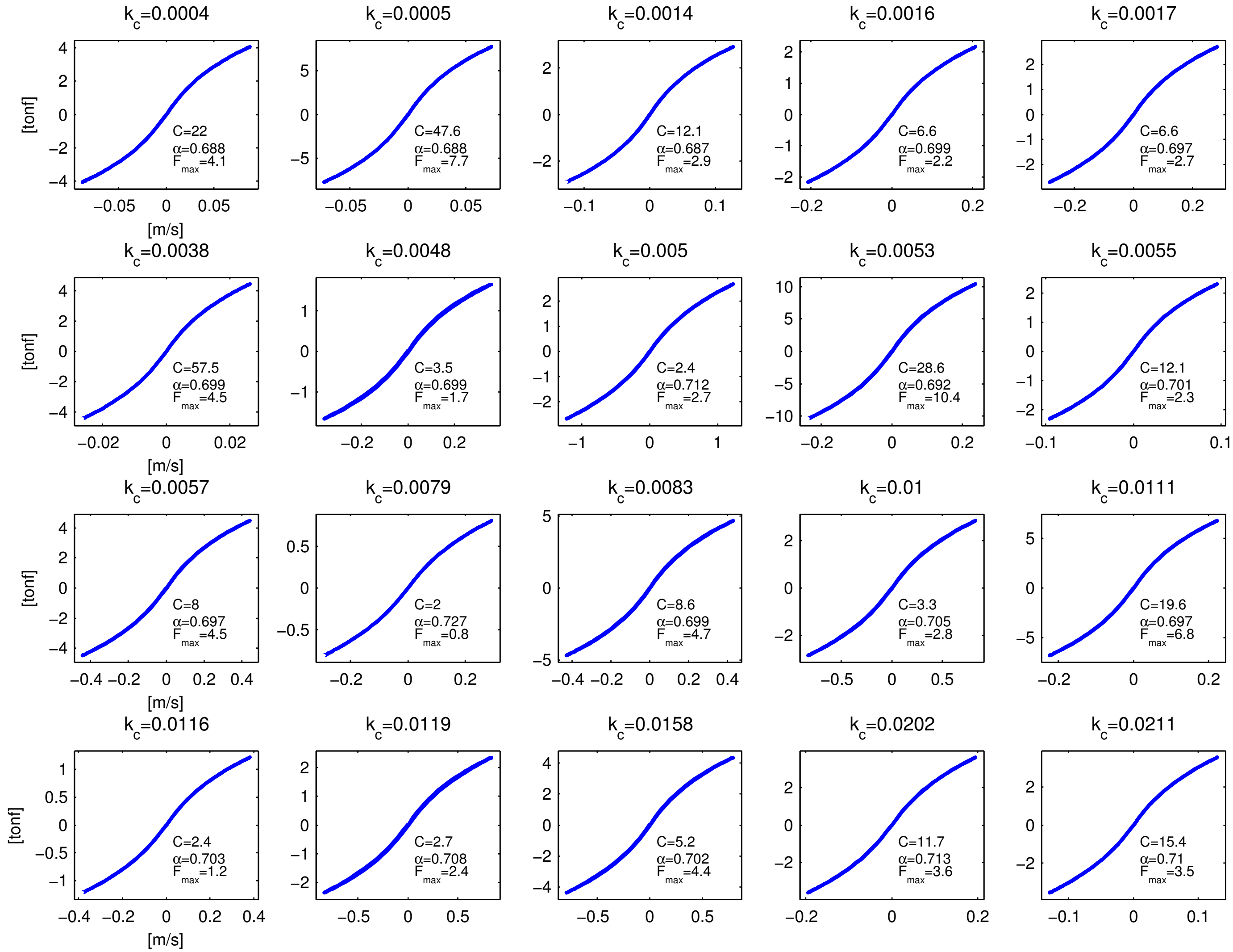

SF30 Cyl. Orif. Parametric Analysis Results Group 3, $\eta_{ave} \approx 11.8\,[Pa \cdot s]$

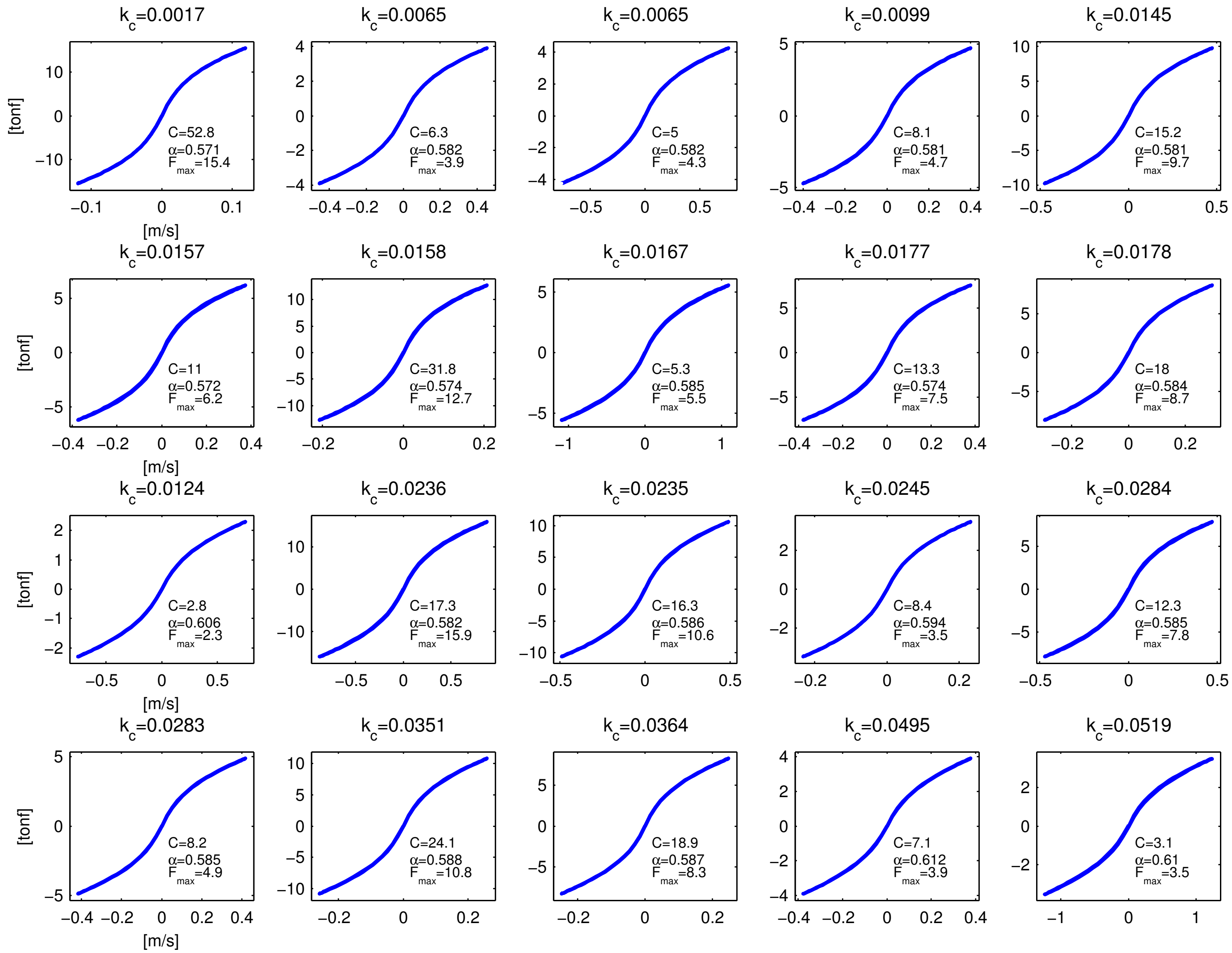

SF30 Cyl. Orif. Parametric Analysis Results Group 4, $\eta_{ave} \approx 11.8\,[Pa \cdot s]$

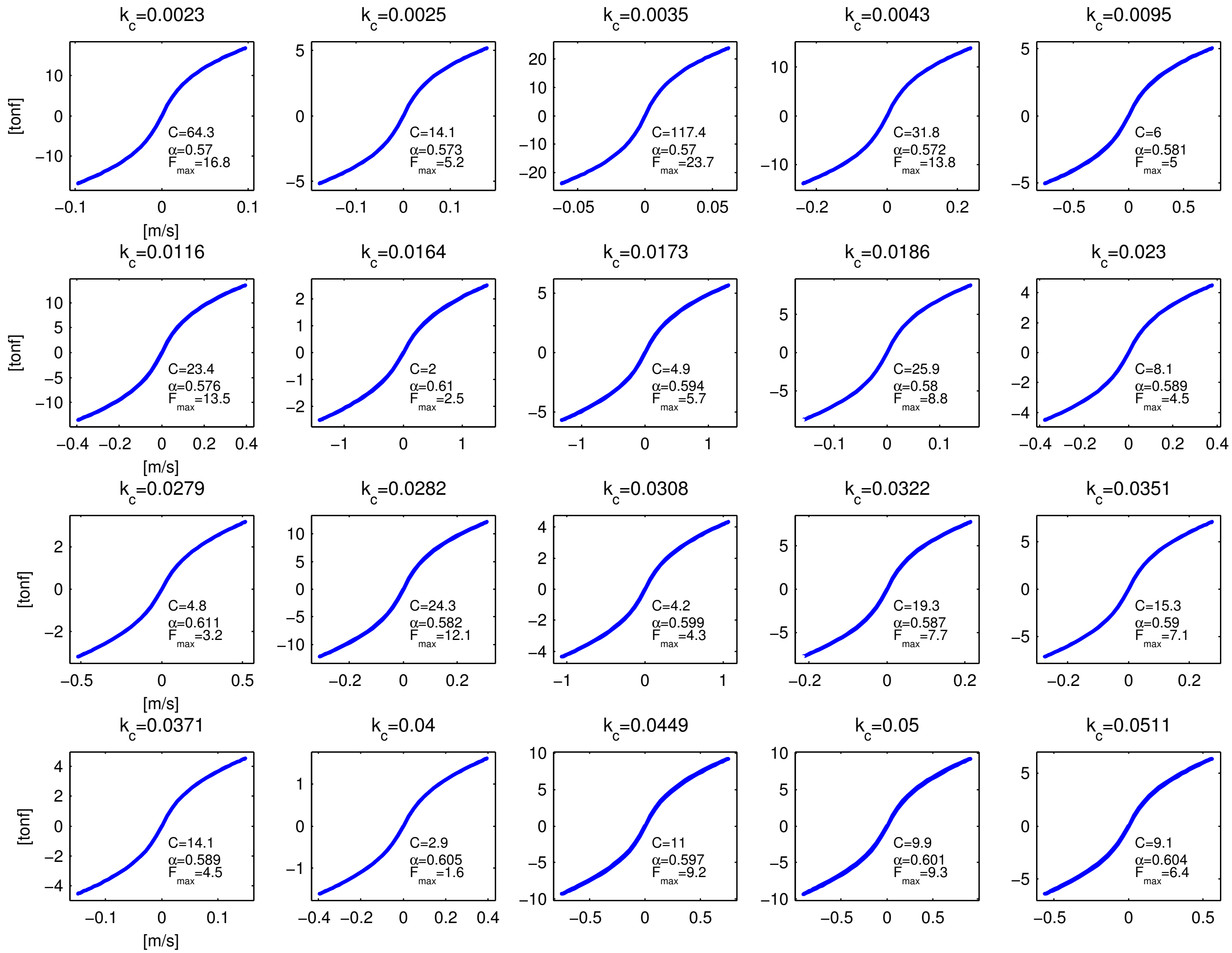

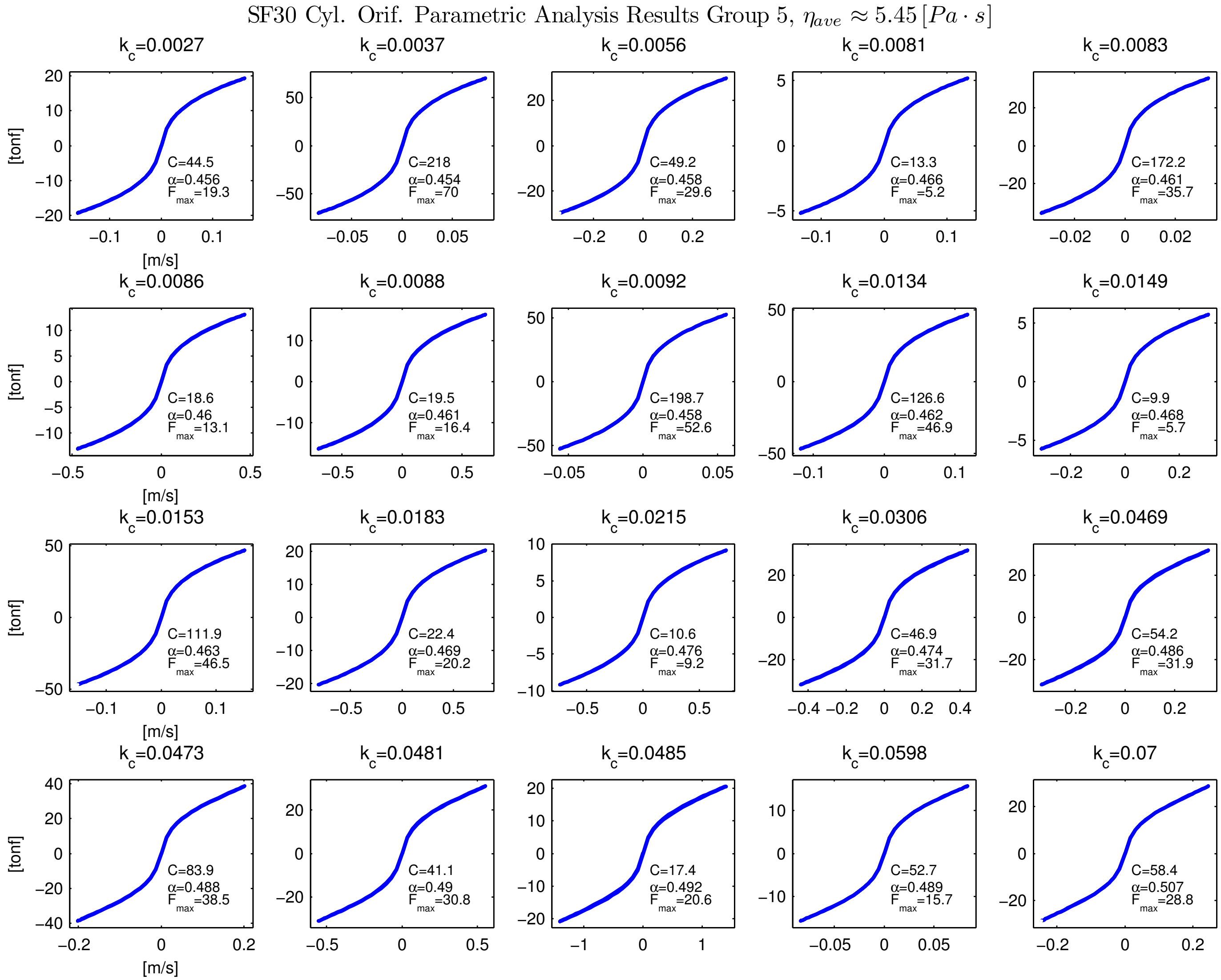
SF30 Cyl. Orif. Parametric Analysis Results Group 5, $\eta_{ave} \approx 5.45\,[Pa \cdot s]$
k_c=0.0027
C=44.5
α=0.456
F_max=19.3
k_c=0.0037
C=218
α=0.454
F_max=70
k_c=0.0056
C=49.2
α=0.458
F_max=29.6
k_c=0.0081
C=13.3
α=0.466
F_max=5.2
k_c=0.0083
C=172.2
α=0.461
F_max=35.7
k_c=0.0086
C=18.6
α=0.46
F_max=13.1
k_c=0.0088
C=19.5
α=0.461
F_max=16.4
k_c=0.0092
C=198.7
α=0.458
F_max=52.6
k_c=0.0134
C=126.6
α=0.462
F_max=46.9
k_c=0.0149
C=9.9
α=0.468
F_max=5.7
k_c=0.0153
C=111.9
α=0.463
F_max=46.5
k_c=0.0183
C=22.4
α=0.469
F_max=20.2
k_c=0.0215
C=10.6
α=0.476
F_max=9.2
k_c=0.0306
C=46.9
α=0.474
F_max=31.7
k_c=0.0469
C=54.2
α=0.486
F_max=31.9
k_c=0.0473
C=83.9
α=0.488
F_max=38.5
k_c=0.0481
C=41.1
α=0.49
F_max=30.8
k_c=0.0485
C=17.4
α=0.492
F_max=20.6
k_c=0.0598
C=52.7
α=0.489
F_max=15.7
k_c=0.07
C=58.4
α=0.507
F_max=28.8
[tonf]
[m/s]

SF30 Cyl. Orif. Parametric Analysis Results Group 6, $\eta_{ave} \approx 5.45\,[Pa \cdot s]$

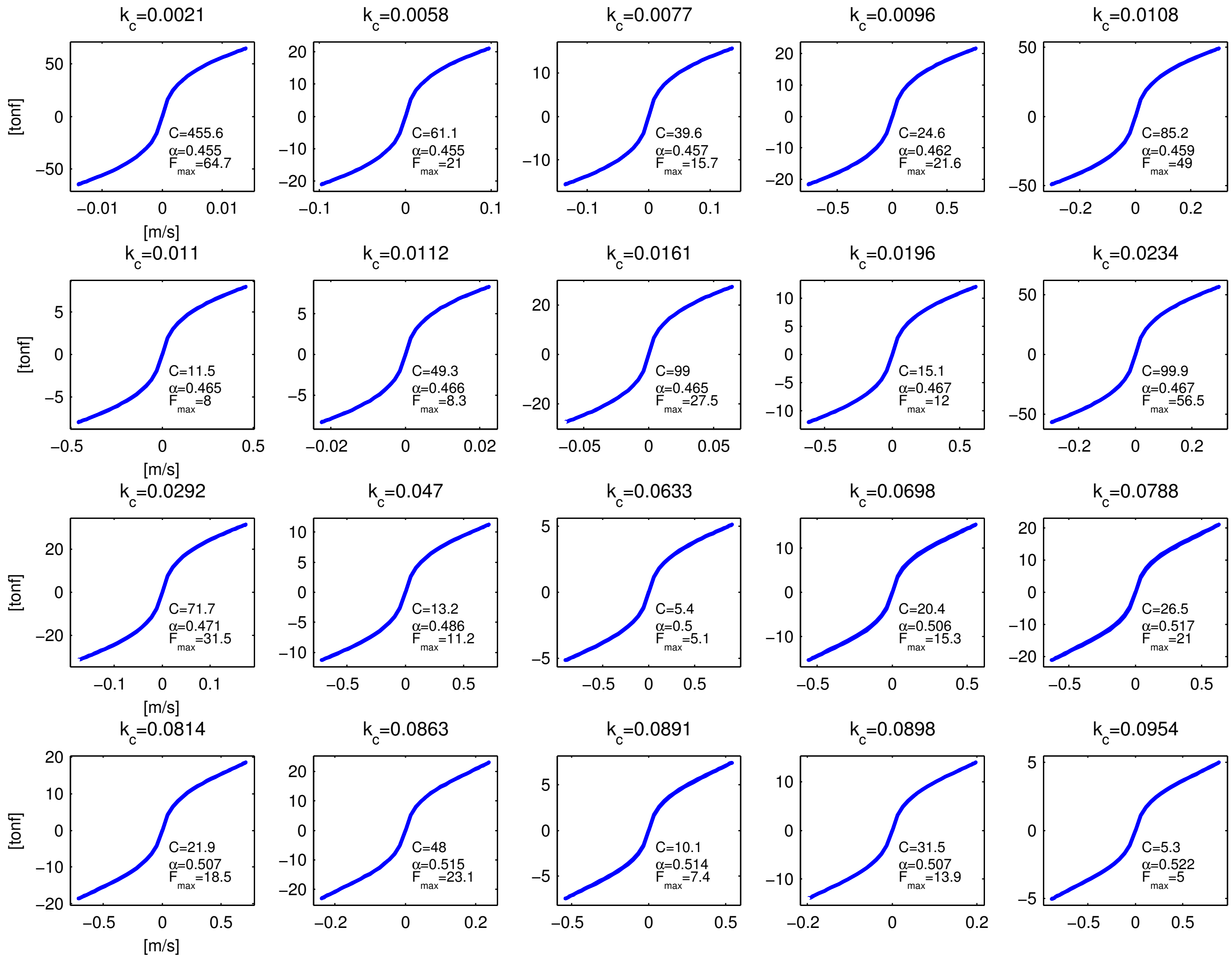

SF30 Cyl. Orif. Parametric Analysis Results Group 7, $\eta_{ave} \approx 1.85\,[Pa \cdot s]$

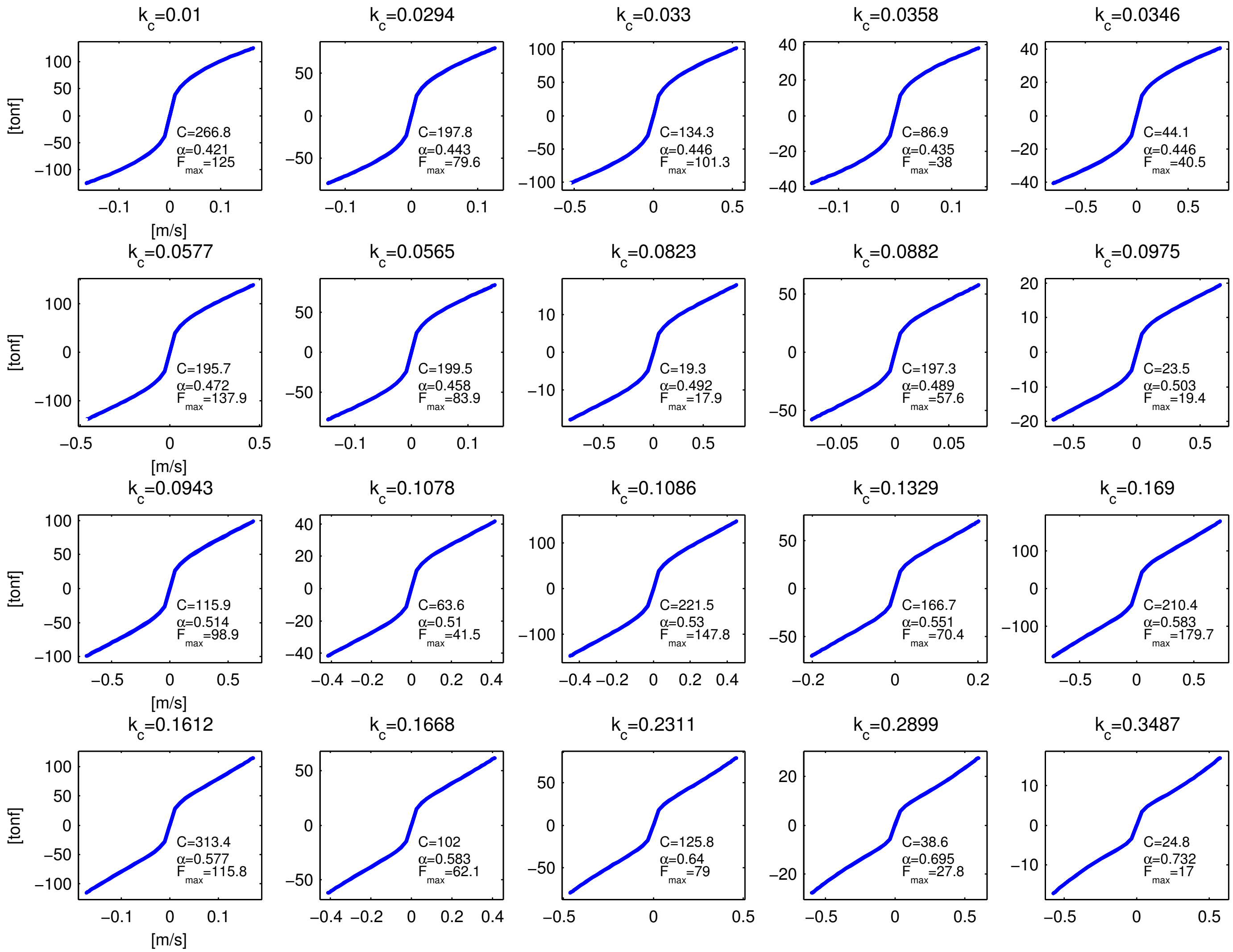

SF30 Cyl. Orif. Parametric Analysis Results Group 8, $\eta_{ave} \approx 1.85\,[Pa \cdot s]$

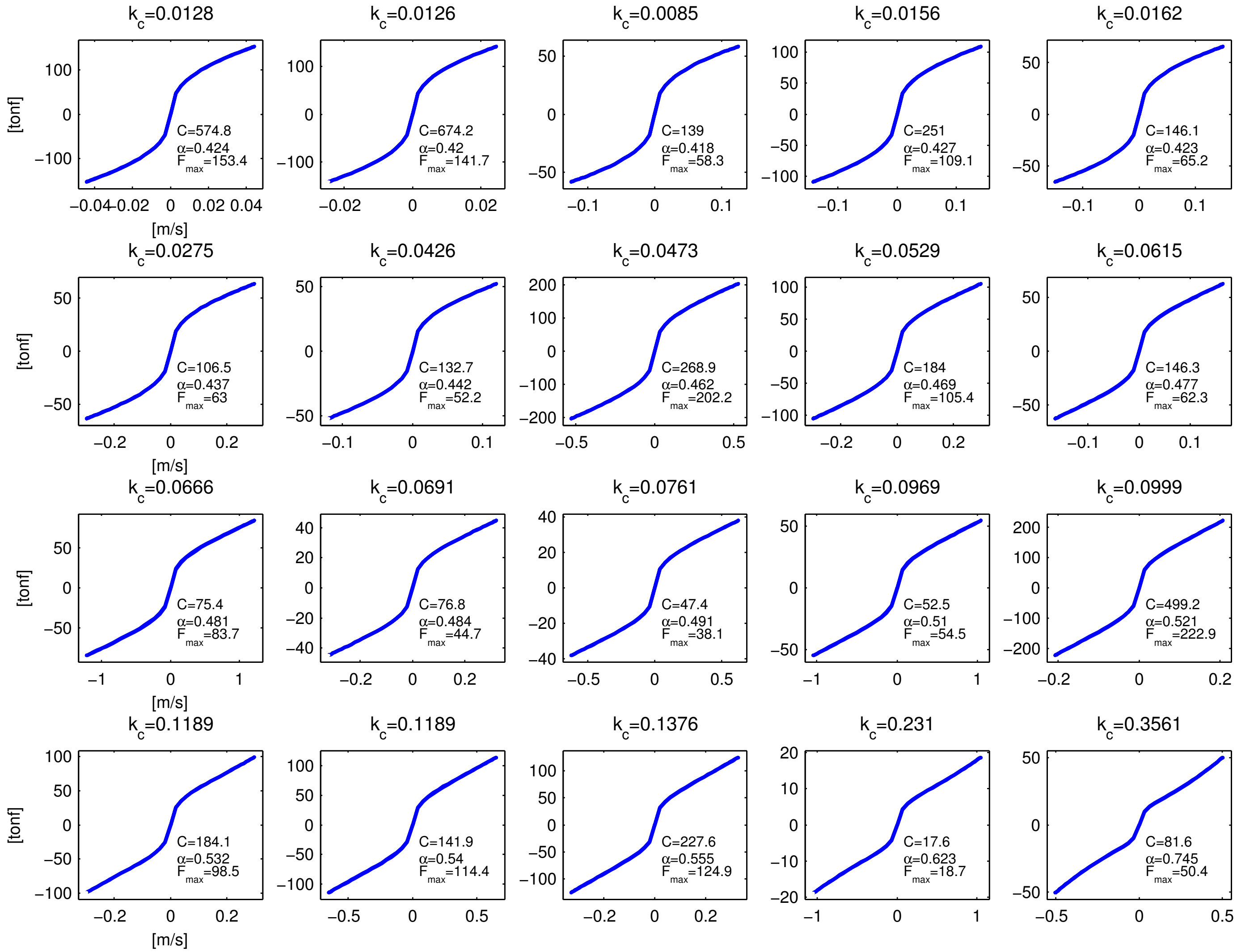

APPENDIX D: MESHES AND SIMULATION RESULTS EXAMPLES

This appendix includes model images and post-process example plots of different simulation results that were not included in the body of the thesis for brevity.

First, aspects from the models that included only fluid dynamics (imposed flow models, no heat transfer) will be presented. In the case of the annular orifice configuration, solved in two dimensional cylindrical coordinates, the fluid domain was discretized entirely with triangular elements, as exemplified in Figure D-1. Naturally, the mesh was much finer near the gap, were the steepest velocity gradients develop.

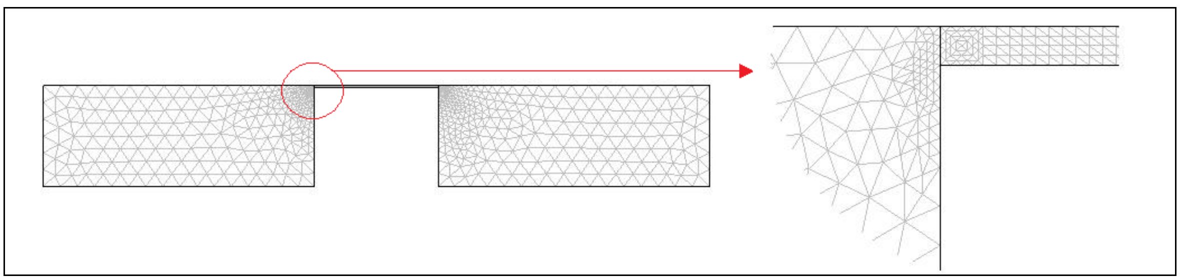

Figure D-1: This particular mesh corresponds to Design 3 and consists of 3103 triangular elements. The left figure zooms into the gap zone, were the mesh becomes much finer. (Comsol)

Figure D-2 shows an example of the resulting velocity field for this type of model. Specifically, it corresponds to the time instant of maximum piston velocity for an input of A = 12.4 *cm* and f = 0.21 *Hz,* as in Test 3-1. Recalling, the fluid used in this test was SF30 and the geometry that of Design 3. For this type of geometry, the fluid velocities in most of the domain are very low, except near and inside the gap. The maximum velocity, approximately 8.3 *m/s*, develops halfway through the gap width. Near this zone, variations in the velocity profile are mild, as seen in Figure D-3. In contrast, steep velocity gradients develop near the gap walls, causing the fluid to thin and originating the non linearity of the damper´s force-velocity relationship.

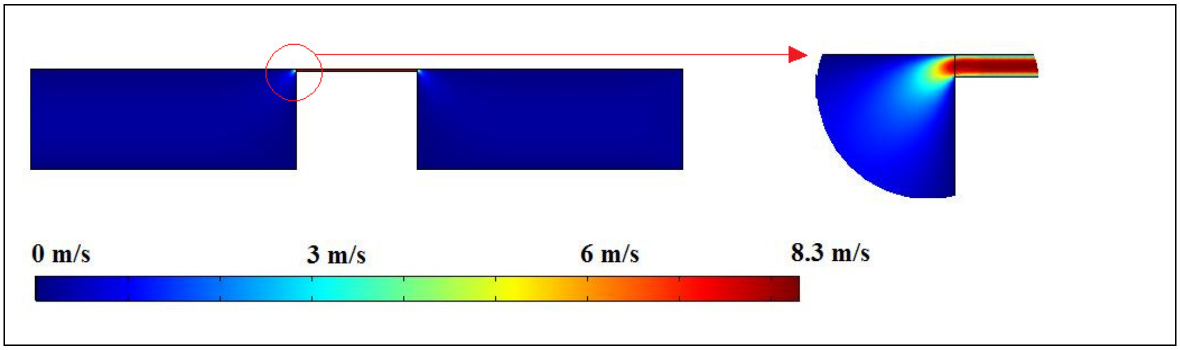

Figure D-2: Velocity field at the instant of maximum piston velocity of Test 3-1.

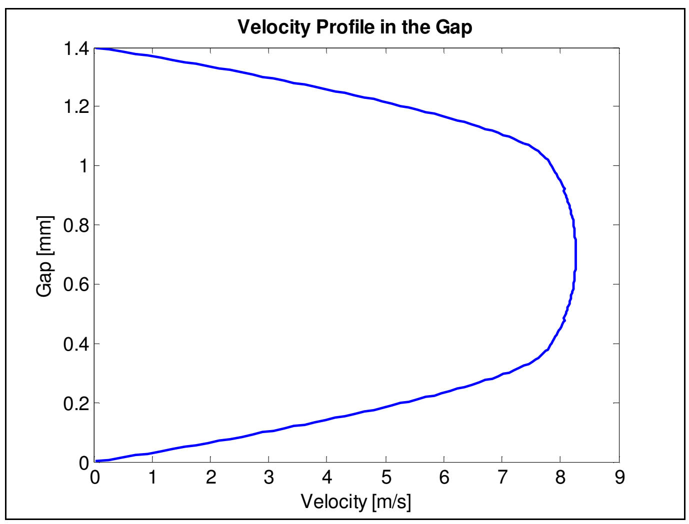

Figure D-3: Velocity profile inside the gap at the piston's mid-length at the instant of maximum piston velocity of Test 3-1.

Figure D-4 presents another interesting result, the pressure distribution inside the fluid domain at the same instant as the previous velocity field. This figure confirms, as was assumed during the body of this thesis, that pressure indeed remains constant throughout each chamber and that the pressure drop is linear and concentrated in the gap's length.

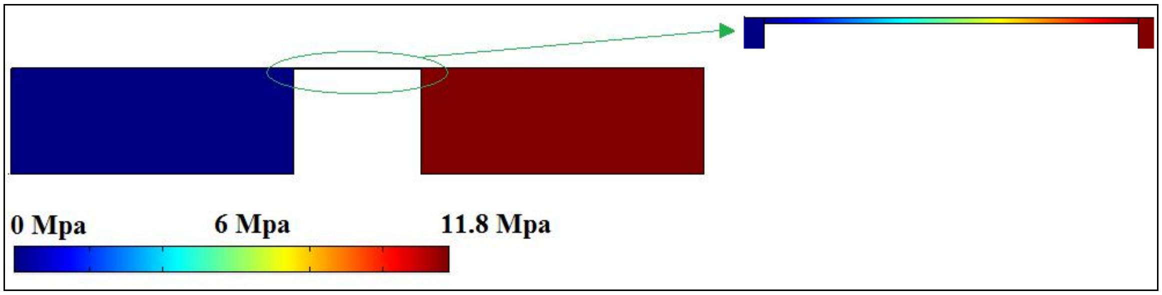

Figure D-4: Pressure field at the instant of maximum piston velocity of Test 3-1.

The configuration combining cylindrical and annular orifices (Design 1), in comparison, was solved on a three dimensional domain since axial symmetry is lost in this configuration. However, symmetry was taken advantage by modeling only a portion of the complete cylinder, as illustrated in Figure D-5. In this case, the mesh (Figure D-6) consisted of 585,793 elements, mixing tetrahedral elements (in the chambers) and hexahedral elements (in the gap and orifice).

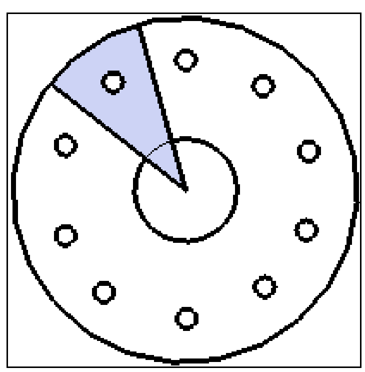

Figure D-5: A symmetric portion of the complete geometry was modeled to reduce computation time.

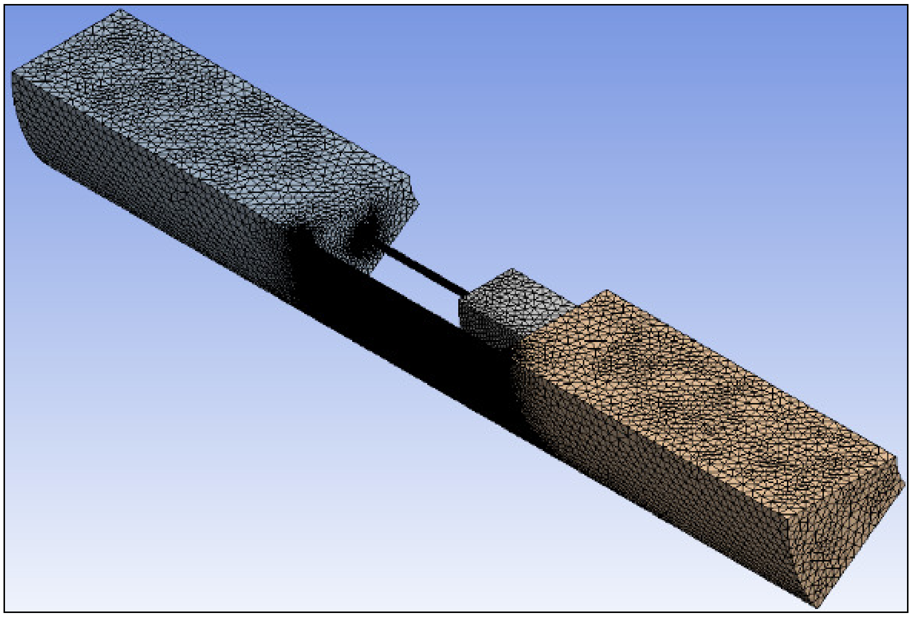

Figure D-6: Mesh corresponding to Design 1. (ANSYS)

Figure D-7 shows an example of the resulting velocity field for this type of configuration. Specifically, it corresponds to the time instant of maximum piston velocity for an input of A = 2 cm and f = 1 Hz, as in Test 1-2. Recalling, the fluid used in this test was SF1 and the geometry that of Design 1. Maximum velocities inside the orifice reached values as high as 45.6 m/s. The compressible flow formulation presented in this thesis is valid as long as Ma < 0.3; in this case:

$$Ma = |\mathbf{u}| \cdot \sqrt{\rho \cdot \beta} = 45.6 \frac{m}{s} \cdot \sqrt{970 \frac{kg}{m^3} \cdot 0.9341 \left[GPa^{-1} \right]} = 0.043 \tag{D.1}$$

which is far below the limit value.

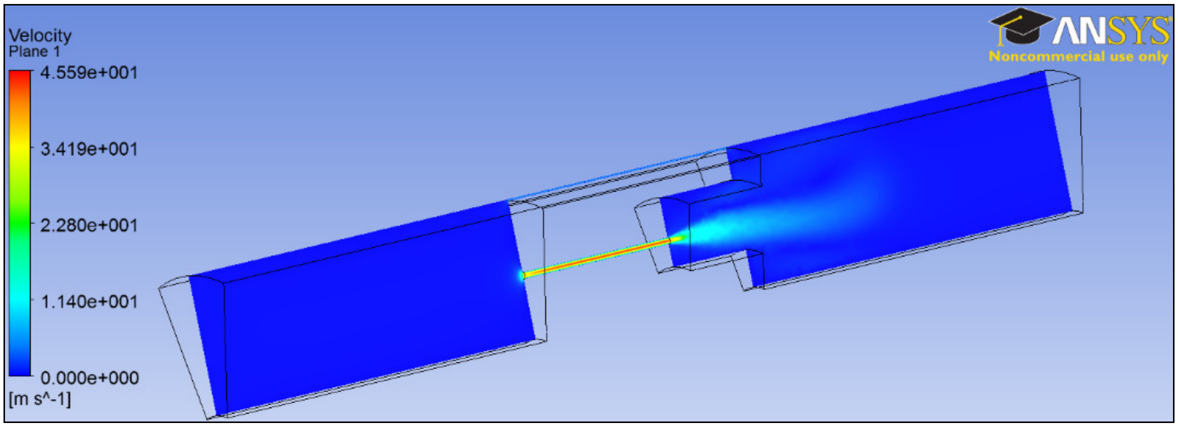

Figure D-7: Velocity field at the instant of maximum piston velocity of Test 1-2.

With respect to the fully multiphysics models, that is including heat transfer, the preference was to use meshes based on quadrilaterals. Since these models included the piston's movement, quadrilateral elements worked better at preserving the mesh quality and avoiding inverted elements as the mesh deformed. Figure D-8 shows a two dimensional mesh, consisting on approximately 4000 elements, used for the annular orifice configuration (specifically Design 3) and its deformation as the piston strokes.

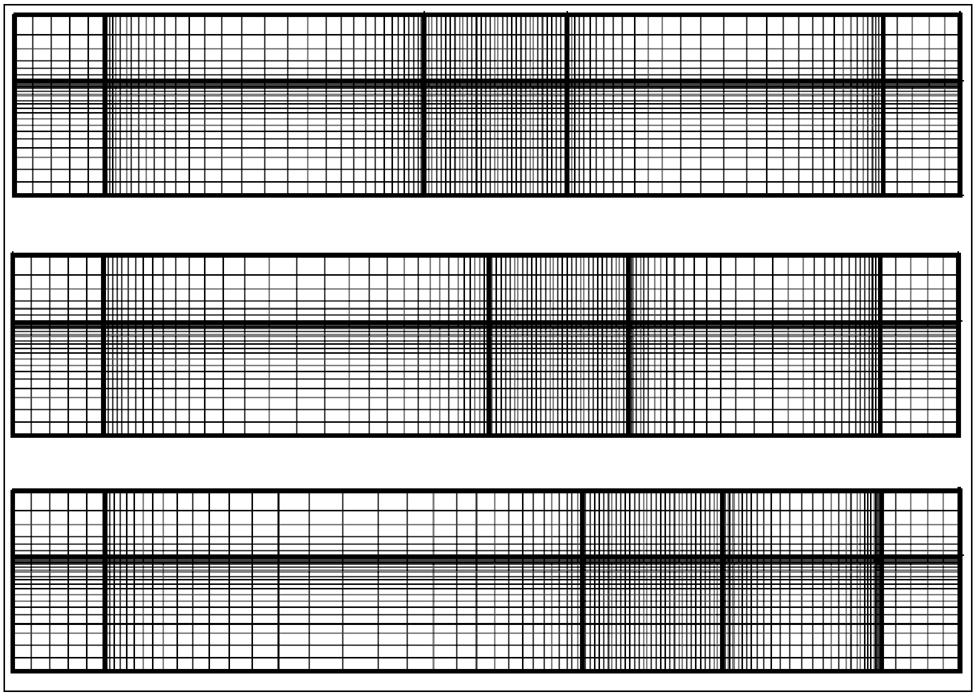

Figure D-8: Deforming mesh used for the multiphysics annular orifice models. In order to maintain the mesh quality, the gap mesh projects into the other domains. (Comsol)

Figure D-9 shows the resulting temperature field for Test 3-1 at different times. The temperature rise concentrates in the central zone (in the range of the piston's displacement), primarily due to the fluid's low thermal conductivity. The temperature in the cylindrical housing barely rises, indicating that for this type of excitation measuring its outer surface temperature is not a good indicator of the fluid's temperature, as was initially thought. In general, the tests were planned bearing in mind seismic applications (low number of cycles with high amplitudes). For an input emulating wind excitation, that is, over 2000 short amplitude cycles in which the test duration extends for a much longer time, the outer temperature would certainly be a better indicator of the internal temperature and the heat transfer coefficient between the cylinder's surface and the ambient would have to be selected more rigorously.

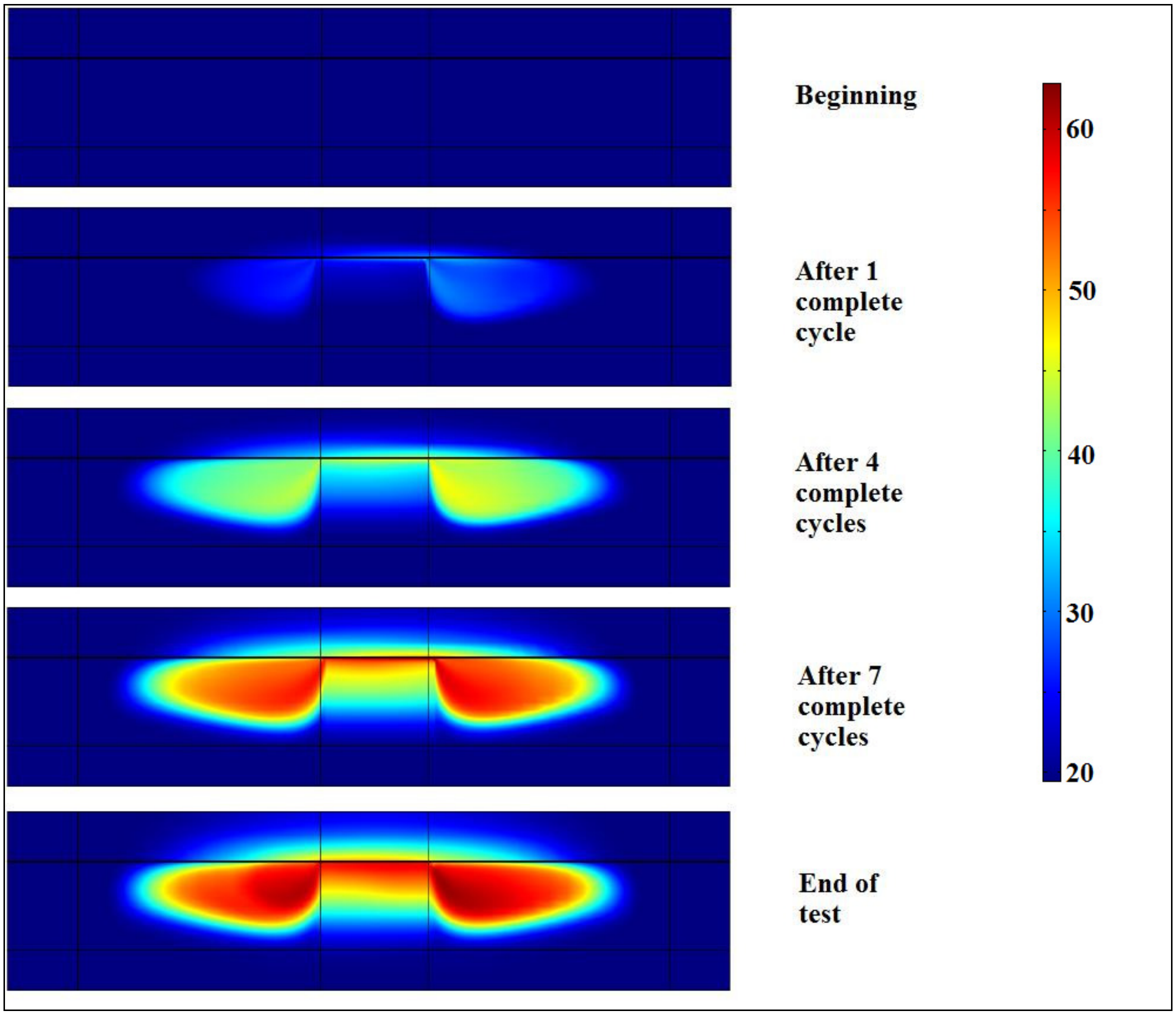

Figure D-9: Temperature fields at different times during Test 3-1.

Figure D-10 shows the mesh, consisting of 488,026 elements, used to discretize the geometry of Design 1. Again, the mesh was based on quadrilateral elements, except in the piston which, naturally, does not deform. A comparison of Figure D-10 and Figure D-8 illustrates the different approaches used by Comsol and ANSYS to model the interface between the silicone fluid and the inner surface of the cylindrical housing. In the case of Figure D-10, the mesh at the solid and fluid sides does not match; the CFX Solver calculates the temperature based on heat flux conservation through that boundary (Ansys Inc., 2009). The cylinder's mesh is therefore static during the whole simulation. On the contrary, Comsol is able to handle deforming meshes both in fluid and solid domains. Therefore, the cylindrical housing's mesh is able to accommodate the piston's movement maintaining always a 1:1 mesh connection at the interface.

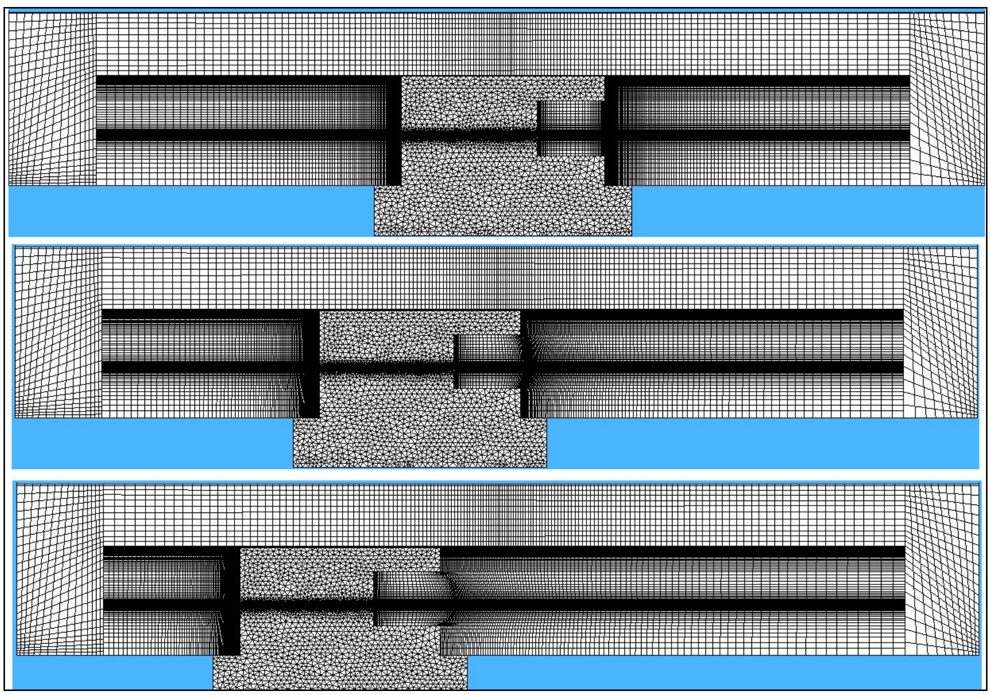

Figure D-10: Deforming mesh used for the multiphysics model of Test 1-1. Again, in order to maintain the mesh quality, the gap and orifice's mesh project into the other domains. (ANSYS)

Contrasting with the imposed flow model of this geometry (Design 1), symmetry was further exploited in the multiphysics case: a portion containing only one half of one orifice was used to reduce calculation time, as depicted in Figure D-11.

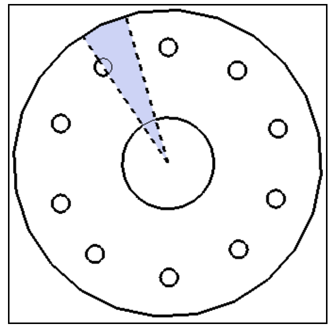

Figure D-11: A small symmetric portion of the geometry was used for the multiphysics model of Test 1-1 to decrease the number of elements and speed up calculations.

Figure D-12 shows the resulting temperature field for Test 1-1 at different times. The temperature rise distributed almost uniformly throughout the fluid domain, unlike the annular orifice configuration. Since this damper configuration was tested far below the velocity it was designed for (due to pump limitations), the temperature rise was very slight, with an average of approximately 5 °C after 6 cycles.

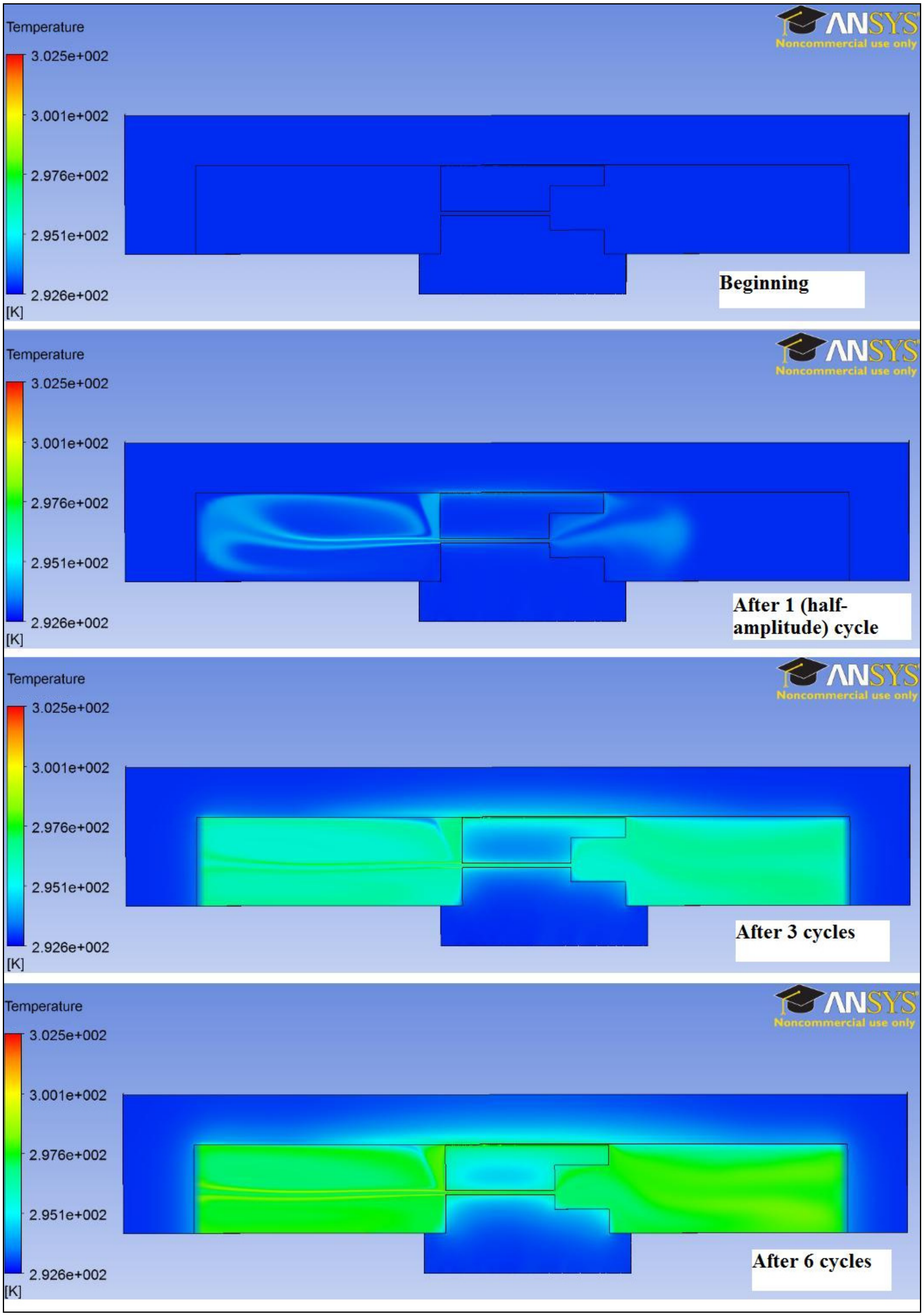

Figure D-12: Temperature fields at different times during Test 1-1.

APPENDIX E: EXPERIMENTAL RESULTS AND DATA PROCESSING

During the months of October, November and December of 2010, three testing sessions took place at the Structural and Geotechnical Engineering Department's Laboratory. In each session one of the designs detailed in the body of this thesis was tested in corresponding order, that is, Session 1 corresponded to Design 1, Session 2 to Design 2 and so on. The finished prototype may be seen in Figure E-1 and the experimental setting in Figure E-2.

Figure E-1: Prototype ready to be tested.

Measured quantities during the tests were the actuator force and displacement, pressure in the damper's two chambers, fluid temperature at one point (near one of the cylinder caps, at the extreme of a chamber) and the temperature at the housing cylinder's outer surface. Figure E-3 shows the instrumentation connected to the damper and the data acquisition system.

Figure E-2: Experimental setting at the lab.

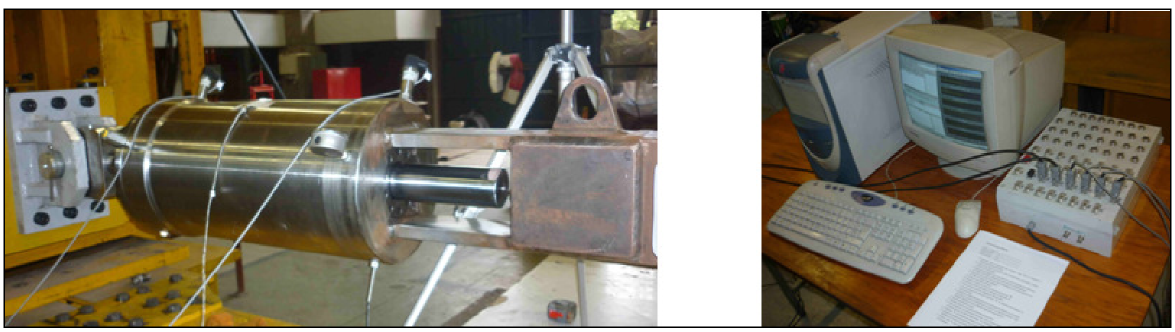

Figure E-3: Damper instrumentation and data acquisition system.

The complete list of performed tests may be seen in Table E-1 through Table E-3. The tests referred to during the body of this thesis (Test 1-1, 1-2, 2-1, etc.) are labeled accordingly in these tables. Tests with a $\pm 15\ cm$ note in the observations column were performed with the piston oscillating with respect to a point that was offset from the cylinder's mid-length.

Table E-1: Tests performed on Design 1.

Test ID	Amplitude (cm)	Frecuency (Hz)	MaxVel. (cm/s)	Completed Cycles	Date	Obs.
1a	10.0	0.10	6.28	7	23-10-10 10:08	-
2b	2.0	0.50	6.28	7	23-10-10 11:47	-
3a	16.0	0.10	10.05	7	23-10-10 12:05	-
4a	1.25	1.50	11.78	7	23-10-10 13:34	-
5a	1.0	2.00	12.57	7	23-10-10 13:59	-
6a	1.5	1.50	14.14	7	23-10-10 14:31	-
7a	5.0	0.50	15.71	7	23-10-10 15:19	-
8a	1.4	2.00	17.59	7	23-10-10 18:05	-
10a	12.4	0.14	10.91	7	23-10-10 18:39	Test 1-1
9b	20.0	0.14	17.59	7	24-10-10 10:07	-
11a	2.0	1.00	12.57	7	24-10-10 10:52	Test 1-2
12a	2.3	1.00	14.45	7	24-10-10 10:58	-
13a	1.4	1.50	13.19	7	24-10-10 12:18	-
14a	1.4	1.25	11.00	7	24-10-10 12:23	-
15a	1.4	1.00	8.80	7	24-10-10 12:42	-
16a	1.4	0.50	4.40	7	24-10-10 12:48	-
18a	8.0	0.20	10.05	7	24-10-10 13:10	-
17a	3.6	0.60	13.57	7	24-10-10 13:37	-
19a	1.4	1.50	13.19	7	24-10-10 14:06	-
20a	1.4	1.25	11.00	7	24-10-10 14:08	-
21a	1.4	1.00	8.80	21	24-10-10 14:11	-

Table E-2: Tests performed on Design 2.

Test ID	Amplitude (cm)	Frecuency (Hz)	MaxVel. (cm/s)	Completed Cycles	Date	Obs.
17a	8.0	0.08	4.02	7	20-11-10 8:53	-
2a	16.0	0.10	10.05	7	20-11-10 9:26	-
11a	1.4	1.25	11.00	7	20-11-10 10:57	-
12a	1.4	1.00	8.80	7	20-11-10 10:59	-
13a	1.4	0.50	4.40	7	20-11-10 11:02	-
4a	5.0	0.50	15.71	7	20-11-10 11:31	-
14a	3.6	0.60	13.57	7	20-11-10 12:10	-
18a	3.6	0.60	13.57	7	20-11-10 13:34	(+15 cm)
5a	1.4	2.00	17.59	7	20-11-10 14:16	-
8a	2.0	1.00	12.57	7	20-11-10 14:43	Test 2-2
9a	2.3	1.00	14.45	7	20-11-10 14:46	-
22a	1.4	1.00	8.80	7	20-11-10 15:13	-
3a	1.5	1.50	14.14	7	20-11-10 16:01	-
1a	10.0	0.10	6.28	7	20-11-10 16:43	-
16a	4.0	0.30	7.54	7	20-11-10 17:08	-
1b	10.0	0.10	6.28	7	20-11-10 17:14	-
20a	1.4	1.50	13.19	7	23-11-10 12:10	-
21b	1.4	1.25	11.00	7	23-11-10 12:15	-
7a	12.4	0.21	16.36	5	23-11-10 12:51	Test 2-1
23a	10.0	0.23	14.14	7	23-11-10 13:25	-
15a	6.0	0.40	15.08	7	23-11-10 13:57	-
24a	5.0	0.50	15.71	7	23-11-10 14:29	-
19b	2.0	1.00	12.57	7	23-11-10 14:35	-

Table E-3: Tests performed on Design 3.

Test ID	Amplitude (cm)	Frecuency (Hz)	MaxVel. (cm/s)	Completed Cycles	Date	Obs.
1a	8.0	0.08	4.02	5	04-12-10 12:38	-
2a	4.0	0.30	7.54	7	04-12-10 13:01	-
3b	1.4	1.00	8.80	7	04-12-10 13:14	-
4a	1.4	1.25	11.00	7	04-12-10 13:23	-
5a	1.4	1.50	13.19	7	04-12-10 13:32	-
6a	1.4	1.75	15.39	7	04-12-10 13:42	-
7a	1.4	2.00	17.59	7	04-12-10 14:00	-
8a	16.0	0.10	10.05	4	04-12-10 14:16	-
9a	3.6	0.60	13.57	7	04-12-10 15:25	-
10a	3.6	0.60	13.57	7	04-12-10 16:06	(-15 cm)
11a	6.0	0.40	15.08	7	04-12-10 16:34	-
12a	7.0	0.40	17.59	4	04-12-10 17:29	-
13a	5.0	0.50	15.71	7	04-12-10 18:10	-
14a	6.0	0.40	15.08	7	04-12-10 18:41	-
15a	10.0	0.225	14.14	5	04-12-10 19:46	-
16a	12.4	0.21	16.36	6	05-12-10 10:02	Test 3-1
17a	5.0	0.55	17.28	7	05-12-10 10:33	-
18a	5.0	0.50	15.71	7	05-12-10 11:06	Test 3-2
19a	2.0	1.00	12.57	7	05-12-10 12:10	-
20a	1.4	1.50	13.19	7	05-12-10 12:13	-
21a	1.4	1.25	11.00	7	05-12-10 12:15	-
22a	1.4	1.00	8.80	7	05-12-10 12:17	-
23a	16.0	0.14	14.07	2.5	05-12-10 13:23	-
24a	3.6	0.70	15.83	7	05-12-10 14:13	-
25a	3.6	0.60	13.57	7	05-12-10 14:16	-
26a	10.0	0.23	14.14	5	06-12-10 11:38	-
27a	4.0	0.30	7.54	7	06-12-10 11:43	-

.

In general, the electrical signals measured during the different tests had a noise component that was filtered out in order to obtain smoother results. The case of velocity, for instance, was particularly critical since it is calculated as the numerical derivative of the displacement. If the unprocessed displacement signal were used for this, the noise would be amplified and the resulting velocity incoherent. As a consequence, the displacement and pressure signals for the different tests were filtered as explained next. The force signal, in contrast, was used unprocessed since the signal to noise ratio was high.

The objective of filtering a signal is to eliminate undesired frequency content. In this case, a low-pass Butterworth filter was employed, which is characterized by a plateau in the passing band and decaying rapidly beyond the cutoff frequency. The gain for this kind of filter may be expressed as:

$$G^2(\omega) = \left|H(j\omega)\right|^2 = \frac{{G_0}^2}{1 + \left(\frac{\omega}{\omega_c}\right)^{2n}} \qquad \text{(E.1)}$$

where n is the filter order, ω_c the cutoff frequency and G_0 the gain at zero frequency. As an example, Figure E-4 displays the frequency response for a fifth order Butterworth filter with a cutoff frequency of $\omega = 2\left[rad/s\right]$.

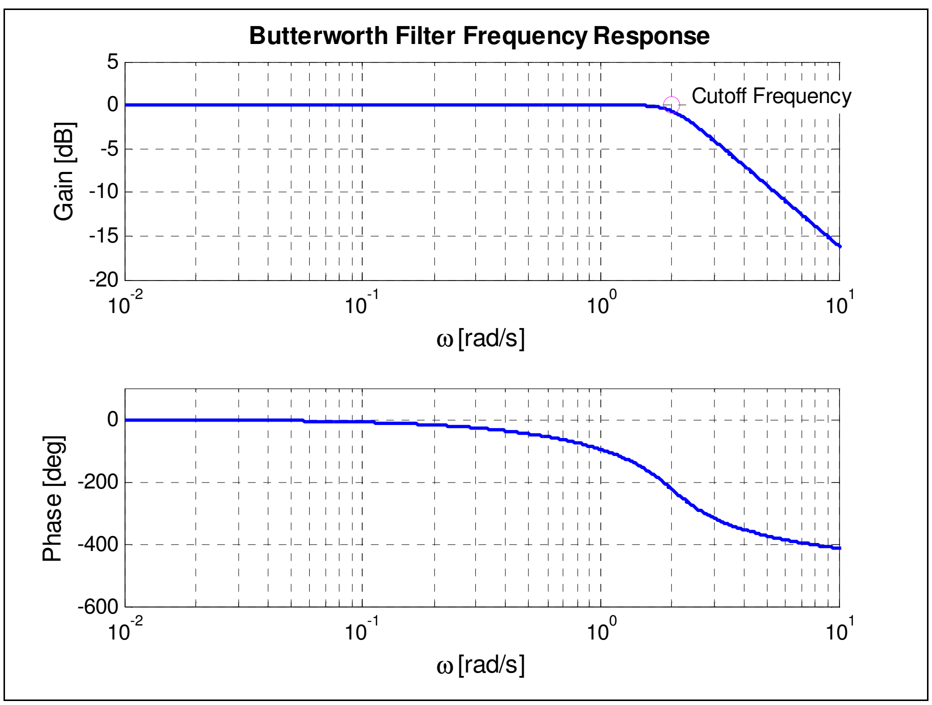

Figure E-4: Frequency response for a fifth order Butterworth filter with a cutoff frequency of $\omega = 2\left[rad/s\right]$.

Matlab includes a Butterworth filter through a function named `butter`. This function receives two parameters as input: *a*, the order of the filter and *b,* which allows to indicate the cutoff frequency and is defined as $b = f_{cutoff} / (0.5 f_s)$, where f_s is the signal sampling rate, in this case 100 *Hz*. Herein, a fifth order filter was employed in all cases and b was established as $b = Z \cdot f_{test} / 50$ where Z amplifies the frequency corresponding to the particular test, f_{test}, so the cutoff frequency is greater than it. It was observed that Z values between 2 and 3 worked well for the higher frequencies (1 to 2 *Hz*) and between 4 and 5 for the lower frequencies (0.08 to 0.7 *Hz*).

Another anomalous phenomenon in the raw experimental data that was corrected had to do with unwanted displacements of the damper cylinder. Ideally, the displacement of the dynamic actuator should be transmitted perfectly to the damper, without relative movement between them. Nevertheless, there was a slight clearance between the pin and the damper's clevis and also a perceptible movement of the supporting frame. This manifested as a plateau near the zones of zero force in the force-velocity and force-displacement curves. In other words, the actuator could move without resistance when changing its direction. Figure E-5, illustrates this phenomenon in one of the tests on Design 1, particularly Test 11a according to Table E-1. (The test referred to as 11a in this appendix is the same as the test referred to as 1-2 during the body of the thesis.) The red circles show the plateaus where velocity increased without an increase in force, which would not be physically possible and is only explained by the unwanted displacements just described.

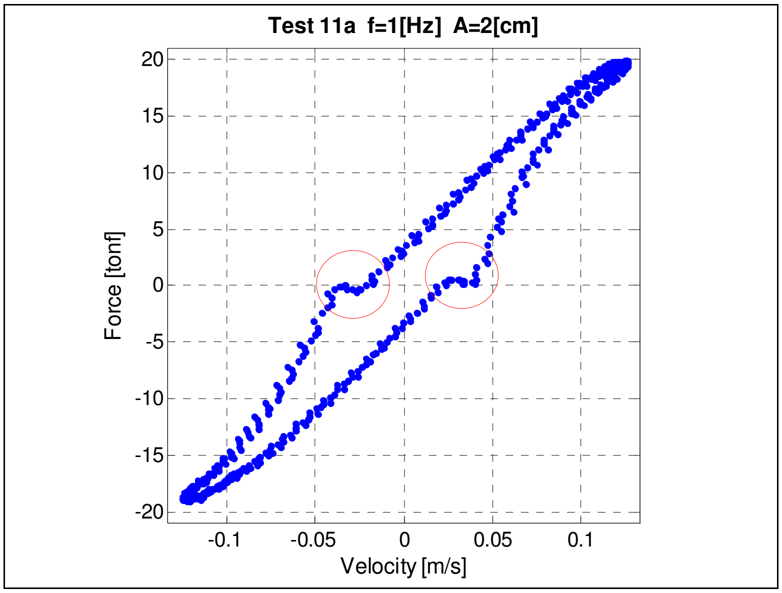

Figure E-5: Unprocessed force-velocity curve corresponding to Test 11a. The red circles indicate the plateau region caused by undesired relative movement between the damper and the dynamic actuator.

Intuitively, the first inclination to correct this problem *a posteriori* is to revise the displacement signal. However, since these are displacement controlled tests, the dynamic actuator executes the prescribed displacement independently of what occurs with the tested probe. Therefore, no evident problems are identifiable when examining the displacement history, as seen in Figure E-6. On the contrary, when examining the force history in the same figure, there is an unmistakable anomaly when the force changes its sign. It was decided to solve this by replacing the anomalous points with interporlated points using the previous and subsequent zones to the problematic area, eliminating the alluded plateaus. Considering that velocity is what determines the damper's output force, once all the clearance in the mentioned zones is adjusted, the damper's piston velocity is effectively the same as the actuator's velocity regardless of any previous unwanted displacement.

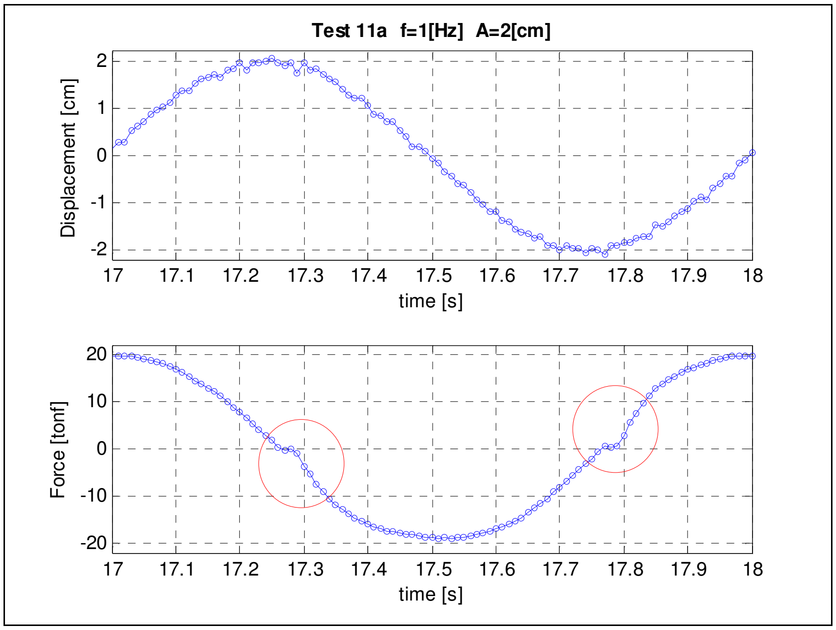

Figure E-6: Fragment of the displacement and force histories during Test 11a without processing. The red circles indicate the problematic zones.

Figure E-7 shows an example of how the original anomalous points (in red) where replaced with interpolated points for Test 11a. Naturally, the definitive solution for this problem would be to physically eliminate the clearance between the pin and clevis and, furthermore, directly measuring the piston's and the cylinder's displacement with two LVDT's and subtract them to determine the true displacement.

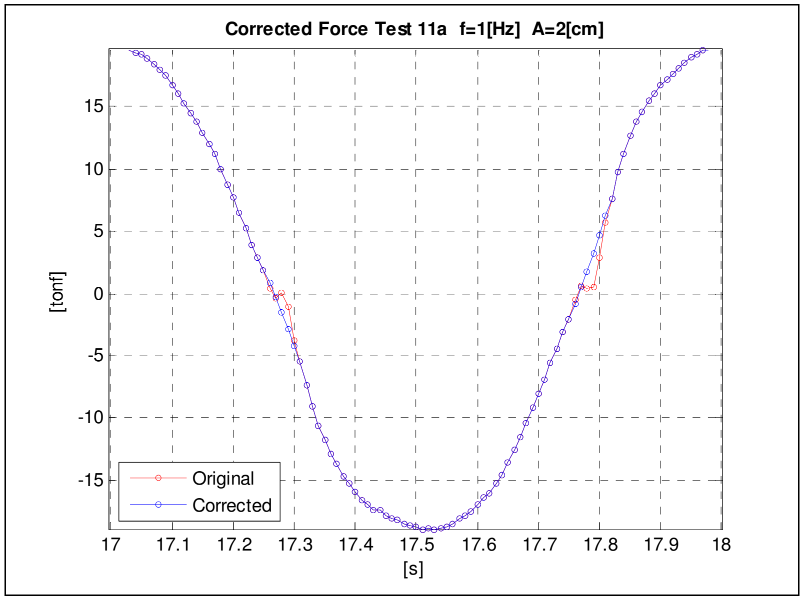

Figure E-7: Points in red were replaced with interpolated points using the previous and subsequent zones.

Force-velocity relationships for all the performed tests and the non-Linear Maxwell macromodel fitted to them are presented in the following figures, grouped in chronological order of execution. The green points are data that was disregarded and corrected with the procedure just described.

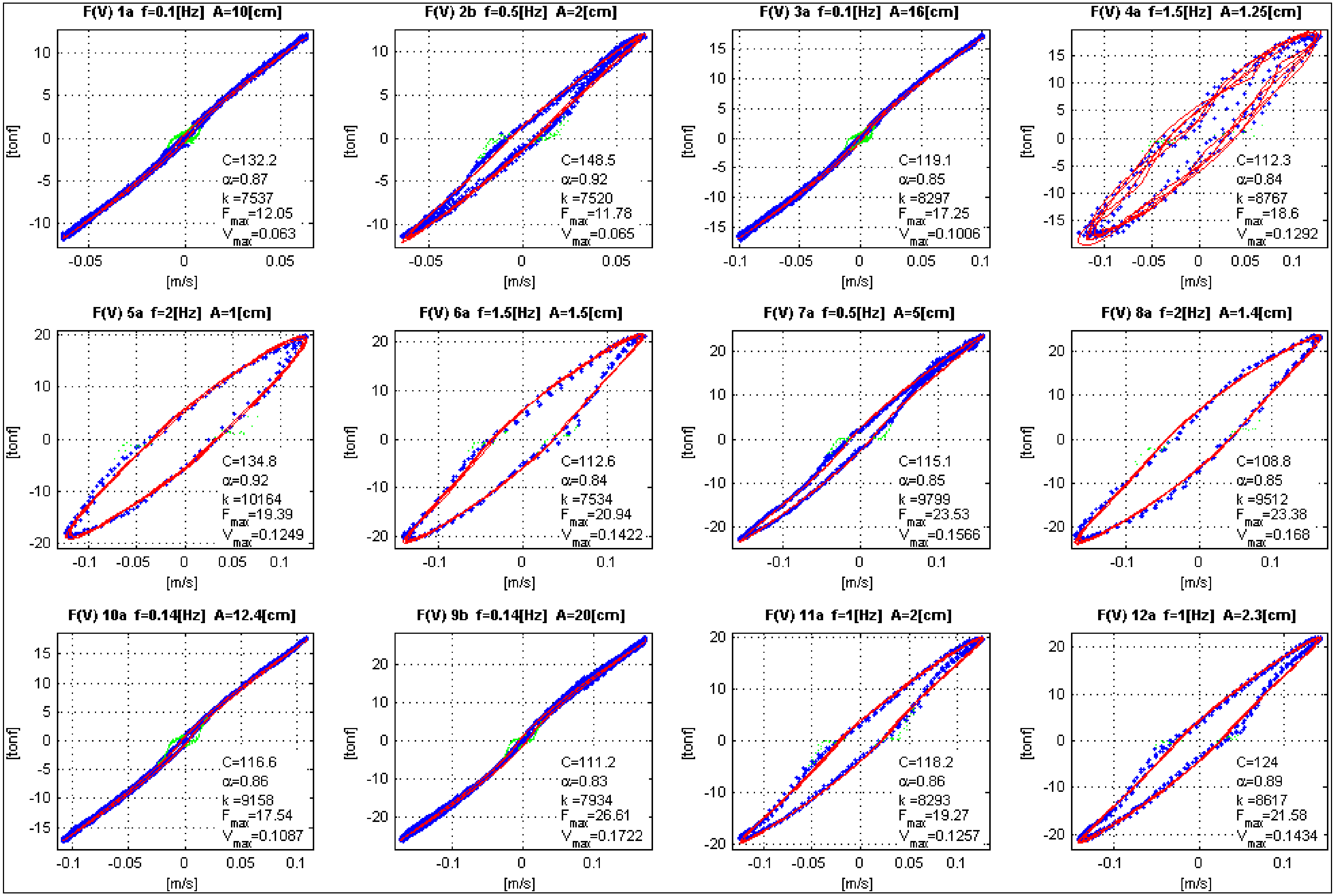

Figure E-8: Experimental force-velocity relationships measured during Session 1 (blue) and fit of Eq. (7.1) to this data (red).

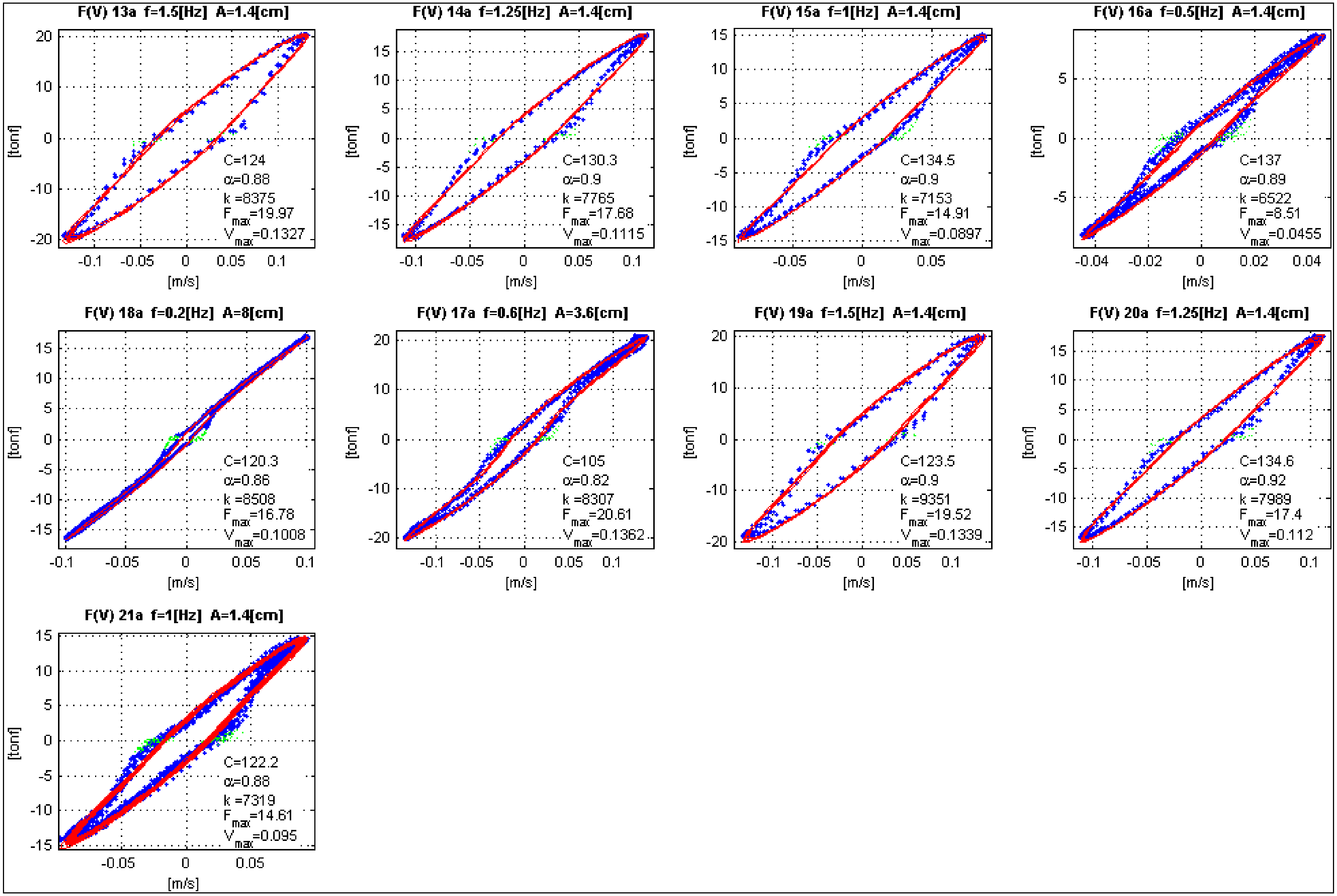

Figure E-9: Experimental force-velocity relationships measured during Session 1 (blue) and fit of Eq. (7.1) to this data (red).

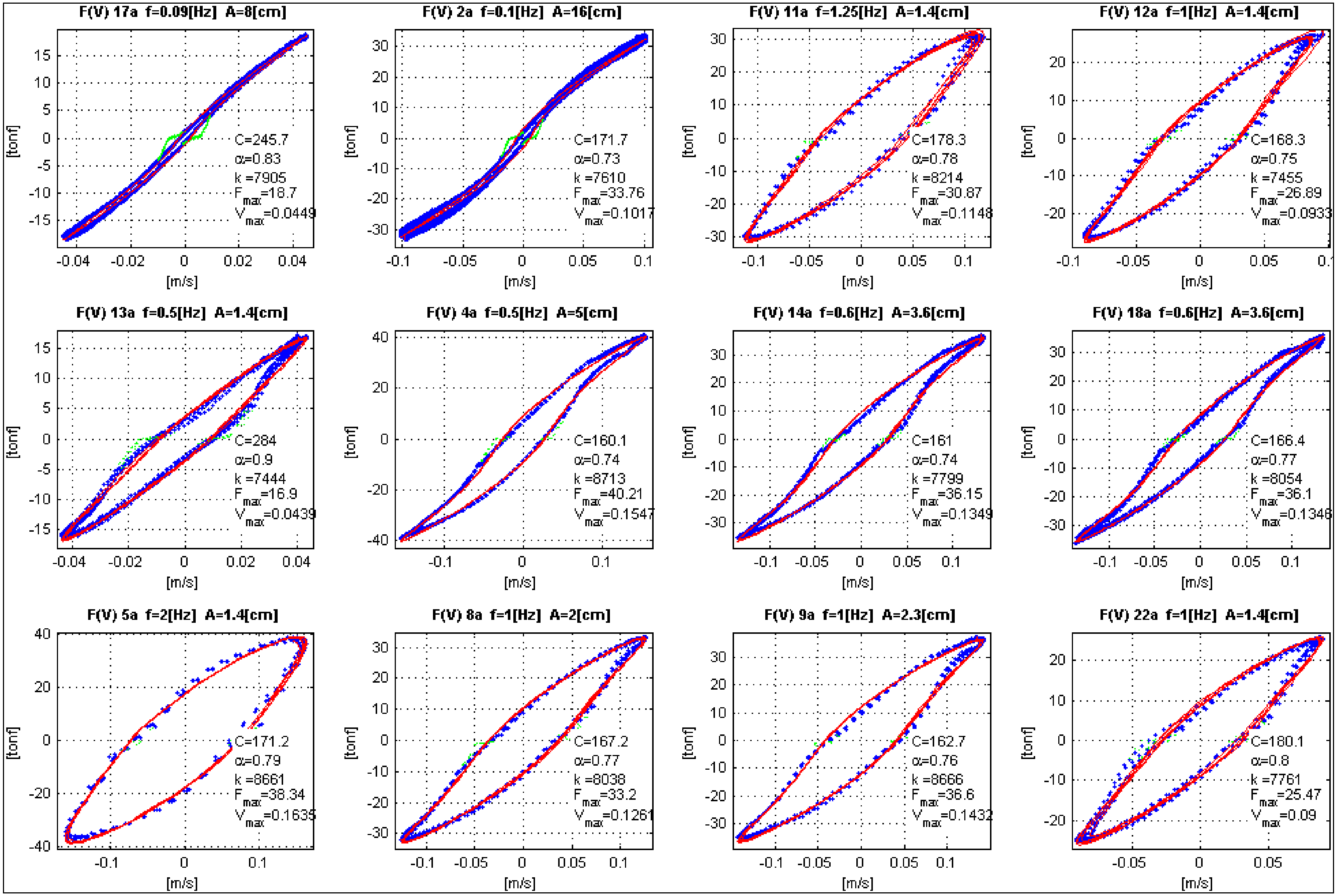

Figure E-10: Experimental force-velocity relationships measured during Session 2 (blue) and fit of Eq. (7.1) to this data (red).

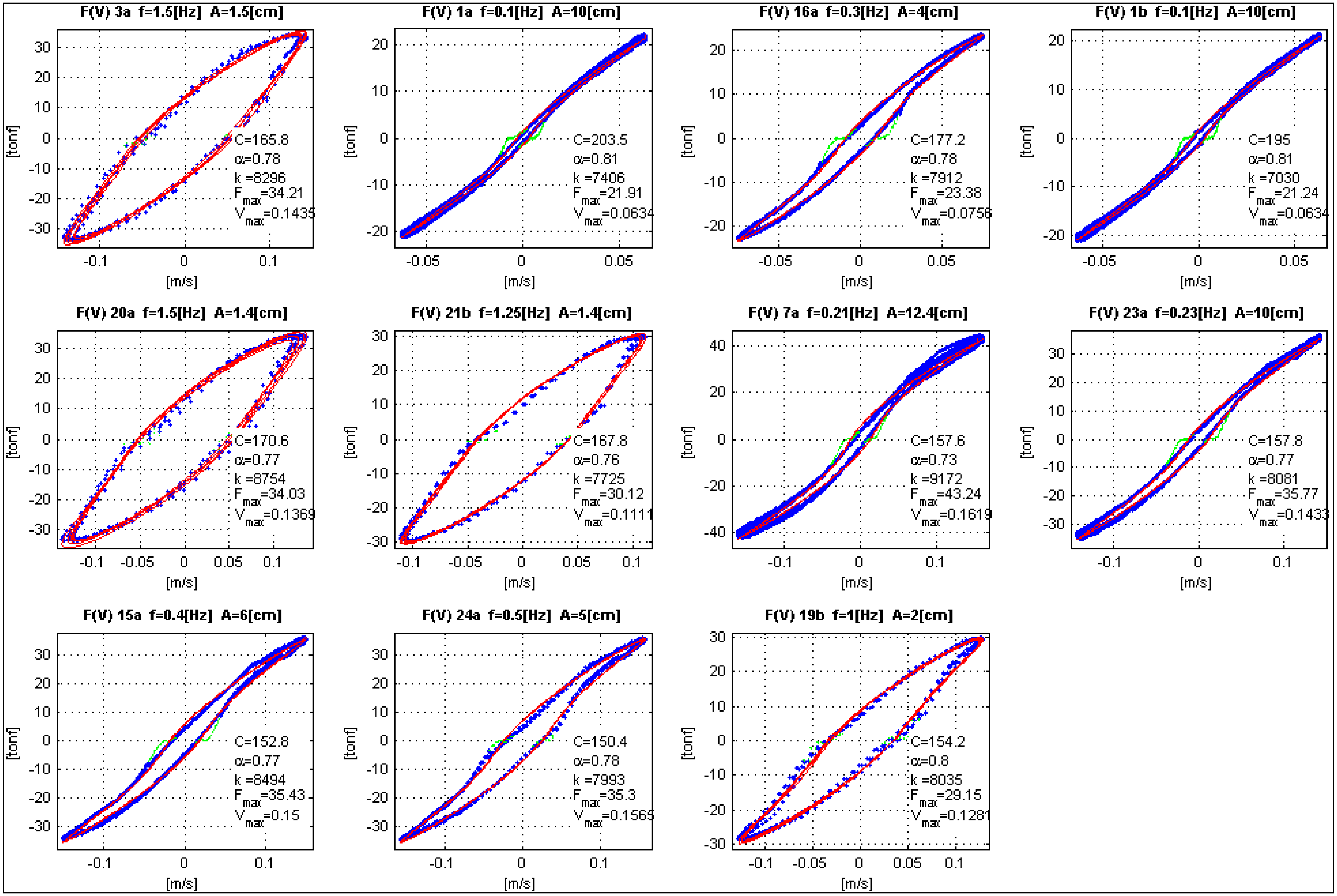

Figure E-11: Experimental force-velocity relationships measured during Session 2 (blue) and fit of Eq. (7.1) to this data (red).

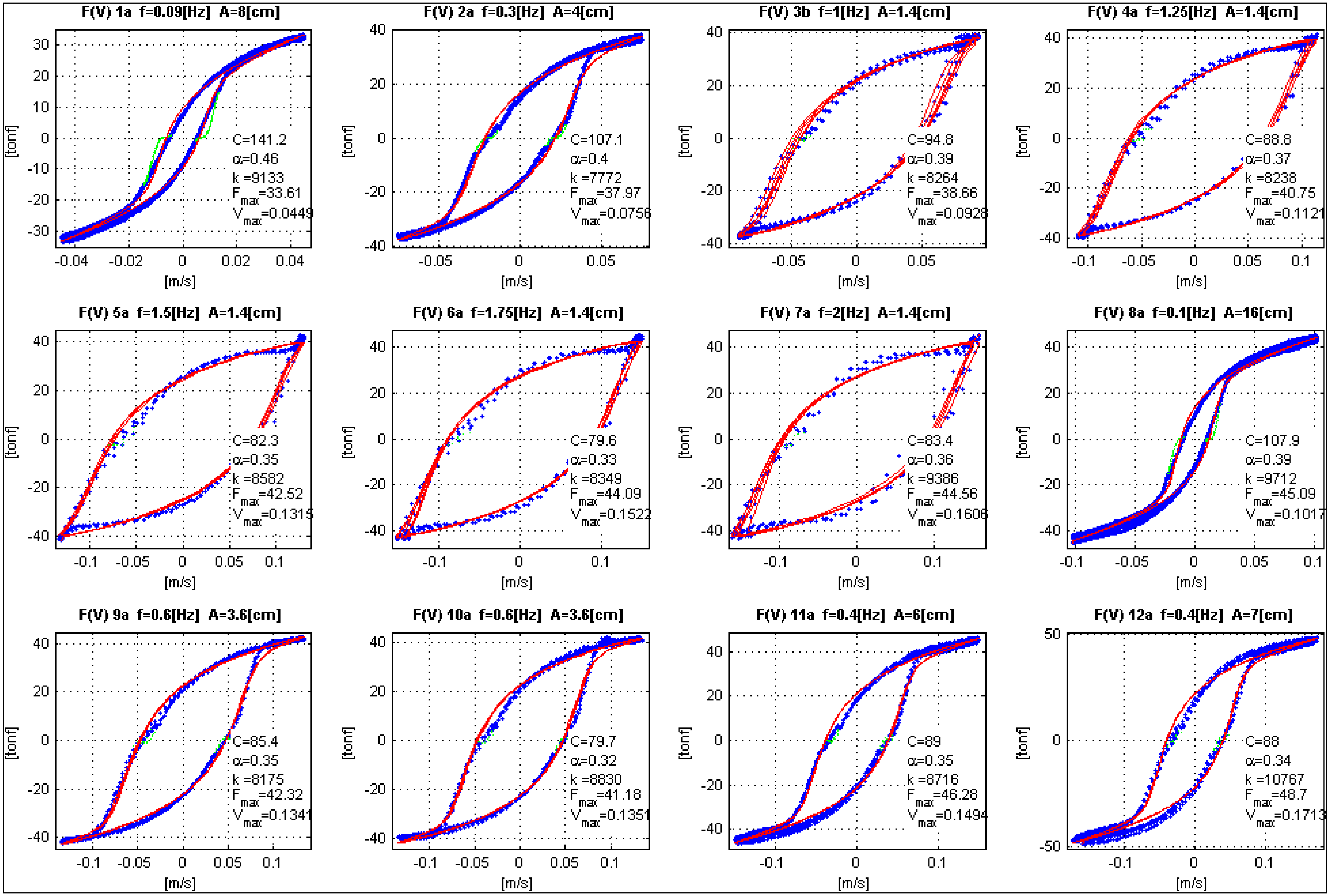

Figure E-12: Experimental force-velocity relationships measured during Session 3 (blue) and fit of Eq. (7.1) to this data (red).

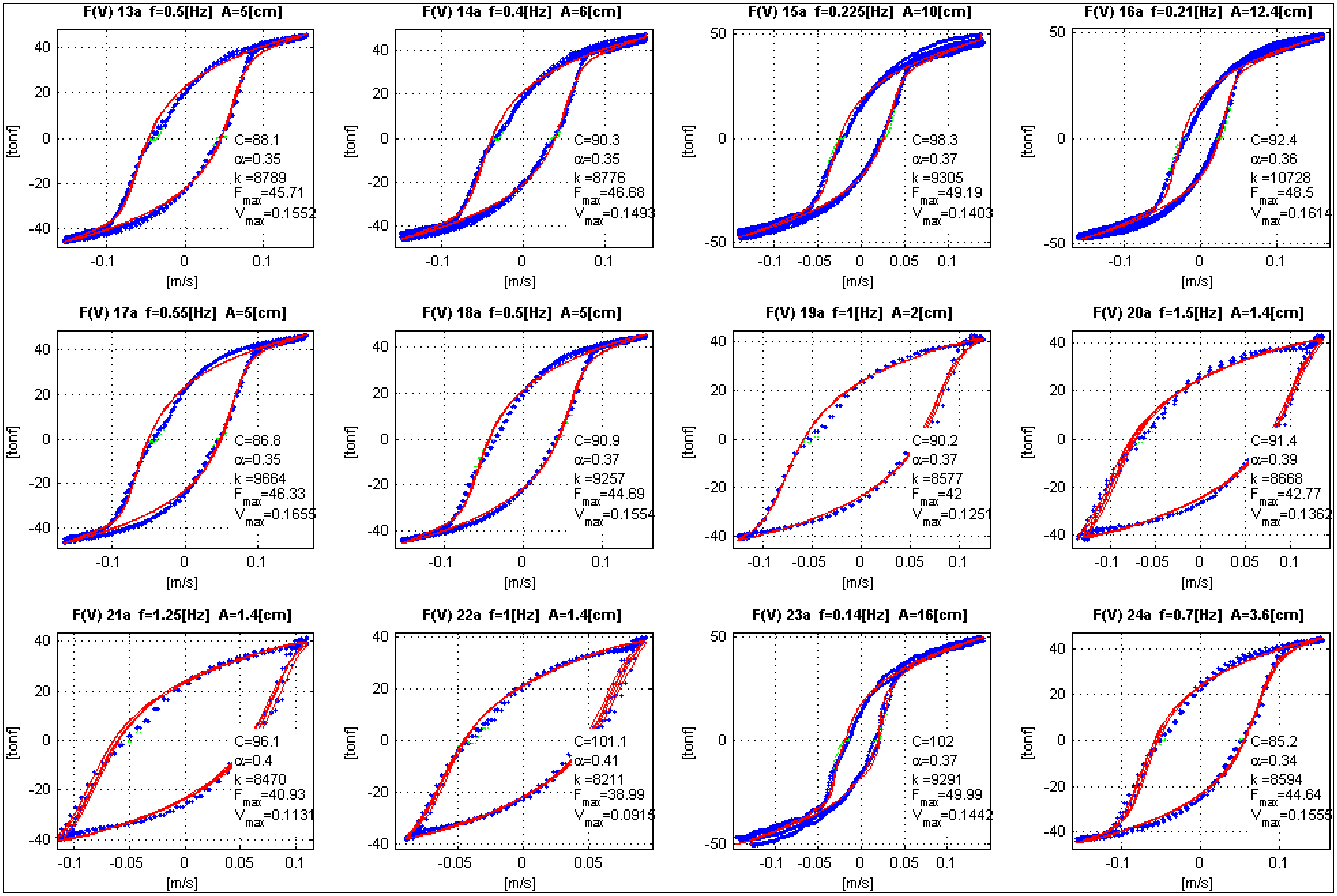

Figure E-13: Experimental force-velocity relationships measured during Session 3 (blue) and fit of Eq. (7.1) to this data (red).

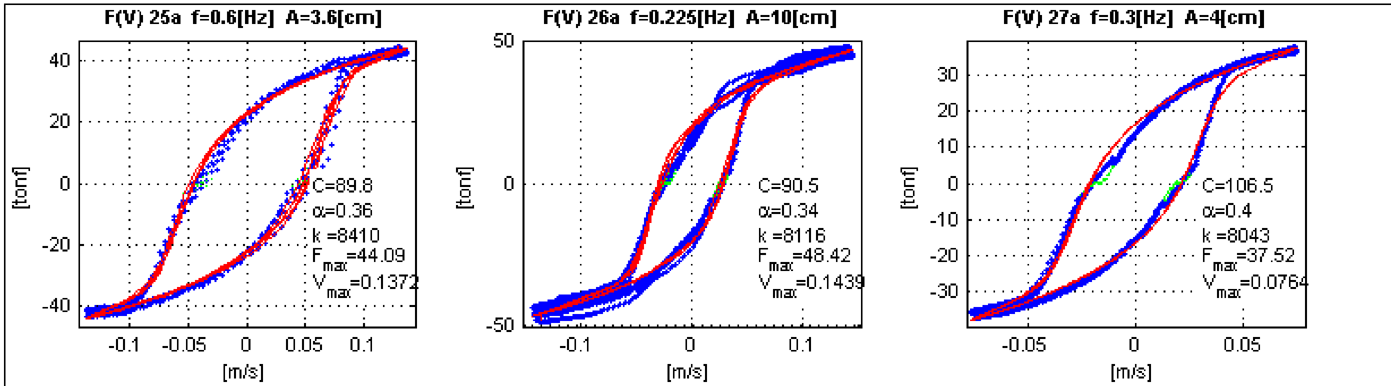

Figure E-14: Experimental force-velocity relationships measured during Session 3 (blue) and fit of Eq. (7.1) to this data (red).

Table E-4: Summary of parameters resulting from the fit of the non linear Maxwell macro model (Eq. (7.1)) to the experimental results from Design 1.

Test ID	**Amplitude (cm)**	**Frecuency (Hz)**	**Max Vel. (cm/s)**	**C tonf/(m/s)$^{\alpha}$**	**α**	**K (tonf/m)**
1a	10	0.1	6.28	132.2	0.87	7537
2b	2	0.5	6.28	148.5	0.92	7520
3a	16	0.1	10.05	119.1	0.85	8297
4a	1.25	1.5	11.78	112.3	0.84	8767
5a	1	2	12.57	134.8	0.92	10164
6a	1.5	1.5	14.14	112.6	0.84	7534
7a	5	0.5	15.71	115.1	0.85	9799
8a	1.4	2	17.59	108.8	0.85	9512
10a	12.4	0.14	10.91	116.6	0.86	9158
9b	20	0.14	17.59	111.2	0.83	7934
11a	2	1	12.57	118.2	0.86	7293
12a	2.3	1	14.45	124	0.89	8617
13a	1.4	1.5	13.19	124	0.88	8375
14a	1.4	1.25	11	130.3	0.9	7765
15a	1.4	1	8.8	134.5	0.9	7153
16a	1.4	0.5	4.4	137	0.89	6522
18a	8	0.2	10.05	120.3	0.86	8508
17a	3.6	0.6	13.57	105	0.82	8307
19a	1.4	1.5	13.19	123.5	0.9	9351
20a	1.4	1.25	11	134.6	0.92	7989
21a	1.4	1	8.8	122.2	0.88	7319
			Ave.	**123.1**	**0.87**	**8258**
			Min.	105.0	0.82	6522
			Max.	148.5	0.92	10164
			Std. Dev.	11.02	0.03	952

Table E-5: Summary of parameters resulting from the fit of the non linear Maxwell macro model (Eq. (7.1)) to the experimental results from Design 2.

Test ID	**Amplitude (cm)**	**Frecuency (Hz)**	**Max Vel. (cm/s)**	**C tonf/(m/s)$^{\alpha}$**	**α**	**K (tonf/m)**
17a	8	0.09	4.52	245.7	0.83	7905
2a	16	0.1	10.05	171.7	0.73	7610
11a	1.4	1.25	11	178.3	0.78	8214
12a	1.4	1	8.8	168.3	0.75	7455
13a	1.4	0.5	4.4	284	0.9	7444
4a	5	0.5	15.71	160.1	0.74	8713
14a	3.6	0.6	13.57	161	0.74	7799
18a	3.6	0.6	13.57	166.4	0.77	8054
5a	1.4	2	17.59	171.2	0.79	8661
8a	2	1	12.57	167.2	0.77	8038
9a	2.3	1	14.45	162.7	0.76	8666
22a	1.4	1	8.8	180.1	0.8	7761
3a	1.5	1.5	14.14	165.8	0.78	8296
1a	10	0.1	6.28	203.5	0.81	7406
16a	4	0.3	7.54	177.2	0.78	7912
1b	10	0.1	6.28	195	0.81	7030
20a	1.4	1.5	13.19	170.6	0.77	8754
21b	1.4	1.25	11	167.8	0.76	7725
7a	12.4	0.21	16.36	157.6	0.72	9172
23a	10	0.23	14.14	157.8	0.77	8081
15a	6	0.4	15.08	152.8	0.77	8494
24a	5	0.5	15.71	150.4	0.78	7993
19b	2	1	12.57	154.2	0.8	8035
			Ave.	**176.9**	**0.78**	**7905**
			Min.	150.4	0.72	7030
			Max.	284	0.9	9172
			Std. Dev.	30.97	0.04	518

Table E-6: Summary of parameters resulting from the fit of the non linear Maxwell macro model (Eq. (7.1)) to the experimental results from Design 3.

Test ID	Amplitude (cm)	Frecuency (Hz)	Max Vel. (cm/s)	C tonf/(m/s)$^{\alpha}$	α	K (tonf/m)
1a	8	0.09	4.52	142	0.47	8825
2a	4	0.3	7.54	110	0.41	8192
3b	1.4	1	8.8	99.2	0.41	8538
4a	1.4	1.25	11	94.9	0.4	8429
5a	1.4	1.5	13.19	87.1	0.38	8814
6a	1.4	1.75	15.39	85.9	0.37	8605
7a	1.4	2	17.59	88.2	0.39	9751
8a	16	0.1	10.05	107.9	0.39	9660
9a	3.6	0.6	13.57	88.4	0.36	8572
10a	3.6	0.6	13.57	82.2	0.34	9221
11a	6	0.4	15.08	91.1	0.36	9246
12a	7	0.4	17.59	89.7	0.35	11511
13a	5	0.5	15.71	90.4	0.36	9249
14a	6	0.4	15.08	91.8	0.36	9219
15a	10	0.225	14.14	98.3	0.37	9224
16a	12.4	0.21	16.36	92.4	0.36	10566
17a	5	0.55	17.28	88.3	0.35	10033
18a	5	0.5	15.71	90.8	0.37	9257
19a	2	1	12.57	93	0.39	8805
20a	1.4	1.5	13.19	94.1	0.41	8817
21a	1.4	1.25	11	101.4	0.42	8610
22a	1.4	1	8.8	110.8	0.44	8583
23a	16	0.14	14.07	102	0.37	9248
24a	3.6	0.7	15.83	86.5	0.35	8783
25a	3.6	0.6	13.57	92	0.37	8760
26a	10	0.23	14.14	92.1	0.35	8690
27a	4	0.3	7.54	113.1	0.43	8882
			Ave.	**96.4**	**0.38**	**8736**
			Min.	82.2	0.34	8192
			Max.	142	0.47	11511
			Std. Dev.	12.21	0.03	709

APPENDIX F: CALIBRATION OF THE YASUDA-CARREAU PARAMETERS

As explained in the body of the thesis, discrepancies between the numerical and experimental results were not unexpected due to the uncertain rheological behavior of the employed fluids. In order to achieve a better agreement between models and experiments, parameters κ, a and n of the Yasuda-Carreau equation, i.e., Eq. (2.9), were calibrated as explained here.

To accomplish this task, tests concerning annular orifice configurations were used since analytical approximations are easier to derive in their case. Specifically, Eq. (4.1) represents a simple, yet accurate expression to estimate output force for annular orifice dampers. For convenience, this equation is presented again here:

$$\begin{aligned} F_a &= \frac{\left(R_p^{\,2} - R_v^{\,2}\right)^2 6\pi\mu_{ave} L_p}{R_p h^3} V \\ \mu_{ave} &= \mu_0 \left[1 + \left(\kappa \left|\dot{\gamma}_{ave}\right|\right)^a\right]^{\frac{n-1}{a}} \\ \dot{\gamma}_{ave} &= \frac{2\left[\left(R_p + h\right)^2 - R_v^{\,2}\right]}{R_p h^2} V \end{aligned} \tag{F.1}$$

Test results from Design 2 were thus used to adjust the parameter values of SF1 and test results from Design 3 for SF30; both designs correspond to annular orifice geometries.

If instead of a single value, V is substituted with a range of velocities in Eq. (F.1), for example the different velocities measured during a test, a force-velocity curve will be obtained. Since this equation does not include compressibility, the resulting curve will be purely viscous, with no memory or viscoelastic effects. The experimental data, on the other hand, is not purely viscous, even though tests with a relatively low frequency and high amplitude were chosen in each fluid's case to minimize this effect. Therefore, instead of fitting Eq. (F.1) directly to the experimental data, it was fitted to a force velocity curve generated with an equation in the form of $F = C|V|^{\alpha}\,\mathrm{sgn}(V)$, that is Eq. (1.1), the classic purely viscous model. The values for C and α were obtained from fitting Eq. (7.1), the proposed non-linear Maxwell macroscopic model, to specific tests from each design. This indirect method was found to be more appropriate and yielded better results than directly using the experimental curve, since it allowed to fit Eq. (F.1) to an also purely viscous model.

Denoting the data generated with Eq. (1.1) as (V_k, F_k), the calibration's objective was to vary parameters κ, a and n in Eq. (F.1) until $F_a(V_k)$ was as similar as possible to F_k in a least-squares sense. Mathematically this is:

$$\min_{\kappa,a,n} \sum_{k=1}^{N}\left[F_k - F_a(\kappa,a,n,V_k)\right]^2$$

$$\begin{aligned} &\kappa_{\min} \le \kappa \le \kappa_{\max} \\ &a_{\min} \le a \le a_{\max} \\ &n_{\min} \le n \le n_{\max} \end{aligned} \tag{F.2}$$

The individual procedure for each fluid is detailed next. Please recall from Eq. (2.11) that while a and n are independent of temperature, κ has to be multiplied by a shift factor $Z(T)$ to account for different temperatures. For convenience, the κ values obtained in the fitting process were shifted to the fluid's reference temperatures, 25°C for SF1 and 20°C for SF30.

Parameter Calibration for SF30

Test 16a (according to Table E-3 and referred to as Test 3-1 during the body of the thesis) was chosen to calibrate the parameters for the SF30 fluid. It was selected for various reasons. Naturally, to properly characterize the viscosity-shear rate relationship, shear rate values as high as possible are needed and Test 16a was one of the tests that reached the highest input velocity permitted by the dynamic actuator's pump. Additionally, it was the first test performed on the day it took place. As a consequence, it is reasonable to suppose that the fluid temperature measured at one of the cylinder caps was uniform throughout the fluid, which ceases to be true once a test has been performed. This implicates that the zero-shear rate viscosity μ_0, a function of temperature, can be estimated confidently. Hence, for the initial fluid temperature measured at 20 °*C*, $\mu_0 \approx 30$ *Pa·s*. This value happened to coincide with the fluid's reference temperature, allowing the direct calculation of κ without the need of a temperature shift. Moreover, only the first complete cycle of this test was used in order to avoid further temperature effects that alter the force-velocity curve as the fluid heats.

Fitting Eq. (7.1) to the experimental force-velocity curve from the first full-amplitude cycle of Test 16a yielded the following results: $\alpha = 0.34$, $C = 96.3$ $tonf/(m/s)^{\alpha}$ and $K = 9929$ *tonf/m*. (Note: these results differ slightly from the results presented in Table E-6 since those considered five complete cycles instead of one like it was done here.) Figure F-1 shows the experimental data and the macroscopic model fitted to it.

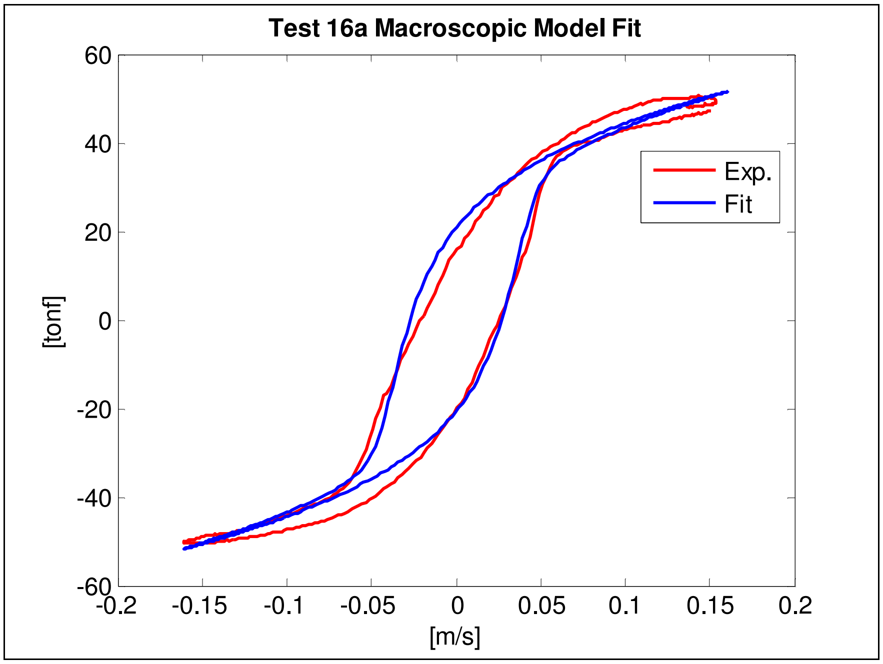

Figure F-1: Comparison of the first complete cycle of Test 16a (in red) and the fit of Eq. (7.1) (in blue) to this data.

As explained earlier, resulting values α = 0.34, C = 96.3 $tonf/(m/s)^{\alpha}$ were used to generate a new force-velocity curve, using Eq. (1.1), whose objective is to resemble the experimental data. A comparison between both can be seen in Figure F-2.

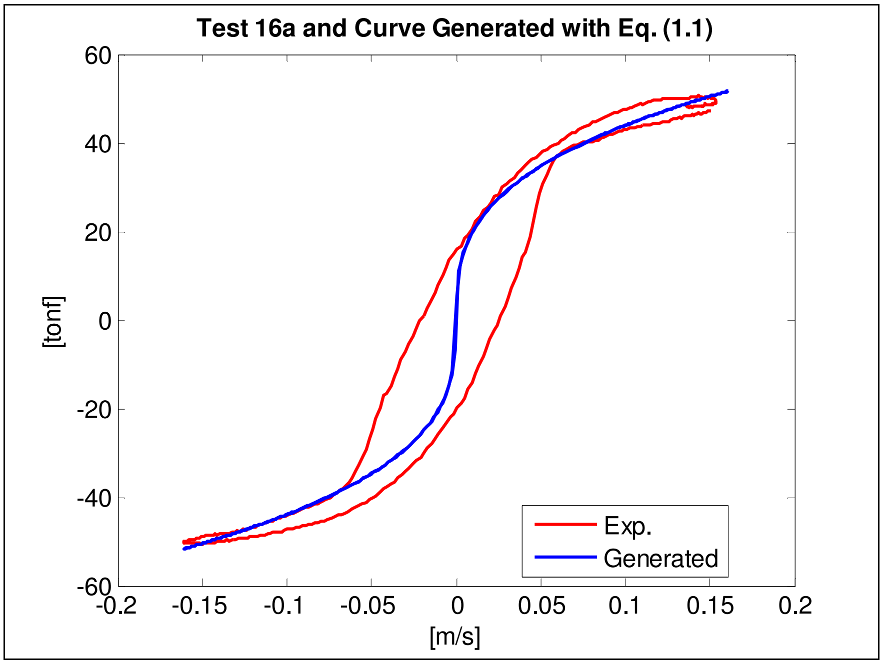

Figure F-2: Comparison of the first complete cycle of Test 16a (in red) and the curve generated with Eq. (1.1) using the fitted values of α and C.

Subsequently, Eq. (F.1) was fitted to the generated curve (blue in Figure F-2): the resulting optimal Yasuda-Carreau parameters were a = 2.0, n = 0.33 and κ = 1.46e-3 s. Please recall that this κ value corresponds to a temperature of 20°C. The bounds considered for the optimization problem, as expressed in (F.2), are shown in Table F-1.

Table F-1: Upper and lower limits for the Yasuda-Carreau parameters during the SF30 optimization process.

	a	n	κ
Min	0.1	0.2	1.00e-3 [s]
Max	2.0	0.4	2.50e-3 [s]

It can be noted that the optimal solution attaches to the upper boundary in the case of a. The same continued happening if a's upper bound was increased and, in consequence, it was set at a = 2.0, a value common to many shear-thinning fluids. In fact a = 2 is a particular case of the Yasuda-Carreau model known simply as the Carreau model. Hou et. al. (2007) used this equation to characterize a silicone fluid in a damper. Anyhow, this is not especially relevant since the sensitivity of the result with respect to parameter *a* is very low. As an example, Figure F-3 shows the result of plotting Eq. (F.2) with the optimal parameter values and then with a value of *a* twice as high; the resulting curve barely changes.

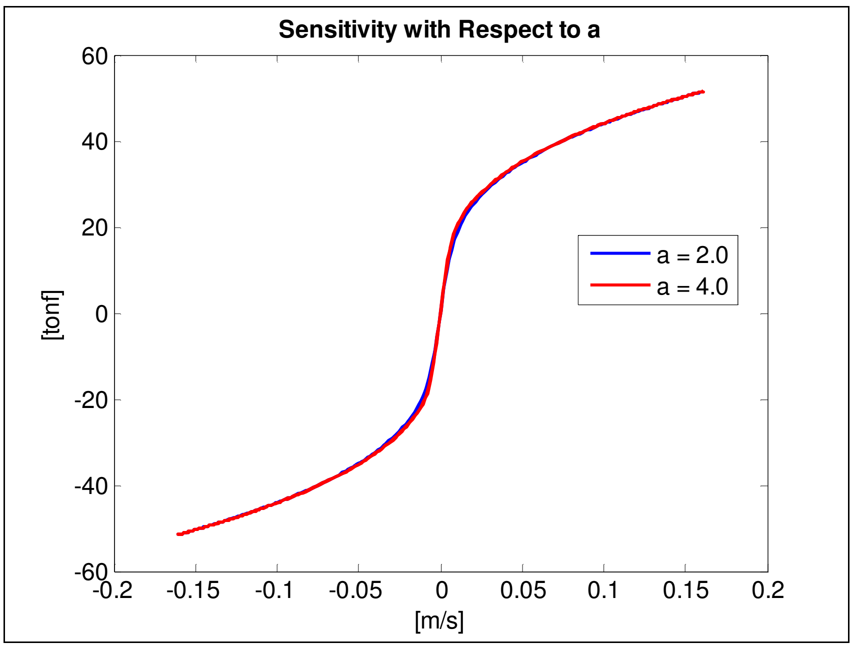

Figure F-3: Force-velocity relationships calculated with Eq. (F.1) and the optimal parameter values. Even though *a* was doubled in the red curve case, the difference in the resulting curve is negligible.

Finally, Figure F-4 compares the plot of Eq. (F.1) using the optimal parameters with the force-velocity curve generated with Eq. (1.1) and with the experimental data corresponding to Test 16a.

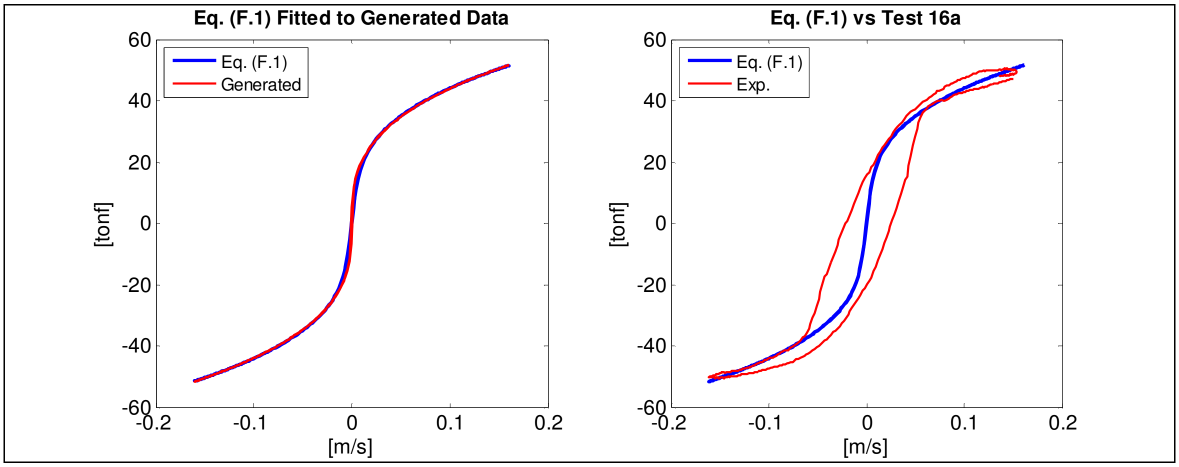

Figure F-4: The left plot shows the fit of Eq. (F.1) to the curve generated with Eq. (1.1) and the right plot compares this result with the experimental data.

Parameter Calibration for SF1

The original intention for the SF1 parameter calibration was to use a test performed under the same scenario as Test 16a for SF30 in the sense that it would be the first one of the day, allowing the assumption of a uniform fluid temperature. Unfortunately, this condition could not be replicated since there was a pump malfunction during the first test; its measured data was useless and the opportunity to perform a test with a good knowledge of the internal fluid temperature was therefore lost. Please recall that the temperature rise of the fluid concentrates in the piston displacement zone, as seen in Figure 5-7. Therefore, once a test has been performed, the measurement of the temperature sensor, placed at one of the cylinder caps, is no longer representative of the fluid temperature.

To amend this situation, the selected approach was to approximate the fluid's temperature according to its pressure and assume a uniform temperature distribution throughout the cylinder. With temperature measured in °*C* and pressure in *bar*, the next equation, derived from Eq. (5.1), relates temperature and pressure increases:

$$\Delta T = 0.078 \cdot \Delta p \tag{F.3}$$

Test 7a (according to Table E-2 and referred to as Test 2-1 during the body of the thesis) was selected for the calibration of the SF1 fluid. Before any test took place that day, the damper's initial fluid pressure was measured at 117.4 *bar* and the temperature at 18.5°C, values that were used as reference points to estimate μ_0. On the other hand, at the beginning of Test 7a fluid pressure was measured at 219.9 *bar*. Using Eq. (F.3), the corresponding fluid temperature was approximated as:

$$T_{7a} - 18.5 = 0.078 \cdot (219.9 - 117.4) \Rightarrow T_{7a} = 26.50°C \tag{F.4}$$

For SF1 this corresponds to a zero shear rate viscosity of $\mu_0 = 0.95$ *Pa·s*.

Fitting Eq. (7.1) to the experimental force-velocity curve from the first full-amplitude cycle of Test 7a yielded the following results: $\alpha = 0.714$, $C = 161.9$ *tonf*/(*m*/*s*)$^{\alpha}$ and $K = 9195$ *tonf*/*m*. Figure F-5 shows the experimental data and the macroscopic model fitted to it.

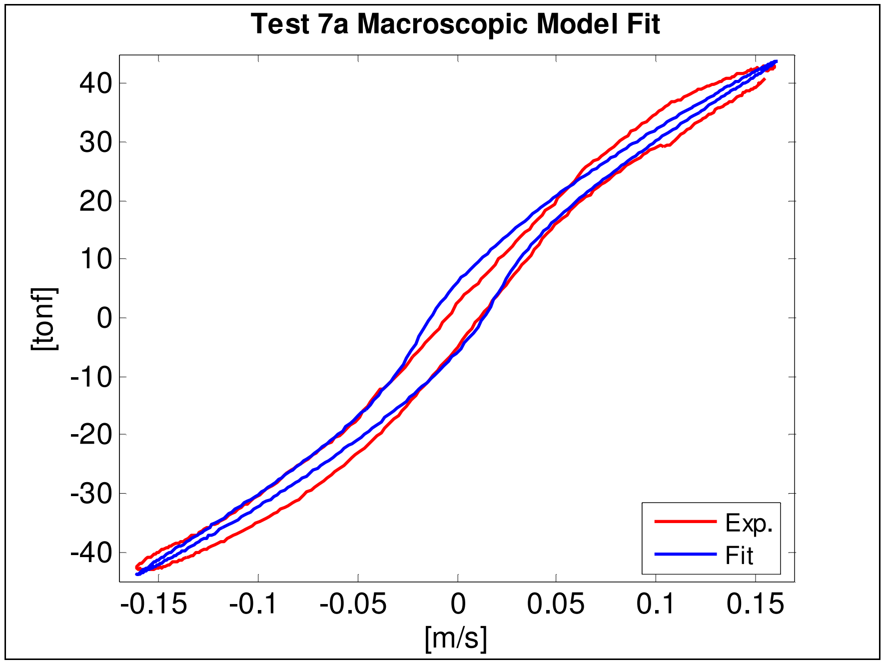

Figure F-5: Comparison of the first complete cycle of Test 7a and the fit of Eq. (7.1) (in blue) to this data.

As before, the resulting values α = 0.714 and C = 161.9 $tonf/(m/s)^{\alpha}$ were used to generate a new force-velocity curve using Eq. (1.1). A comparison between this and the experimental curve can be seen in Figure F-6.

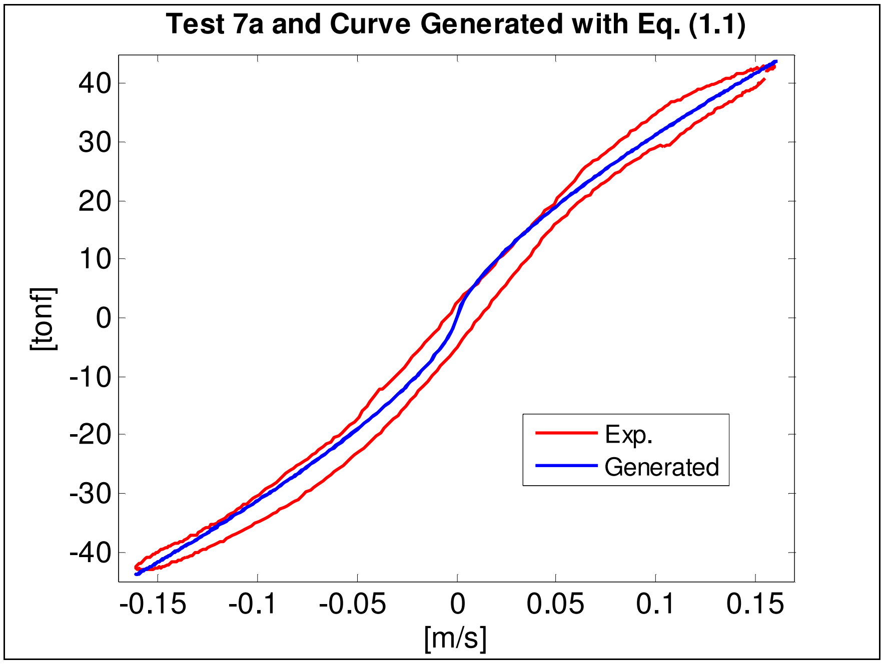

Figure F-6: Comparison of the first complete cycle of Test 7a (in red) and the curve generated with Eq. (1.1) using the fitted values of α and C.

Subsequently, Eq. (F.1) was fitted to the generated curve (blue in Figure F-6): the resulting optimal Yasuda-Carreau parameter values were a = 2.0, n = 0.44 and κ = 4.13e-5 s. Shifting κ's value to 25°C (SF1's reference temperature) with b = 1452 K yields:

$$\kappa_{25} = \exp\left(\frac{b}{299.65} - \frac{b}{298.15}\right) \cdot \kappa_{26.5} = 4.03 \cdot 10^{-5} \left[s\right] \qquad \text{(F.5)}$$

The bounds for the optimization problem are shown in Table F-2. The optimal solution for this fluid also attached to the upper boundary in the case of a, thus it was decided to limit that value to 2.0 again.

Table F-2: Upper and lower limits for the Yasuda-Carreau parameters during the SF1 optimization process.

	a	n	κ
Min	0.1	0.3	1.0e-5 [s]
Max	2.0	0.8	9.0e-5 [s]

Finally, Figure F-7 compares the plot of Eq. (F.1) using the optimal parameters with the force-velocity curve generated with Eq. (1.1) and with the experimental data corresponding to Test 7a.

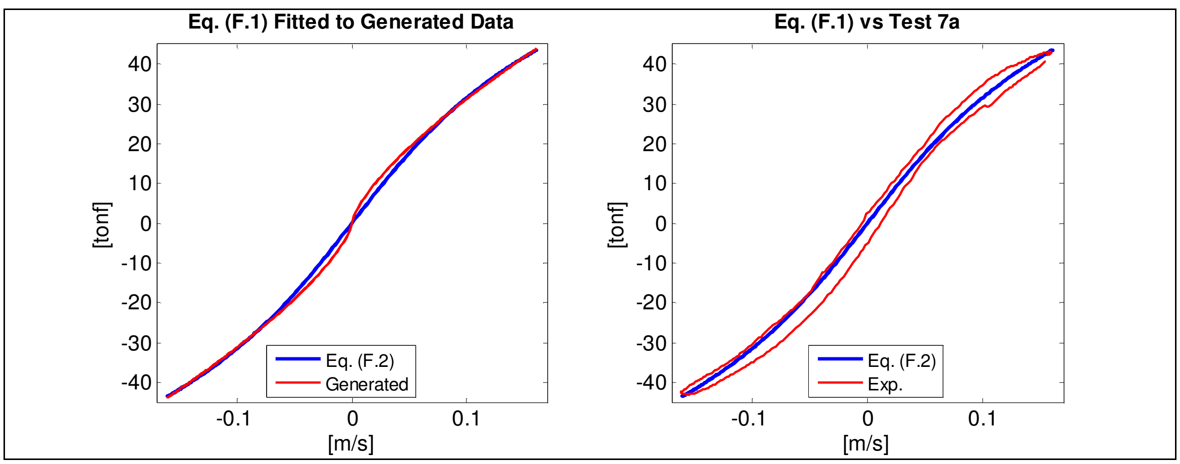

Figure F-7: The left plot shows the fit of Eq. (F.1) to the curve generated with Eq. (1.1) and the right plot compares this result with the experimental data.